To the Graduate Council:

I am submitting herewith a dissertation written by Rubayet Tanveer entitled "Synthesis and Investigation of Multifunctional High Entropy Oxides." I have examined the final electronic copy of this dissertation for form and content and recommend that it be accepted in partial fulfillment of the requirements for the degree of Doctor of Philosophy, with a major in Materials Science and Engineering.

Veerle Keppens, Major Professor

We have read this dissertation and recommend its acceptance:

_____

Veerle Keppens

_____

William J. Weber

_____

David Mandrus

_____

Katharine Page

_____

Maik K. Lang

Accepted for the Council:
Dr. Marieke Van Puymbroeck
Vice Provost and Dean of the Graduate School

(Original signatures are on file with official student records.)

Synthesis and Investigation of Multifunctional High Entropy Oxides

A Dissertation Presented for the
Doctor of Philosophy
Degree
The University of Tennessee, Knoxville

Rubayet Tanveer
December 2025

© by Rubayet Tanveer, 2025
All Rights Reserved.

Acknowledgements

Firstly, I want to thank my supervisor Dr. Veerle Keppens for providing me the work opportunity in a top-notch research environment, training me on research methodology, and constant guidance. Secondly, I want to thank my co-advisor Dr. William J Weber for his consistent support and guidance and for providing great opportunities for research and learning. It was also a great opportunity for me to be under the mentorship of Dr. David Mandrus throughout my research work, and I must specially acknowledge his MSE 514 class – one of the best courses I have attended during all my graduate studies. My special thanks will go to Dr. Maik Lang, Dr. Haidong Zhou, Dr. Bin Hu and Dr. Katharine Page and their group for helping me with my research and providing a great opportunity to collaborate.

I thank my friend Dylan Windsor and Dr. Haixuan Xu for their invaluable computational support throughout this research. My friendship with Dylan traces back to the *Defects* class taught by Dr. Weber, where our shared interests first converged.

I'm extremely grateful to all my fellow colleagues from the Mandus-Keppens group: Candice Kinsler-Fedon, William Meier, Shirin Mozaffari, Seung Hwan Do, Matthew Cothrine and others.

My heartfelt thanks to all the staff of the Institute of Advanced Materials and Manufacturing (IAMM) and the department of MSE.

This work was supported by the National Science Foundation under Grant No. DMR-2104228.

Abstract

The deliberate introduction of configurational entropy has emerged as a powerful strategy for stabilizing complex oxides and enabling novel functionalities. In this dissertation, the synthesis and investigation of multifunctional high-entropy oxides (HEOs) are undertaken with a focus on perovskite and garnet structures. A family of rare-earth perovskites, $REBO_3$ (RE = La, Pr, Nd, Sm, Eu, Gd; B = Sc, Al, Cr, Ni, Fe), was synthesized with equimolar B-site occupancy. All compositions crystallize in the orthorhombic *Pnma* structure and exhibit thermally activated transport. Magnetic ordering was observed at low temperatures in $LaBO_3$, $PrBO_3$, and $SmBO_3$, with the transition temperatures shifting in relation to the rare-earth ionic moment.

Detailed investigation of the high-entropy perovskite $Eu(Sc/Cr/Fe/Ni/Al)O_3$ revealed a subtle interplay between local bonding, charge ordering, and polaron transport. SQS-based PDF analysis identified anomalously short Eu–Ni and long Ni–O distances, indicating electrostatic coupling between Eu and Ni, while bond-valence results confirmed the coexistence of Ni^{2+}, Cr^{3+} and Cr^{4+} at the ground state. Temperature-dependent XRD analysis showed a structural anomaly near 140 K, correlating with a crossover in conduction from Ni-mediated small-polaron hopping to Cr- or oxygen-mediated hopping. Magnetization measurements confirmed an antiferromagnetic transition at ~17 K and additional features near ~130 K. Complementary photoluminescence spectroscopy revealed intensity quenching below 150 K possibly due to reduced electron–phonon coupling.

Extending the high-entropy design to the garnet system, $Y_3Fe_4(Sc/Cr/Ga/Al)_1O_{12}$ and $Y_3Fe_3(Sc/Cr/Ga/Al)_2O_{12}$ were synthesized via Fe^{3+} - sublattice substitution in YIG. Both retain the cubic *Ia$\bar{3}$d* structure, yet PDF and DOS analysis exposed distinct site preferences for Sc^{3+}/Cr^{3+} toward octahedral coordination and, in $Y_3Fe_3(Sc/Cr/Ga/Al)_2O_{12}$, nanoscale Al^{3+} short-range ordering invisible to average probes. This emergent short-range order disrupts long-range spin connectivity, producing cluster-glass-like magnetism, while Cr^{3+} substitution enhances photoluminescence although the short-range order delocalizes the local crystal-field environment. Together, these studies demonstrate that entropy-driven compositional complexity not only stabilizes unconventional oxide phases but also engenders tunable couplings among structural, electronic, magnetic, and optical degrees of freedom – offering new design principles for multifunctional materials.

Table of Contents

List of Figures

CHAPTER 1
INTRODUCTION

The design of materials with coexisting and synergistic functional properties – such as magnetism, electronic transport, and optical transitions – remains a central goal in condensed matter physics and materials science. In many advanced material systems, key functionalities such as electronic transport, magnetism, and photoluminescence are not merely independent – they are often fundamentally antagonistic in nature. Strong electronic correlations that promote charge localization, essential for magnetic ordering and optical transitions in certain oxides, can simultaneously hinder delocalized carrier transport. Likewise, local structural disorder that enables spin-glass and cluster-glass behavior is typically incompatible with the long-range structural coherence required for conventional magnetic phases such as ferromagnetism or antiferromagnetism. These inherent functional and structural dichotomies impose significant constraints on traditional materials design, which often relies on precise compositional control within narrow solid-solution limits. Overcoming these constraints necessitates a fundamentally different design paradigm – one that can mediate, reconcile, or even exploit these competing phenomena within a single, unified crystalline framework.

Recent advances in the field of high-entropy and entropy-stabilized materials have opened new pathways to overcome these limitations. Originally conceptualized in the context of metallic alloys, the idea of utilizing high configurational entropy to stabilize single-phase solid solutions at elevated temperatures has since expanded into complex oxides. High-entropy oxides (HEOs) and entropy-stabilized oxides (ESOs) now form an established class of materials where multiple cationic species can coexist on a single sublattice, leading to novel combinations of structure, disorder, and functionality. By introducing a high degree of compositional disorder, one can access energy landscapes and local environments not achievable in ordered compounds – offering a unique handle for tuning dichotomous properties in a concerted fashion.

This framework is particularly promising for perovskites (ABO_3) and garnets ($A_3B_5O_{12}$), two oxide families renowned for their structural versatility and functional richness. Perovskites accommodate a wide range of A- and B-site cations, and their functional diversity spans magnetism, conductivity, and optoelectronic behavior. Garnets, on the other hand, are traditionally known for their optical transparency, magnetic ordering, and stability across extreme environments. However, in such systems, the co-optimization of magnetic, optical and electronic properties – such as achieving high conductivity without sacrificing luminescence, bypassing spin selection rule or introducing spin glass inside a strongly connected ordered magnetic chain – has remained difficult due to the structural and electronic rigidity imposed by conventional synthesis routes.

High configurational entropy provides a thermodynamic lever to expand the phase space of both perovskites and garnets. In perovskites, multi-principal B-site or A-site mixing can modulate the electronic bandwidth, carrier localization, and octahedral distortions in ways that simultaneously influence optical transitions and charge transport. In garnets, mixing on the dodecahedral, octahedral, and tetrahedral sites can perturb local structural order, crystal field environments and magnetic interactions, opening pathways to magnetic-optical coupling and tunable bandgaps. Importantly, the local disorder inherent to entropy-driven design does not preclude global crystallinity, allowing for property coexistence rather than mutual exclusion.

The central hypothesis of this work is that configurational entropy can be strategically used to engineer multifunctionality in perovskites and garnets, particularly in systems where electronic and optical properties are inherently at odds. This dissertation explores if or how compositional disorder alters the structural, electronic, magnetic and optical landscape of these complex oxides, and, how such disorder may be leveraged to navigate and reconcile dichotomous material requirements.

In doing so, the work contributes to a growing effort to define a new paradigm in materials design – one in which disorder is not an impediment, but a functional tool. This thesis seeks to formulate foundational design strategies for entropy-driven multifunctionality in complex oxides by integrating conventional synthesis techniques, comprehensive structural characterization, and in-depth physical property measurements.

CHAPTER 2
BACKGROUND

2.1 *3d*-orbital Driven Multifunctionality

Transition metal oxides (TMOs) constitute a versatile class of materials in which the intricate coupling among charge, spin, orbital, and lattice degrees of freedom gives rise to a wide spectrum of emergent functionalities. At the heart of these phenomena lie the partially filled *3d* orbitals of the transition metal cations, which serve as the primary conduits for correlated electronic behavior. These orbitals underpin key material properties such as electronic transport, magnetic ordering, and optical emission, making TMOs a compelling platform for multifunctional materials design. The following section delineates these three core functionalities, with an emphasis on their microscopic origins and interdependencies.

2.1.1 Electronic Conductivity: Case of Nickelate Perovskites

Electronic conduction in TMOs primarily arises from the bandwidth and filling of the *3d* orbitals, modulated by the local crystal field environment, hybridization with ligand orbitals, and electron-electron correlations. In perovskite nickelates, typically formulated as $RNiO_3$ (R = rare earth), Ni^{3+} ions adopt a low-spin $3d^7$ electronic configuration, with a nominally quarter-filled e_g^1 configuration in an octahedral ligand field.

The primary mechanism of conductivity in nickelates involves small-polaron or thermally activated hopping of e_g electrons, mediated by Ni-O-Ni bonds. The degree of overlap between Ni *3d* and O-*2p* orbitals is crucial, with the electronic bandwidth (W) defined by the equation [1]:

$$W \propto \frac{\cos(\theta)}{d^n} \tag{2.1}$$

where θ is the Ni–O–Ni bond angle, d is the Ni–O bond length, and n ~ 3.5-4. For rare-earth nickelates, bandwidth control is achieved by modifying the size of the R-site cation, which affects octahedral tilting. Smaller R cations lead to larger tilting (decreased), reducing W and promoting insulating behavior via charge disproportionation (e.g. $2Ni^{3+} \rightarrow Ni^{2+}+Ni^{4+}$). Electronic phase transitions in nickelates are characterized by a temperature-dependent metal-insulator transition (MIT), often coupled to lattice distortions. For example, $PrNiO_3$ exhibits an MIT around 130 K, driven by both bandwidth narrowing and charge ordering [2].

2.1.2 Magnetic Ordering: Antiferromagnetism and Ferrimagnetism

2.1.2.1 Antiferromagnetic Ordering of Cr^{3+}

Chromium ions in the Cr^{3+} oxidation state ($3d^3$ configuration) are a classic example of cations exhibiting antiferromagnetic (AFM) order due to their half-filled t_{2g} orbitals in an octahedral field. Magnetic exchange interactions are dominated by superexchange, mediated through bridging oxygen atoms. According to the Goodenough–Kanamori–Anderson (GKA) rules, AFM coupling is favored when the metal–oxygen–metal bond angle is close to 180°, and the overlapping orbitals are half-filled [3]:

$$J \propto -\frac{t^2}{U} \tag{2.2}$$

where J is the exchange integral, t is the hopping integral (related to overlap of metal and oxygen orbitals), and U is the on-site Coulomb repulsion. In perovskite systems like $EuCrO_3$, Cr^{3+} ions show strong canted AFM coupling with a Néel temperature around 178 K. The long-range magnetic order arises from well-aligned antiparallel spins due to dominant superexchange interactions between Cr^{3+}-O- Cr^{3+} paths [4].

2.1.2.2 Ferrimagnetism in Yttrium Iron Garnet (YIG)

YIG ($Y_3Fe_5O_{12}$) is a prototypical ferrimagnetic garnet with a complex three-sublattice spin structure. Fe^{3+} ions occupy both octahedral and tetrahedral sites, with antiparallel alignment of moments between the sublattices. The net magnetization arises from the unequal number of Fe^{3+} ions in each site: Octahedral: 2 Fe^{3+} per formula unit Tetrahedral: 3 Fe^{3+} per formula unit. The Fe^{3+} ions ($3d^5$, high spin) in both sites contribute fully unpaired spins (S = 5/2), but due to antiferromagnetic superexchange between Octahedral and Tetrahedral sites, the resulting structure is ferrimagnetic. Magnetization M(T) below the Curie temperature ($T_c \sim 560$ K) follows mean-field-like behavior, and spin waves in YIG exhibit low damping, making it a key material for spintronic and magnonic applications. Notably, glassy magnetic states like spin glass or cluster glass – which involve frozen, disordered spins – are structurally and electronically dichotomous to such long-range ordered states. In spin glasses, frustration and randomness prevent conventional ordering, leading to a distribution of local fields and magnetization directions.

2.1.3 Orbital Photoluminescence: Fe^{3+} and Cr^{3+} Centers

Photoluminescence (PL) from 3*d* transition metals arises from electronic transitions between crystal field-split *d* orbitals, often spin-forbidden but partially allowed via spin-orbit coupling or vibronic mechanisms.

2.1.3.1 Cr^{3+} Luminescence

Cr^{3+} ($3d^3$) ions in an octahedral field display strong photoluminescence, particularly when substituted into wide-gap hosts such as Al_2O_3 (ruby) or $Y_3Al_5O_{12}$ (YAG). The emission may primarily arise from spin allowed $^4T_1 \rightarrow {}^4A_2$ and $^4T_2 \rightarrow {}^4A_2$ transitions and sometimes from the $^2E \rightarrow {}^4A_2$ (spin forbidden) transition. The latter is spin-forbidden but becomes partially allowed due to vibronic coupling and symmetry breaking. The sharpness and intensity of the emission depend on minimal electron–phonon coupling and the rigidity of the host lattice.

2.1.3.2 Fe^{3+} Luminescence

Fe^{3+} ($3d^5$, high-spin) typically exhibits weak luminescence because the transition is both spin- and parity-forbidden. In garnet hosts such as YIG, strong crystal field and magnetic interactions suppress radiative transitions further. Non-radiative decay channels dominate due to extensive overlap with phonon states and potential quenching via magnetic ordering. YAG ($Y_3Al_5O_{12}$), a nonmagnetic garnet, serves as a more suitable host for PL from Fe^{3+} or Cr^{3+} due to the absence of magnetic exchange fields and reduced non-radiative losses. The photonic quality of the host lattice – especially its wide band gap, low phonon energies, and structural rigidity – facilitates efficient radiative transitions.

2.1.4 Competing Effects Between Magnetism and Luminescence

Ordered magnetic sublattices, as seen in YIG, can suppress photoluminescence through magnetic exchange interactions that broaden energy levels and increase non-radiative decay. This electronic dichotomy is rooted in the overlap between magnetic exchange and optical emission processes – both involving the same 3*d* orbitals. Hence, high luminescence and strong magnetic ordering are often mutually exclusive, requiring a trade-off in material design.

In summary, 3*d* orbitals are central to the realization of multifunctional behaviors in transition metal oxides. The inherent tension between conductivity, magnetism, and photoluminescence, arising from shared orbital mechanisms, necessitates a careful balance in crystal chemistry and lattice symmetry. Understanding and manipulating these properties through compositional and structural control is key to the rational design of high-performance multifunctional materials.

2.2 High-Entropy Concept in Materials Design

The notion of high entropy represents a transformative paradigm in materials science, shifting the traditional focus from dilute alloying to multi-component systems where configurational disorder itself becomes a stabilizing factor. The central idea is that a sufficiently large configurational entropy term can outweigh unfavorable enthalpic contributions and promote the stabilization of single-phase solid solutions, even when multiple elements with diverse sizes, charges, and bonding preferences are incorporated. This concept, first introduced in the context of metallic alloys [5], has since expanded into ceramic oxides [6], nitrides [7], carbides [8], and even intermetallic compounds, demonstrating broad applicability across structural and functional materials.

2.2.1 Thermodynamic Foundation

The stability of multi-component solid solutions is governed by the Gibbs free energy of mixing:

$$\Delta G_{mix} = \Delta H_{mix} - TS_{config} \tag{2.3}$$

where ΔH_{mix} is the mixing enthalpy and S_{config} is the configurational entropy. For random substitutional *n* species, S_{config} can be expressed as,

$$S_{config} = -R \sum_{i=1}^{n} x_i \ln x_i \tag{2.4}$$

where x_i representing the mole fraction of the i^{th} element, *R* universal gas constant. For equiatomic compositions ($x_i = 1/n$),

$$S_{config} = R \ln n \tag{2.5}$$

The increase in the logarithmic term implies that configurational entropy rises with the number of elements.

2.2.2 Consequences of Entropy-Driven Disorder

While configurational entropy enhances thermodynamic stability, it simultaneously introduces pronounced local structural and electronic complexity. The distribution of ionic radii, electronegativity, and oxidation states across the lattice generates local distortions, random bond angles, and a spread of crystal field environments. These entropy-driven fluctuations directly

influence electronic bandwidths, exchange interactions, phonon scattering rates, and optical transitions. Rather than being detrimental, such disorder can be harnessed to produce emergent functional responses unattainable in conventional ordered compounds. The entropic design principle has evolved beyond simple stabilization and is now recognized as a versatile tool for engineering multifunctionality. By judiciously selecting elemental combinations, it becomes possible to create single-phase materials that simultaneously exhibit desirable electrical, magnetic, and optical properties.

2.2.2.1 Electrical Functionality

Several high-entropy oxides, specially perovskites [9] often host multiple transition-metal cations with partially filled *d*-orbitals. The coexistence of ions such as Ni, Co, Cu, and Mn modulates electron correlation (U) and hopping integrals (t), leading to tunable transport phenomena. In high-entropy systems, structural disorder can be strategically harnessed as a functional advantage. A compelling example is provided by our study on the perovskite R(Sc/Cr/Fe/Ni/Al)O_3 (discussed in Chapter 4), where we demonstrate that, with the usage of structural disorder, unlike conventional rare-earth nickelates ($RNiO_3$, with R = rare earth) in which Ni exclusively occupies 100% of the B-site lattice, the incorporation of only 20% Ni within a multi-cation B-site framework can still sustain significant electrical conductivity even below room temperature. This highlights how chemical complexity and reduced site-specific occupancy can unlock unconventional transport pathways inaccessible to ordered analogues [10].

2.2.2.2 Magnetic Functionality

The magnetic behavior of high-entropy oxides is profoundly influenced by the configurational disorder inherent to their composition. In contrast to conventional single-cation systems, where the exchange interactions and spin alignments are relatively well-defined, high-entropy systems host a distribution of magnetic ions with varying spin states, orbital occupancies, and ionic sizes. This leads to a statistical mixture of exchange pathways across the lattice. The magnetic interactions can be described by the Heisenberg Hamiltonian:

$$H = -2\sum_{i,j} J_{ij}\mathbf{S}_i \cdot \mathbf{S}_j \tag{2.6}$$

where $\mathbf{S}_i$ and $\mathbf{S}_j$ are the spin operators, J_{ij} is the exchange integral which may take positive (ferromagnetic) or negative (antiferromagnetic) values depending on orbital geometry and overlap. According to the Goodenough-Kanamori-Anderson framework, 180° superexchange between half-filled orbitals usually favors antiferromagnetic order, while near-orthogonal orbital overlap may favor ferromagnetism. In high-entropy oxides, the coexistence of multiple cations ensures that the set of J_{ij} values span a broad distribution rather than converging on a single dominant interaction. This produces exchange frustration, preventing uniform long-range order and often leading to unconventionally disordered magnetic states [11].

From a functional perspective, this entropy-induced magnetic complexity is technologically valuable. The coexistence of multiple exchange interactions can broaden magnetic transitions, yielding a distributed entropy change that enhances the magnetocaloric effect, as estimated from Maxwell's relation:

$$\Delta S_M(T,H) = \mu_0 \int_0^H \left(\frac{\partial M}{\partial T}\right)_{H'} dH' \tag{2.7}$$

Such behavior is promising for magnetic refrigeration near room temperature. Furthermore, the tunability of coercivity, remanence, and damping properties through compositional disorder makes these materials attractive in spintronics and magnonics, where control over spin dynamics is crucial. In summary, configurational entropy in high-entropy oxides not only stabilizes phases but also engineers magnetic frustration and disorder, enabling the realization of exotic magnetic ground states with functional applications.

2.2.2.3 Photoluminescence in High-Entropy Oxides

Photoluminescence (PL) in high-entropy oxides represents a unique convergence of configurational disorder, crystal-field effects, and multi-ion luminescence centers. In conventional crystalline hosts, the PL response of a dopant or transition-metal ion is primarily determined by well-defined local environments that fix the crystal-field splitting, site symmetry, and nonradiative relaxation pathways. By contrast, high-entropy systems generate a distribution of local environments due to random cation substitution and lattice distortion, producing broadened emission spectra, and multi-band luminescence. The origin of PL lies in the excitation of electrons to higher electronic states, followed by radiative recombination. For transition-metal ions in octahedral coordination, excitation across the crystal-field gap can be described by the energy separation,

$$\Delta_{oct} = 10Dq \tag{2.8}$$

which splits the five d-orbitals into lower-energy t_{2g} and higher-energy e_g states. The emission energy depends on the relaxation from excited states (often charge-transfer or intra-d transitions) back to the ground configuration. In high-entropy oxides, Δ_{oct} should vary due to distortions in bond length and angle, leading to an inhomogeneous distribution of emission energies. This manifests as line broadening and, in many cases, the emergence of multiple overlapping PL peaks. Another key factor is the suppression of nonradiative pathways. In conventional hosts, thermal quenching of PL arises from multiphonon relaxation processes, where excited-state energy is dissipated into lattice vibrations. The rate of nonradiative decay W_{nr} depends exponentially on the maximum phonon energy $\hbar\omega_{max}$ and the energy gap ΔE between emitting and ground states:

$$W_{nr} = C\exp\left(-\frac{\alpha\Delta E}{\hbar\omega_{max}}\right) \tag{2.9}$$

where α denotes electron-phonon coupling. In high-entropy oxides, phonon spectra are broadened and fragmented due to mass and bond-strength disorder, which should reduce the efficiency of multiphonon relaxation. This should prolong excited-state lifetimes and increase PL efficiency.

2.3 Perovskite Structure

The perovskite structure, with the general formula ABO_3, is one of the most versatile and extensively studied frameworks in solid-state physics, chemistry and materials science. Its archetype, calcium titanate ($CaTiO_3$), crystallizes in a cubic structure at high temperatures, where the A-site cation occupies a 12-fold coordinated cuboctahedral cavity, the B-site cation resides in a 6-fold coordinated octahedral environment, and oxygen atoms form corner-sharing BO_6 octahedra. The perovskite lattice is distinguished by its ability to host a vast range of cations at both the A and B sites, spanning alkali, alkaline earth, rare-earth, and transition metals. This

remarkable chemical flexibility makes perovskites ideal candidates for incorporating multiple principal elements in high-entropy configurations.

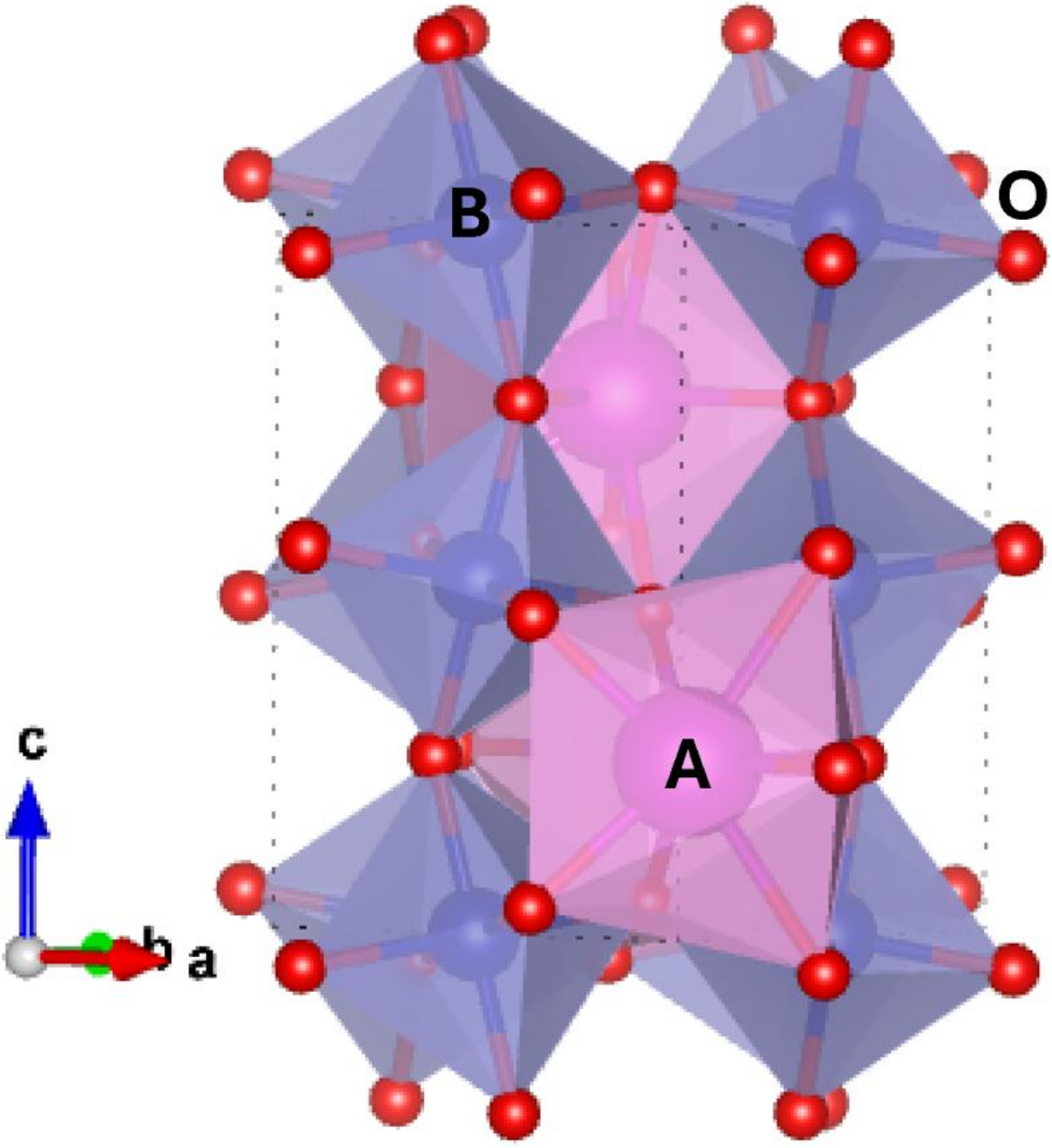

Figure 2.1: A prototype orthorhombic perovskite with *Pnma* space group.

A widely used descriptor for predicting the stability of perovskite phases is the Goldschmidt tolerance factor, defined as:

$$t = \frac{r_A + r_O}{\sqrt{2}(r_B + r_O)} \tag{2.10}$$

where r_A, r_B, and r_O represent the ionic radii of the A-site cation, B-site cation, and oxygen anion, respectively. For an ideal cubic perovskite, $t \approx 1$. Deviations from unity indicate structural distortions: $t < 1$ generally results in octahedral tilting or orthorhombic/rhombohedral distortions, while $t > 1$ can destabilize the perovskite framework in favor of hexagonal or layered variants. In the context of high-entropy design, the effective tolerance factor is calculated using the average ionic radii of multiple cations at each sublattice. The distribution of radii (variance in r_A or r_B) is equally important, as it quantifies lattice strain introduced by size mismatch.

2.4 Garnet Structure

The garnet lattice occupies a special position in solid-state chemistry because of its highly ordered yet compositionally flexible framework. The general formula $A_3B_2C_3O_{12}$, reflects a three-sublattice architecture where cations occupy distinct coordination environments: the A-sites exhibit dodecahedral coordination with eight surrounding oxygen atoms, the B-sites adopt octahedral coordination, and the C-sites occupy tetrahedral environments. This hierarchy of polyhedra generates a three-dimensional network of corner- and edge-sharing units that not only stabilizes a wide family of oxides but also allows subtle tuning of their functional properties by targeted cation substitution.

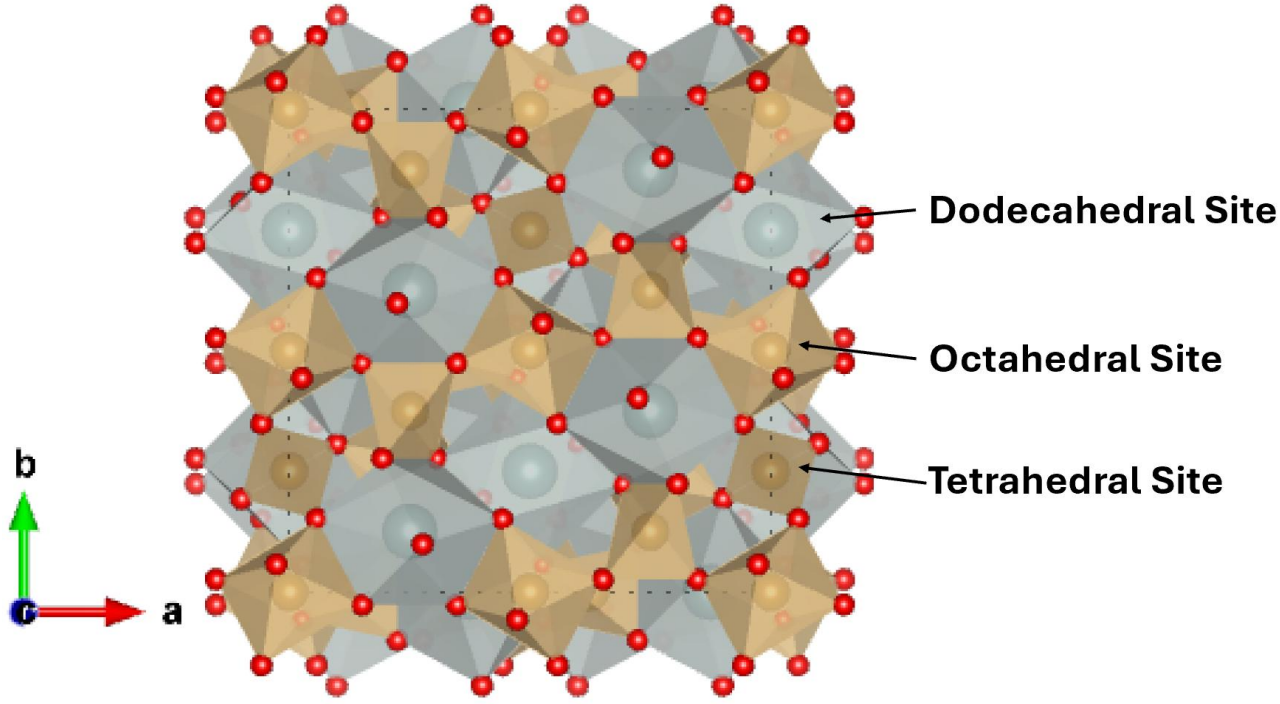

Figure 2.2: A prototype YIG structure with multiple different sublattices.

The yttrium iron garnet ($Y_3Fe_5O_{12}$, YIG) has long been the most notable member of this family. It is a magnetic insulator in which Fe^{3+} ions occupy both octahedral and tetrahedral sites, forming two sublattices that are antiferromagnetically coupled. The imbalance of spins between these two sublattices produces a net ferrimagnetic order. Y^{3+} in contrast, is confined to the large dodecahedral cavities and remains magnetically inactive, effectively "skeletonizing" the structure while leaving the Fe^{3+} network to dictate the magnetic response. This site selectivity imparts rigidity to the lattice, as the dodecahedral sites are largely inaccessible to other cations, but also highlights the Fe^{3+} sublattice as the primary arena for chemical substitution and functional tailoring.

The Fe^{3+} sublattice is the most substitutionally versatile, as it can host a variety of trivalent cations with differing sizes, electronic configurations, and bonding preferences. Small trivalent ions such as Al^{3+} and Ga^{3+}, can replace Fe^{3+} across both octahedral and tetrahedral sites. Larger trivalent ions, such as Sc^{3+} and In^{3+}, fit only partially into the octahedral network, expanding the local coordination polyhedra and weakening interionic interactions. Cr^{3+} introduces yet another layer of complexity, as it not only perturbs magnetic coupling but also contributes its own characteristic *d-d* optical transitions.

CHAPTER 3
EXPERIMENTAL DETAILS

3.1 Solid State Synthesis

The synthesis of the high-entropy oxides studied in this work was carried out via a conventional solid-state reaction route, a method selected for its reliability in producing dense, polycrystalline materials with controlled stoichiometry. The synthesis of high-entropy perovskites demands a heightened level of procedural rigor, particularly in terms of iterative homogenization and diffusion-driven equilibration – because the random occupation of multiple cations necessitates overcoming both kinetic and enthalpic barriers to cation redistribution.

As a representative example, the perovskite $Pr(Sc_{0.2}Cr_{0.2}Fe_{0.2}Ni_{0.2}Al_{0.2})O_3$ was synthesized starting from binary oxides. High-purity precursors included Pr_2O_3 (A-site) and Sc_2O_3, Cr_2O_3, Fe_2O_3, NiO, and Al_2O_3 (B-sites). The overall reaction may be expressed as:

$$Pr_2O_3 + 0.2\,Sc_2O_3 + 0.2\,Cr_2O_3 + 0.2\,Fe_2O_3 + 0.4\,NiO + 0.2\,Al_2O_3 \longrightarrow 2\,Pr(Sc_{0.2}Cr_{0.2}Fe_{0.2}Ni_{0.2}Al_{0.2})O_3$$

All precursors were dried at 200 °C to remove adsorbed moisture and carbonates, weighed to ±0.01 mg precision, and handled in a desiccated environment to prevent contamination.

The oxides were combined and subjected to high-energy milling in a SPEX 8000M shaker mill using methacrylate vial and balls (at least of three different diameters). Milling for 90–120 minutes induced microstructural refinement, enhanced defect concentrations, and reduced the characteristic diffusion distance. These factors directly influence the rate of solid-state reaction, which is generally governed by [12]:

$$\tau \propto \frac{d^2}{D} \tag{3.1}$$

where τ is the characteristic reaction time, d is the diffusion distance, and D is the diffusion coefficient. The reduction of particle size via milling, therefore, significantly accelerates reaction kinetics. Following milling, powders were hand-ground in an agate mortar for 45–60 minutes, which provided additional homogenization and minimized local concentration gradients.

The homogenized powders were calcined in an MTI 1700 box furnace, beginning with a 10 h dwell at 1250 °C. The furnace ramp rate was maintained at 5 °C/min to prevent thermal shock. At elevated temperatures, the reaction between adjacent oxide grains follows a diffusion-controlled mechanism, where ionic species migrate across boundaries to form intermediate phases. The rate of diffusion is described by Fick's second law [12]:

$$\frac{\partial C}{\partial t} = D\frac{\partial^2 C}{\partial x^2} \tag{3.2}$$

where C is concentration, t is time, x is distance, and D as described above is the diffusion coefficient, which follows an Arrhenius dependence:

$$D = D_0 \exp\left(-\frac{Q}{RT}\right) \tag{3.3}$$

Here, Q is the activation energy for diffusion, R is the ideal gas constant, and T is the absolute temperature. Successive calcinations or sintering at 1250 °C progressively increased D, thereby accelerating reaction completion. After each calcination, powders were reground to break up agglomerates, reduce diffusion distances again, and reset the system for more complete reaction. This iterative calcination-grinding loop is crucial for high-entropy compositions, where multiple cations of disparate sizes and charges must diffuse and occupy equivalent crystallographic sites. The mechanistic description of such reactions can also be modeled by the shrinking-core model, wherein the reaction initiates at the particle surface and progresses inward, leaving behind a product layer that may inhibit further diffusion. Repeated grinding thus disrupts the partially reacted "shell" and exposes unreacted cores, enabling more complete reaction upon further calcination.

Once a single-phase pattern was confirmed via powder XRD after the ~1250 °C calcinations, the powder was pelletized (~300 MPa) into 12 mm discs and sintered at 1350–1500 °C for 10–24 h in air. Sintering densification is driven by minimization of surface free energy, with mass transport occurring through mechanisms such as lattice diffusion, grain boundary diffusion, and surface diffusion.

3.1.1 Hot Pressing

To achieve high-density bulk ceramics suitable for transport and mechanical measurements, the single-phase high-entropy oxide powders were subjected to densification using a uniaxial hot press (OXY-GON Industries, Inc.). This method was selected over conventional pressure-less sintering to overcome the limitations of grain coarsening and porosity retention that frequently accompany high-entropy oxide systems due to sluggish diffusion kinetics.

Ground powders were loaded into a graphite die assembly lined with graphite foil to minimize frictional stress and contamination. The system was evacuated to a low-pressure environment and subsequently backfilled with flowing argon gas, which served two purposes: (i) suppressing volatilization of volatile cations such as Ni and Cr, and (ii) minimizing oxidation or reduction deviations during high-temperature processing. The samples were hot-pressed at 1500 °C under a uniaxial load of 37.5 MPa for 2–4 h, with heating and cooling rates maintained at ~10 °C/min. The simultaneous application of temperature and pressure accelerated mass transport through enhanced atomic mobility, thereby promoting pore elimination. The densification rate ($\dot{\rho}$) under hot-pressing conditions can be modeled as [13]:

$$\dot{\rho} = \frac{A\sigma^n}{d^p} \exp\left(-\frac{Q}{RT}\right) \tag{3.4}$$

where ρ is the relative density, σ is the applied stress, d is grain size and A, n, p are material constants. The applied load reduces the effective diffusion distance by collapsing pores, while high temperature lowers the exponential barrier for ionic transport.

3.1.2 Post-Processing Annealing

Following hot pressing, samples were removed from the graphite die and subjected to a stress-relief anneal in an MTI 1700 °C box furnace at 1500 °C in air for 10 h. This step served multiple critical functions:

1. Residual Stress Reduction: Rapid densification during hot pressing introduces anisotropic stresses that can degrade mechanical integrity. Air annealing allowed atomic rearrangements that relieved such stress.
2. Carbon Removal: Contact with graphite tooling can leave residual carbon films or diffuse light carbon into the pellet surface. Prolonged annealing in oxygen-rich air reoxidized and eliminated such contamination.
3. Stoichiometric Equilibration: The anneal re-established full oxygen stoichiometry in the perovskite lattice, ensuring reliable property measurements.

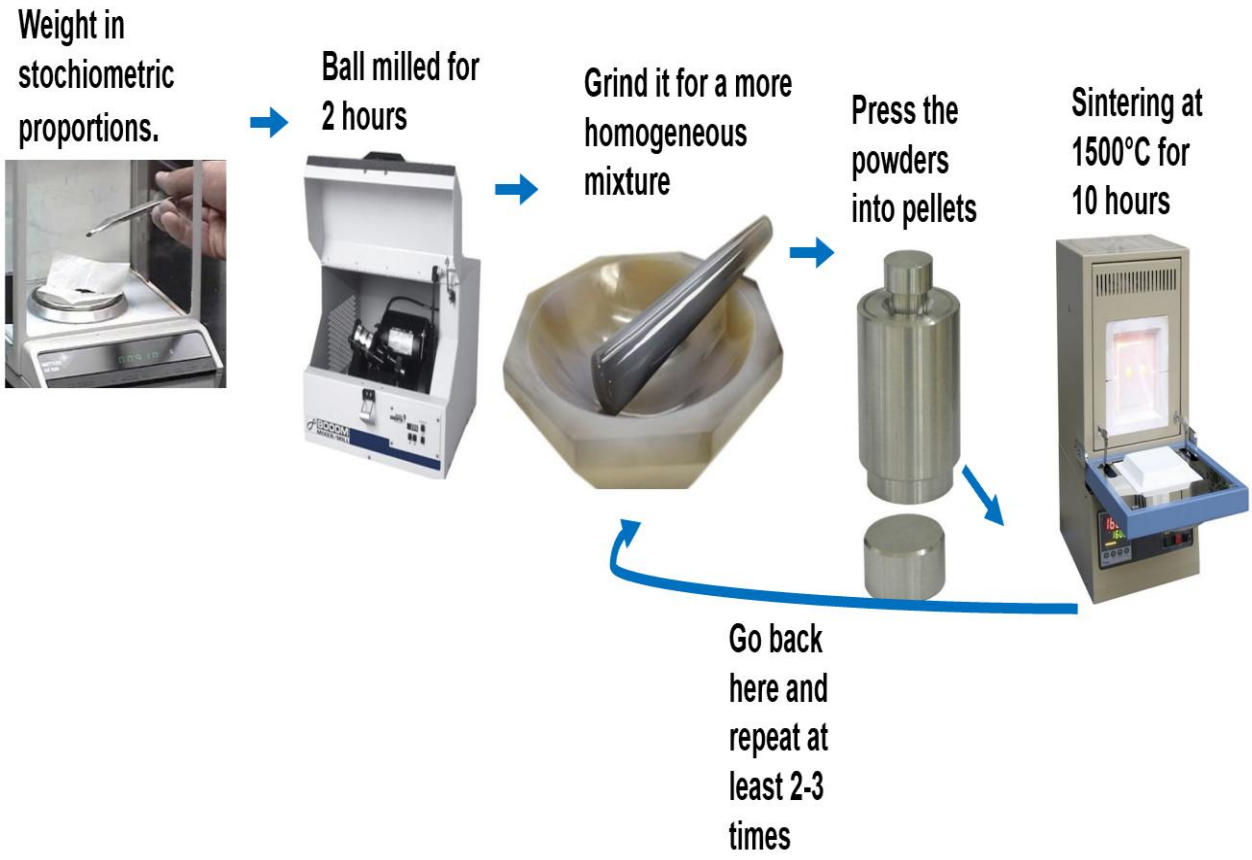

Figure 3.1: Sketch of the general solid state reaction steps.

3.2 Structural Characterization by X-ray Diffraction

X-ray diffraction (XRD) is one of the most powerful techniques for elucidating the crystal structure of polycrystalline solids, providing information on symmetry, lattice constants, phase assemblage, and microstructural features. The technique is governed by Bragg's Law:

$$n\lambda = 2d_{hkl}\sin\ \theta \tag{3.5}$$

where n is the order of reflection, λ is the wavelength of the incident X-ray, d_{hkl} is the interplanar spacing corresponding to the (hkl) lattice planes, and θ is the angle of incidence. For cubic systems, the interplanar spacing is related to the lattice constant 'a' by:

$$d_{hkl} = \frac{a}{\sqrt{h^2+k^2+l^2}} \tag{3.6}$$

In more distorted perovskites, particularly those adopting orthorhombic symmetry (*Pbnm/Pnma* space group), the relationship becomes:

$$\frac{1}{d_{hkl}^2} = \left(\frac{h^2}{a^2}\right) + \left(\frac{k^2}{b^2}\right) + \left(\frac{l^2}{c^2}\right) \tag{3.7}$$

where a, b, and c are the orthorhombic lattice parameters. Systematic refinement of diffraction peak positions thus allows determination of not only average cell dimensions but also subtle distortions (e.g., octahedral tilting, Jahn–Teller distortions) that are central to the physics of perovskites.

The laboratory-based XRD measurements in this study employed the *Bragg–Brentano* geometry, in which the incident and diffracted angles are equal (θ–2θ configuration). This geometry provides high-intensity reflections and excellent peak statistics for polycrystalline samples, making it ideal for Rietveld refinement.

3.2.1 Rietveld Refinement

The Rietveld method is fundamentally a non-linear least-squares fitting procedure, in which the calculated diffraction pattern is iteratively adjusted to minimize the difference between observed y_i^{obs} and calculated y_i^{calc} intensities at each step of the diffraction profile. The weighted profile R-factor R_{wp} quantifies the agreement between observed and calculated intensities [14]:

$$R_{wp} = \left[\frac{\sum_i w_i\left(y_i^{obs}-y_i^{calc}\right)^2}{\sum_i w_i\left(y_i^{obs}\right)^2}\right]^{1/2} \tag{3.8}$$

with w_i representing statistical weights. Structural parameters are refined by adjusting atomic positions, occupancies, and thermal vibrations in the structure factor equation:

$$F_{hkl} = \sum_j\ f_j \exp\left[2\pi i\left(hx_j + ky_j + lz_j\right)\right]\exp\left(-B_j\frac{\sin^2\theta}{\lambda^2}\right) \tag{3.9}$$

where f_j is the atomic scattering factor, (x_j, y_j, z_j) are atomic positions, and B_j is the Debye–Waller factor.

Two refinement suites were employed for cross-validation:

- *HighScore Plus (PANalytical):* integrates seamlessly with Empyrean instruments, enabling phase identification, background fitting, and Rietveld refinement with automated workflows. Its integration with ICDD databases accelerates phase analysis.
- *GSAS-II:* an open-source refinement framework offering advanced control of anisotropic strain, preferred orientation, and multiphase refinement. It is particularly advantageous for high-entropy oxides where subtle disorder and micro-strain effects complicate standard analysis.

Figure 3.2: PANalytical EMPYREAN XRD instrument setup.

3.3 X-ray Total Scattering and Pair Distribution Function (PDF) Analysis

Unlike conventional diffraction, which probes long-range crystallographic order, X-ray total scattering provides access to both Bragg peaks and diffuse scattering. This enables the simultaneous characterization of long-range periodicity and local, short-range structural correlations—essential for high-entropy perovskites where local distortions and cation disorder play a pivotal role in functional behavior. The experimental observable is the scattering intensity, *I(Q)*, as a function of the scattering vector magnitude, $Q=4\pi\sin(\theta)/\lambda$, where λ is the incident X-ray wavelength and 2θ is the scattering angle. The normalized structure function is obtained as [15]:

$$S(Q) = \frac{I(Q)-I_{bkg}(Q)}{\langle f(Q)\rangle^2} \tag{3.10}$$

where $I_{bkg}(Q)$ is the background contribution (e.g., from the Kapton capillary) and $\langle f(Q)\rangle$ is the average atomic scattering factor. The atomic pair distribution function (PDF) is then extracted through Fourier transformation [15, 16]:

$$G(r) = \frac{2}{\pi}\int_{Q_{min}}^{Q_{max}} Q[S(Q)-1]\sin(Qr)dQ \tag{3.11}$$

where *r* is the real-space distance. Peaks in *G(r)* directly correspond to atomic pair correlations, allowing bond lengths, coordination numbers, and local distortions to be quantified independent of long-range periodicity.

Powder samples were finely ground and packed into Kapton tube capillaries. Experiments were conducted at the *28-ID-2 (XPD)* beamline at the *National Synchrotron Light Source-II (NSLS-II)*, *Brookhaven National Laboratory*. Measurements utilized a high-energy X-ray beam (λ=0.1665 Å, ~74.4 keV) to access large *Q*-ranges, enabling high-resolution real-space transforms. Data were collected at room temperature with an exposure time of 10 s per sample, balancing high signal-to-noise with minimal beam damage.

Background-corrected total scattering data were normalized and Fourier transformed using the *PDFgetX2 (v2.1.1)* software package, producing structure functions *S(Q)* and corresponding pair distribution functions *G(r)*. The accessible *Q*-range spanned from 0.5 Å^{-1} to 23 Å^{-1}, ensuring high-quality transforms with real-space resolution down to ~0.1 Å. Refinements of the PDF data were carried out using *PDFgui*, which fits the experimental *G(r)* with structural models by minimizing the residual function:

$$R_w = \frac{\sum_i w_i\left[G^{obs}(r_i)-G^{calc}(r_i)\right]^2}{\sum_i w_i\left[G^{obs}(r_i)\right]^2} \tag{3.12}$$

where $G^{obs}(r_i)$ and $G^{calc}(r_i)$ are the observed and calculated pair distribution functions at distance r_i, and w_i are weighting factors. Refinable parameters included lattice constants, atomic displacement parameters, and site occupancies. By fitting across different *r*-ranges, both local distortions (short *r*) and average crystallographic order (long *r*) were assessed. Additionally, radial distribution functions (RDFs) for individual atomic pairs were derived to analyze specific bond lengths (e.g., B–O, A–O, A-B) and their distributions, providing insight into the degree of disorder inherent in the high-entropy lattice.

3.4 Scanning Electron Microscopy (SEM)

Scanning electron microscopy (SEM) is a versatile tool for examining the microstructural features of ceramic and polycrystalline materials. Unlike optical microscopy, SEM utilizes a focused beam of high-energy electrons (typically 1–30 kV) to interact with the sample surface, producing a variety of secondary signals. The most exploited are secondary electrons (SE), which provide topographical contrast, and backscattered electrons (BSE), which are sensitive to atomic number (Z) contrast. The spatial resolution R achievable in SEM is governed by the electron probe size and interaction volume, which depends strongly on the accelerating voltage and sample composition. The effective resolution can be approximated by:

$$R \approx 0.61 \frac{\lambda_e}{\alpha} \tag{3.13}$$

where λ_e is the de-Broglie wavelength of the electron and α is the semi-angle of convergence of the electron beam. At typical operating voltages of 15–20 kV, SEM achieves resolutions down to a few nanometers for conductive specimens.

3.4.1 Energy-Dispersive X-ray Spectroscopy (EDS)

Energy-dispersive X-ray spectroscopy (EDS), integrated within the SEM, was employed to assess elemental composition and cation distribution. Characteristic X-rays are generated when incident electrons ionize inner-shell electrons of atoms, followed by electronic transitions from higher shells. The energy of the emitted X-ray corresponds to the energy difference between electronic states and is unique to each element. The intensity of an X-ray peak for element i is proportional to its concentration:

$$I_i = kC_i\omega_i f_i(Z, A, F) \tag{3.14}$$

where, C_i is the atomic concentration, ω_i is the fluorescent yield, f_i is a correction factor accounting for atomic number (Z), absorption (A), and fluorescence (F) effects, and$k$ is an instrumental constant.

Figure 3.3: Zeiss EVO SEM with integrated EDS.

3.5 Electrical Transport Measurements

The electrical resistance, R of the synthesized samples was measured by four-probe configuration. Samples were cut and polished into rectangular bars with typical dimensions of 3–5 mm in length, 1.5–2.5 mm in width and 0.5–1 mm in both width and thickness. Measurements were performed as a function of temperature, spanning from 2-350 K, under zero applied magnetic field conditions using a Quantum Design DynaCool Physical Property Measurement System (PPMS). A constant excitation current *I* is passed longitudinally through the outer two contacts, while the voltage drop *V* is simultaneously recorded across the inner two contacts. The intrinsic material resistivity , ρ, is obtained from the conventional equation,

$$\rho = R \cdot \frac{A}{L} \tag{3.15}$$

where A is the cross-sectional area of the sample bar and L is the length between electrical contacts. Since most specimens exhibit extremely high impedances, particularly at low temperatures, a two-probe AC impedance configuration was also employed for higher accuracy. The experiments were conducted on similar dimensioned sample fragments using the PPMS with an electrical transport option (ETO). In this technique, an alternating voltage V_{AC} is applied across the two electrodes while the resultant current I_{AC} is measured. The complex impedance *Z* is then obtained as:

$$Z(\omega) = \frac{V_{AC}(\omega)}{I_{AC}(\omega)} = R(\omega) + jX(\omega) \tag{3.16}$$

where $R(\omega)$ is the real part corresponding to the resistive component, and $X(\omega)$ is the imaginary part associated with capacitive or inductive contributions. The frequency dependence of the impedance provides insight into both charge transport and dielectric relaxation processes.

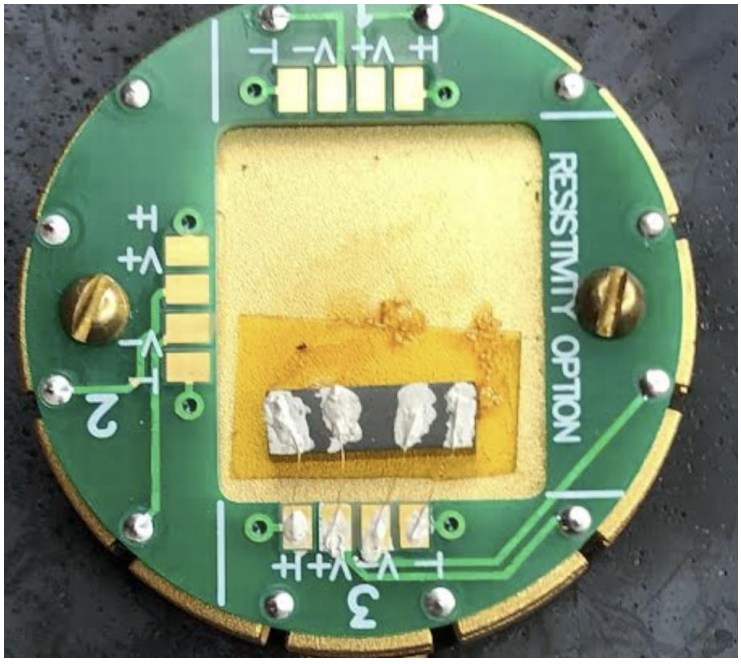

Figure 3.4: A sample connected in a four-probe configuration.

3.6 Magnetic Measurements

Magnetic characterization was performed using a Quantum Design MPMS3 SQUID-VSM magnetometer, which integrates the high sensitivity of superconducting quantum interference detection with the dynamic response capability of a vibrating sample magnetometer. In this configuration, the sample is rigidly mounted on a non-magnetic sample holder and positioned within the bore of a superconducting solenoid magnet, which generates fields up to 7 T with high homogeneity which provides ultrahigh sensitivity for detecting very small magnetic moments. Magnetization *M(T)* was recorded as a function of temperature, following both zero-field cooling (ZFC) and field cooling (FC) protocols.

In the ZFC protocol, the specimen was initially cooled to 2 K in the absence of any externally applied field. After reaching the base temperature, a magnetic field of $\mu_0 H$ = 1000 Oe for the perovskites and $\mu_0 H$ = 100 Oe for the garnet samples were applied. and the magnetization was measured while warming the sample back to 400 K. For the FC protocol, the specimen was cooled to 2 K in the presence of an applied magnetic field (up to 5 T). Magnetization data were subsequently recorded upon warming under the same $\mu_0 H$ = 1000 Oe for the perovskites and $\mu_0 H$ = 100 Oe for the garnets. A comparison of ZFC and FC curves provides direct insight into magnetic irreversibility and phenomena such as spin-glass freezing, superparamagnetic blocking, or canted antiferromagnetism.

Isothermal magnetization *M(H)*, was also measured at different selected temperatures by sweeping the applied field from $\mu_0 H$ = 0 to 7 T. This enabled determination of the field-dependent response, including the approach to saturation and the contribution of any paramagnetic background.

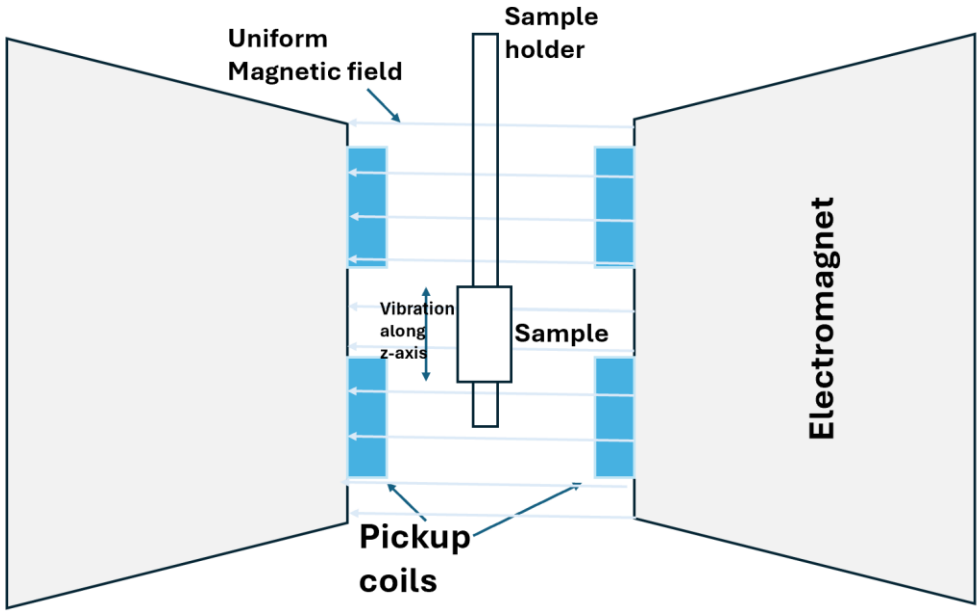

Figure 3.5: Schematic of a VSM setup.

3.6.1 AC susceptibility measurements

The AC susceptibility measurements were performed using the AC Measurement System (ACMS) option of a Quantum Design DynaCool Physical Property Measurement System (PPMS). Approximately ~40 mg of perovskite and ~10 mg of polycrystalline garnet sample was mounted during respective measurements for analysis. An AC excitation field of 10 Oe was applied for the perovskite samples; however a lower 0 Oe AC field was applied for the garnets, and the measurements were conducted across a broad frequency window to capture relaxation dynamics. To ensure repeatable results, the auto-centering function of the PPMS sample stage was disabled, thereby maintaining consistent positioning of the sample throughout the measurement sequence. The applied oscillating magnetic field is given by,

$$H(t) = H_0 \cos(\omega t) \tag{3.17}$$

Notably, with this applied AC field, the magnetization response of the material is not instantaneous but lags behind due to relaxation processes. Which can be expressed as,

$$M(t) = \chi'(\omega) H_0 \cos(\omega t) + \chi''(\omega) H_0 \sin(\omega t) \tag{3.18}$$

where, $\chi'(\omega)$ denotes the real (in-phase) component of the AC susceptibility, reflecting the reversible response of the system, while $\chi''(\omega)$ represents the imaginary (out-of-phase) component, associated with dissipative processes such as magnetic relaxation or domain wall motion.

3.7 Heat Capacity Measurements

The heat capacity of a solid is a fundamental thermodynamic property that reflects the amount of energy required to produce a unit change in temperature. Because it is directly related to fluctuations in entropy and internal energy, it serves as a sensitive probe of structural, electronic, and magnetic transitions. Sharp features or anomalies in the temperature dependence of the heat capacity often signal phase transitions, such as the onset of magnetic order or structural instabilities – that may not be as clearly discernible in bulk magnetization or susceptibility measurements.

For this work, heat capacity measurements were performed using the relaxation method integrated into the Quantum Design DynaCool PPMS system. The heat capacity module of the PPMS employs a microcalorimeter mounted on a sample puck, enabling measurements over the entire accessible temperature and magnetic field range of the system. The experiment is conducted under high-vacuum conditions to ensure proper thermal isolation. During a run, a controlled heat pulse is applied to the specimen, and the resulting temperature evolution is tracked following the principles of the semi-adiabatic relaxation method. Analytical routines then model the thermal circuit and fit the recorded temperature profile, allowing extraction of the sample's heat capacity [17].

To isolate the intrinsic contribution of the specimen, preliminary measurements are first carried out on the empty platform with a thin layer of Apiezon N-grease (2 K to 300 K) or H-grease (300 K-400 K) used as a thermal interface. This run provides the so-called addenda, consisting of the platform, grease, and wiring contributions. Subsequent measurements with the specimen mounted allow the net sample heat capacity to be determined by subtracting the addenda from the total response.

3.8 Photoluminescence Measurements

Photoluminescence (PL) characterization was performed using a HORIBA Fluorolog-QM-11 spectrofluorometer, a versatile system designed for high-sensitivity luminescence studies. The setup was configured to allow both room-temperature and variable-temperature measurements, enabling detailed investigation of optical transitions across a broad thermal range.

The excitation source consisted of a pulsed ultraviolet laser operating at a wavelength of 343 nm. The laser was operated at repetition rates near 25 Hz with an average output power between 8–10 W, providing sufficient photon flux to efficiently excite the samples. To ensure spectral purity, a 343 nm bandpass filter was inserted directly into the excitation path to remove residual background wavelengths. The excitation beam was passed through a single monochromator equipped with a 1200 gr/mm diffraction grating, which allowed precise wavelength selection. Focusing optics were used to achieve a beam spot size of approximately 0.5 mm in diameter on the sample surface, corresponding to an excitation intensity of ~50 mW/cm².

The emitted PL signal was collected in a right-angle geometry and directed into a single emission monochromator, also configured with a 1200 gr/mm grating to ensure high spectral resolution. A photomultiplier photon detector (PPD), operated in high-sensitivity mode, was employed for signal detection. Data collection and instrument control were carried out using FelixFL software. Typical acquisition parameters included slit widths of 5–10 nm (100–200 μm), yielding a spectral resolution of approximately 1 nm across an emission window spanning 250–650 nm. Each spectrum was obtained with an integration time of 10–30 seconds, and in most cases averaged over three to ten consecutive scans to improve the signal-to-noise ratio.

For temperature-dependent studies, the samples were mounted in a closed-cycle helium cryostat, permitting measurements between 5 K and 295 K. This configuration enabled the observation of thermally activated processes, excitonic recombination, and defect-related emission features with high reproducibility. At room temperature, the specimens were positioned horizontally on a flat sample stage for ambient-condition measurements. To ensure accurate comparison of relative intensities across different runs, the PL intensity was calibrated against a standard reference light source.

This combination of high-power pulsed excitation, precise monochromator control, and sensitive photon detection provided a robust framework for characterizing the intrinsic optical properties of the samples, including their defect emission signatures, band-edge luminescence, and temperature-dependent recombination mechanisms.

3.9 Resonant Ultrasound Spectroscopy Measurements

Resonant ultrasound spectroscopy (RUS) is a non-destructive technique [18] that is based on measuring the natural mechanical resonances of a specimen and using them to extract the complete set of elastic moduli.

When a solid body with free surfaces is excited mechanically, it vibrates at characteristic frequencies determined by its shape, dimensions, and elastic constants. Therefore, experimental determination of the resonant frequencies, along with the sample's dimensions, allows us to determine the full elastic tensor of a solid material. Samples are typically shaped into a rectangular parallelepiped or cylinder, and the resonances can be tracked as a function of temperature and/or magnetic field, allowing to detect structural and magnetic transitions.

For polycrystalline (isotropic) materials, the stiffness tensor reduces to only two independent constants. RUS measurements for these materials will yield the longitudinal modulus c_{11} and the shear modulus c_{44}, which allows determination of the Young's and Bulk modulus.

CHAPTER 4
PROPERTIES OF RE(Sc/Cr/Fe/Ni/Al)O_3

4.1 Introduction

This chapter examines the average structural, electronic, magnetic, thermodynamic, and elastic characteristics of the RE(Sc/Cr/Fe/Ni/Al)O_3 (RE = rare-earth) perovskite system. Portions of this work have been previously reported in the publication "*Synthesis and properties of rare-earth high-entropy perovskite* by Rubayet Tanveer, Dylan Windsor, Sean Drewry, Katharine Page, Haixuan Xu, Veerle Keppens, and William J. Weber, published in Applied Physics Letters" [10].

4.2 X-ray Diffraction (XRD) Analysis

The phase composition and crystallographic framework of RE(Sc/Cr/Fe/Ni/Al)O_3 (RE = La–Gd, including the extended 11-cation formulation) were examined by powder X-ray diffraction (XRD). Figure 4.1(a) displays representative diffraction patterns across the rare-earth series. All synthesized compounds adopt the orthorhombic *Pnma* perovskite structure, which is isostructural with well-known orthoferrites and orthochromites.

The absence of secondary-phase reflections confirms that the materials were single-phased within the detection limits of the technique. This observation aligns closely with previous reports of orthorhombic high-entropy perovskites [9, 19, 20], thereby validating the robustness of the adopted synthesis approach for stabilizing complex multi-cationic systems in a perovskite lattice.

Closer inspection of the diffraction patterns reveals systematic changes in peak positions and line shapes across the lanthanide series.

Progressive splitting of several characteristic reflections is observed as the A-site cation varies from La to Gd (clearly noticeable in the (121) reflection). This behavior directly reflects the increased lattice distortion induced by the the gradual reduction of the rare-earth ionic radii. Such distortions decrease the overall crystallographic symmetry, steering the structure further away from the higher symmetry tetragonal structure to a more distorted orthorhombic framework.

Quantitative analysis through Rietveld refinement provides deeper insight into these structural trends. As summarized in Figure 4.1(b) and Table 4.1, the lattice parameters b and c exhibit a continuous contraction of 1-2% across the series. The change in lattice parameter a is much more subtle (less than 1%) and are indicative of a small expansion in that direction.

Taken together, the XRD analysis confirms not only the phase purity of the synthesized RE(Sc/Cr/Fe/Ni/Al)O_3 perovskites but also establishes a correlation between rare-earth ionic size and symmetry lowering. These results set the structural foundation for understanding the subsequent property variations discussed in later sections.

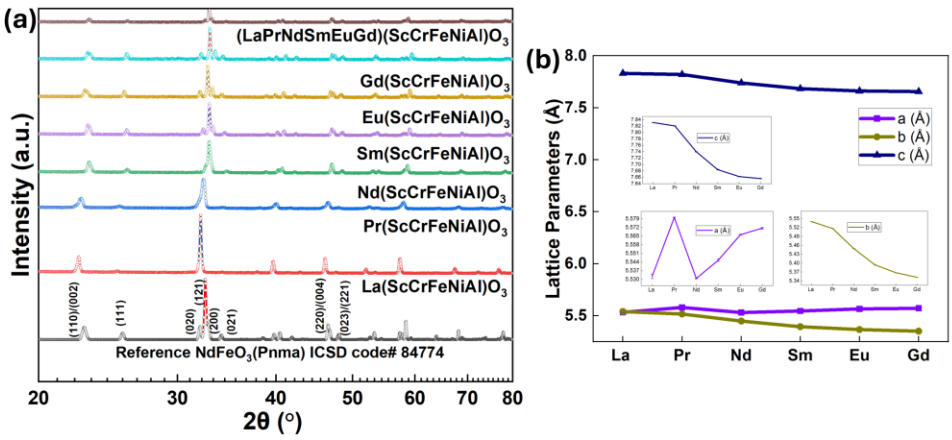

Figure 4.1: (a) Powder X-ray diffraction profiles of RE(Sc/Cr/Fe/Ni/Al)O_3 high-entropy perovskites, all indexed with the orthorhombic *Pnma* space group. For reference, the diffraction pattern of $NdFeO_3$ [21] is included to illustrate the structural archetype. (b) Variation of the refined lattice parameters as a function of the A-site rare-earth cation radius, highlighting the systematic evolution driven by lanthanide contraction.

Table 4.1: Rietveld refined lattice parameters of RE(Sc/Cr/Fe/Ni/Al)O_3 perovskites.

List of Compositions	Associated Phases	Lattice Parameters (Å)
La(Sc/Cr/Fe/Ni/Al)O_3	Orthorhombic (Pnma)	a = 5.5325 ± 0.0019 b = 5.5399 ± 0.0007 c= 7.8309 ± 0.0009
Pr(Sc/Cr/Fe/Ni/Al)O_3	Orthorhombic (Pnma)	a = 5.5801 ± 0.0003 b = 5.5166 ± 0.0003 c = 7.8203 ± 0.0004
Nd(Sc/Cr/Fe/Ni/Al)O_3	Orthorhombic (Pnma)	a = 5.5308 ± 0.0003 b = 5.4491 ± 0.0005 c = 7.7397 ± 0.0003
Sm(Sc/Cr/Fe/Ni/Al)O_3	Orthorhombic (Pnma)	a = 5.5456 ± 0.0009 b = 5.3944 ± 0.0013 c = 7.6838 ± 0.0009
Eu(Sc/Cr/Fe/Ni/Al)O_3	Orthorhombic (Pnma)	a = 5.5662 ± 0.0004 b = 5.3676 ± 0.0004 c = 7.6623 ± 0.0006
Gd(Sc/Cr/Fe/Ni/Al)O_3	Orthorhombic (Pnma)	a = 5.5715 ± 0.0007 b =5.3521 ± 0.0006 c =7.6560 ± 0.0009
(La/Pr/Nd/Sm/Eu/Gd) (Sc/Cr/Fe/Ni/Al)O_3	Orthorhombic (Pnma)	a = 5.5352 ± 0.00001 b = 5.4292 ± 0.00001 c = 7.7216 ± 0.00001

4.3 Elemental Analysis

To further validate the compositional integrity and chemical homogeneity of the multicomponent RE(Sc/Cr/Fe/Ni/Al)O_3 system, a combination of energy-dispersive X-ray spectroscopy (EDS) intensity profiling and mapping was employed. Figure 4.2(a) presents the characteristic X-ray intensity as a function of energy for the representative 11-cation perovskite, formulated as (La/Pr/Nd/Sm/Eu/Gd) (Sc/Cr/Fe/Ni/Al)O_3. The spectrum exhibits distinct peaks corresponding to all expected constituent elements, thereby confirming the successful incorporation of the targeted cations into the perovskite lattice. In parallel, Figure 4.2(b) provides spatially resolved EDS elemental maps for the same sample. The distribution maps of each rare-earth and transition-metal cations demonstrate a remarkably uniform contrast throughout the scanned region, with no evidence of clustering, segregation, or elemental gradients.

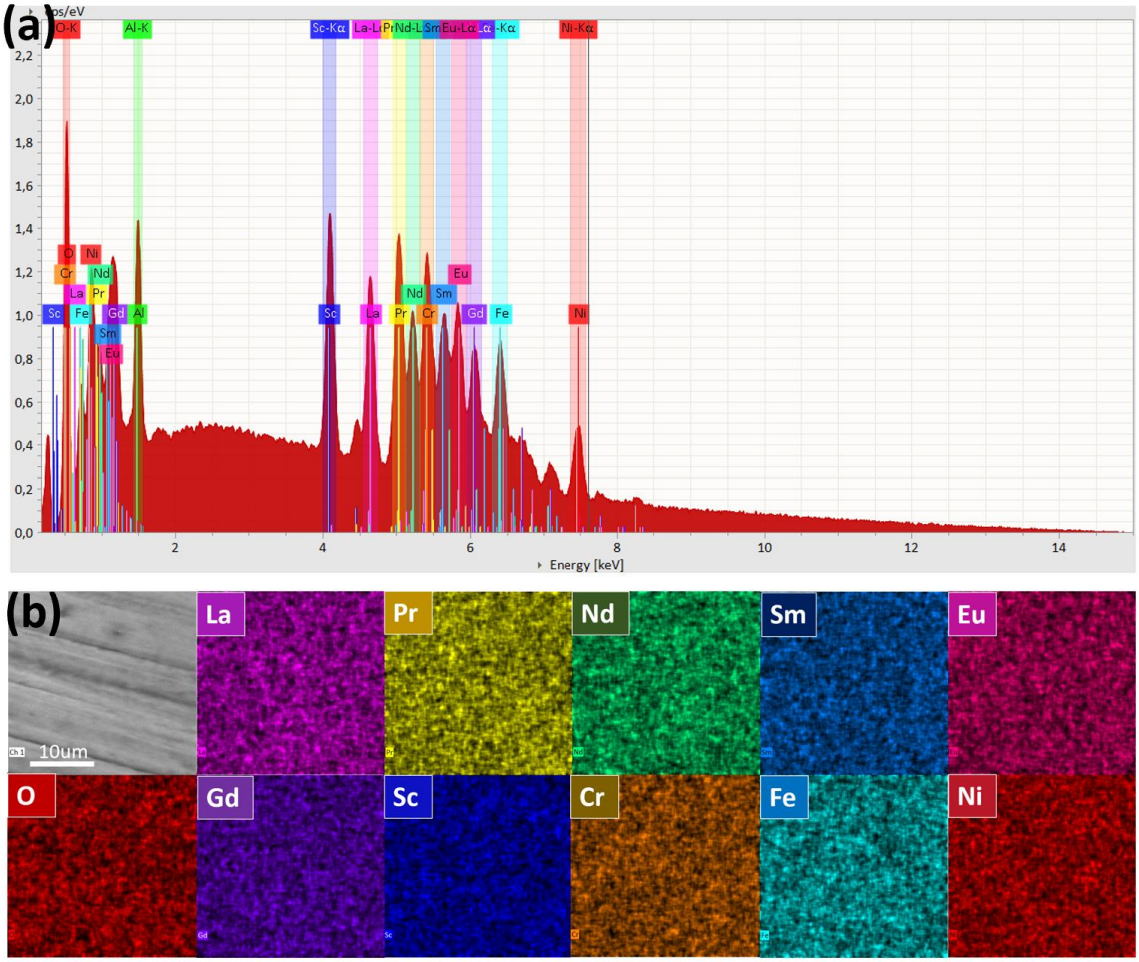

Figure 4.2: (a) X-ray intensity profile as a function of energy for the 11-cation perovskite (La/Pr/Nd/Sm/Eu/Gd)(Sc/Cr/Fe/Ni/Al)O_3, confirming the presence of all targeted constituent elements. (b) Corresponding surface energy-dispersive spectroscopy (EDS) elemental maps, illustrating a uniform spatial distribution of both rare-earth and transition-metal cations across the microstructure, with no evidence of phase segregation or compositional clustering.

4.4 Electrical Transport Properties

The temperature-dependent electrical conductivity of the rare-earth high-entropy perovskites is presented in Figure 4.3 over the range of 120-300 K. The conductivity exhibits a thermally activated increase, displaying an exponential temperature-dependence. When represented on a log scale, the data follow an essentially linear trend – consistent with the transport characteristics of elemental semiconductors. A systematic change in conductivity is observed across the series of rare-earth cations. Specifically, the conductivity at room temperature is found to be 0.008 (±0.0005), 0.006 (±0.0005), 0.0031 (±0.0002), and 0.0003 (±0.00002) S/cm for the Pr-, Nd-, Sm-, and Gd-based compounds, respectively. The monotonic decrease in conductivity with decreasing A-site ionic radius highlights the role of symmetry lowering induced by the lanthanide contraction, which in turn modulates the electronic transport pathways. These values are consistent with previous reports on high-entropy perovskites containing alternative B-site cations, such as Mn- and Co-based systems [9, 22].

To elucidate the conduction mechanism, the intrinsic temperature region was fitted to the small-polaron hopping model, expressed by the Arrhenius-type relation:

$$\sigma(T) = \sigma_0 \exp\left(-\frac{E_a}{k_B T}\right) \tag{4.1}$$

where σ_0 is the pre-exponential factor, E_a the activation energy, and k_B the Boltzmann constant. The extracted activation energies E_a span a narrow range of 0.16–0.168 eV. This narrow variation suggests that substitution of different rare-earth cations at the A-site, while keeping the B-site fixed, has only a modest influence on the fundamental electronic band structure. These findings are in excellent agreement with earlier investigations [23, 24], which reported negligible variation in activation energy with A-site modification.

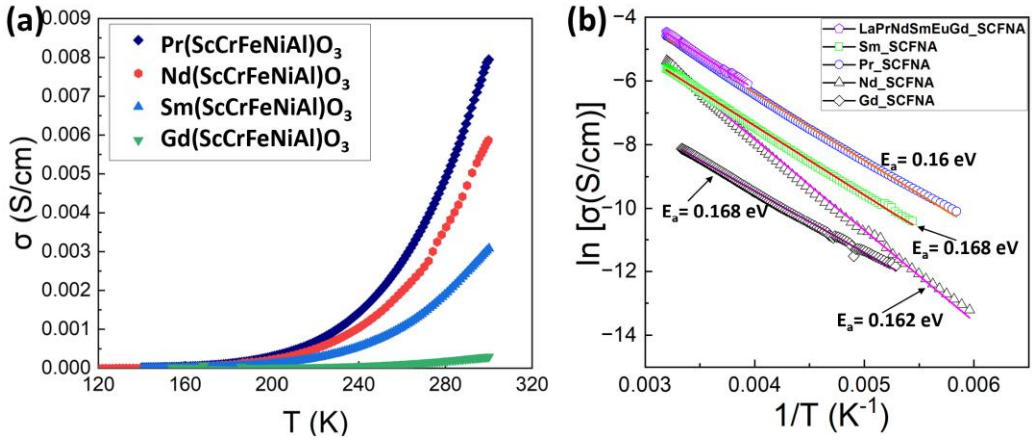

Figure 4.3: (a) Temperature dependence of electrical conductivity for RE(Sc/Cr/Fe/Ni/Al)O₃ (RE = Pr, Nd, Sm, Gd), illustrating the exponential increase in conductivity with rising temperature. (b) Corresponding Arrhenius representation, where the logarithm of conductivity is plotted against reciprocal temperature (1/T), confirming thermally activated transport behavior within the intrinsic conduction regime.

4.5 Magnetic Properties

Figures 4.4 (a)-(d) present the temperature dependence of the magnetic moment (measured at $\mu_0 H$ = 0.1 T) for LaSCFNA, PrSCFNA, SmSCFNA, and the 11-cation perovskite. All compositions exhibit a clear divergence between zero-field-cooled (ZFC) and field-cooled (FC) magnetization curves, indicative of magnetic frustration or canted ordering. The characteristic temperatures corresponding to the onset of this bifurcation – designated here as the magnetic ordering temperature, T_{mo} - are 20.8 K (PrSCFNA), 18.3 K (SmSCFNA), and 16.8 K (LaSCFNA). Notably, the FC magnetization shows a pronounced upturn below T_{mo}, whereas the ZFC response remains nearly constant or decreases, suggesting that only a subset of magnetic moments contribute to the emergent low-temperature order. This behavior may point toward a long range canted antiferromagnetic order from Cr-ions [4] and will be discussed elaborately in the next chapter. Importantly, none of the investigated compounds exhibit long-range ordering above 150 K, a marked departure from single-cation orthorhombic perovskites (e.g., $LaCrO_3$, $LaNiO_3$, $LaFeO_3$), which display robust ferro- or antiferromagnetic transitions associated with fully ordered B-site sublattices [25-28]. The suppression of high-temperature ordering in these configurationally complex compositions is likely attributable to entropy-driven chemical disorder, dilution of magnetic species, disrupted exchange connectivity, and the presence of competing interactions that collectively inhibit the formation of a single, coherent magnetic ground state [22, 29].

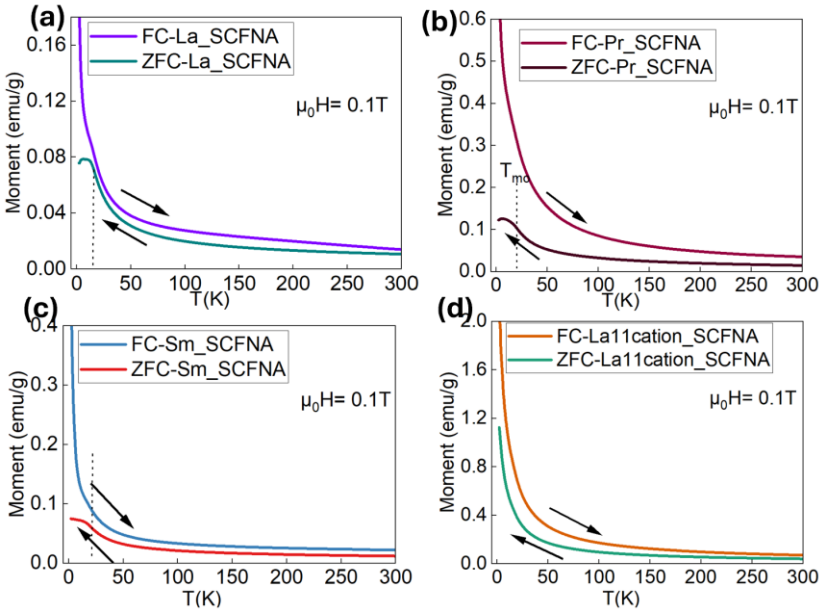

Figure 4.4: Temperature dependence of the DC magnetic moment measured at $\mu_0 H$ = 0.1 T for (a) $La(Sc/Cr/Fe/Ni/Al)O_3$, (b) $Pr(Sc/Cr/Fe/Ni/Al)O_3$, (c) $Sm(Sc/Cr/Fe/Ni/Al)O_3$, and (d) the 11-cation perovskite $(La/Pr/Nd/Sm/Eu/Gd)(Sc/Cr/Fe/Ni/Al)O_3$. Field-cooled (FC) measurements were recorded upon cooling, whereas zero-field-cooled (ZFC) measurements were collected during subsequent warming.

Figure 4.5 (a) highlights the change of magnetization against applied field across the rare-earth series at 30 K and 2 K. Compositions such as SmSCFNA and PrSCFNA exhibit predominantly speromagnetic character, whereas NdSCFNA and the 11-cation perovskite display a transition toward asperomagnetism, ultimately approaching near-saturation in GdSCFNA [3, 30]. Despite these low-temperature signatures, all compositions retain paramagnetic behavior at 30 K, indicating the absence of long-range order at elevated temperatures. The temperature derivative of the magnetization provides a clearer view of the ordering phenomena, revealing well-defined transitions for SmSCFNA ($T_{mo} \approx 18.3$ K), PrSCFNA ($T_{mo} \approx 20.8$ K), and LaSCFNA ($T_{mo} \approx 16.7$ K). The similarity of these transition profiles suggests that the driving mechanism originates from exchange interactions among B-site cations. Since La^{3+} carries no intrinsic magnetic moment (J = 0), the observed transition in LaSCFNA must result from a single or cooperative interactions among Ni^{3+}, Cr^{3+}, and Fe^{3+} species on the B-sublattice. Interestingly, none of the corresponding single-cation perovskites ($LaNiO_3$, $LaCrO_3$, $LaFeO_3$) display magnetic ordering at such low temperatures [26, 27, 31], implying that the emergent order likely arises from superexchange interactions involving mixed B-site cation pairs or triplets. A second, weaker anomaly is observed near 3.4 K, suggestive of a short-range magnetic contribution even though no distinct anomaly is visible in the M-T curves. As illustrated in Figure 4.5(b), the ordering temperature systematically increases with the A-site magnetic moment ($g_J \cdot J$), but disappears beyond Nd^{3+}, revealing a clear moment-dependent tunability of the low-temperature transition.

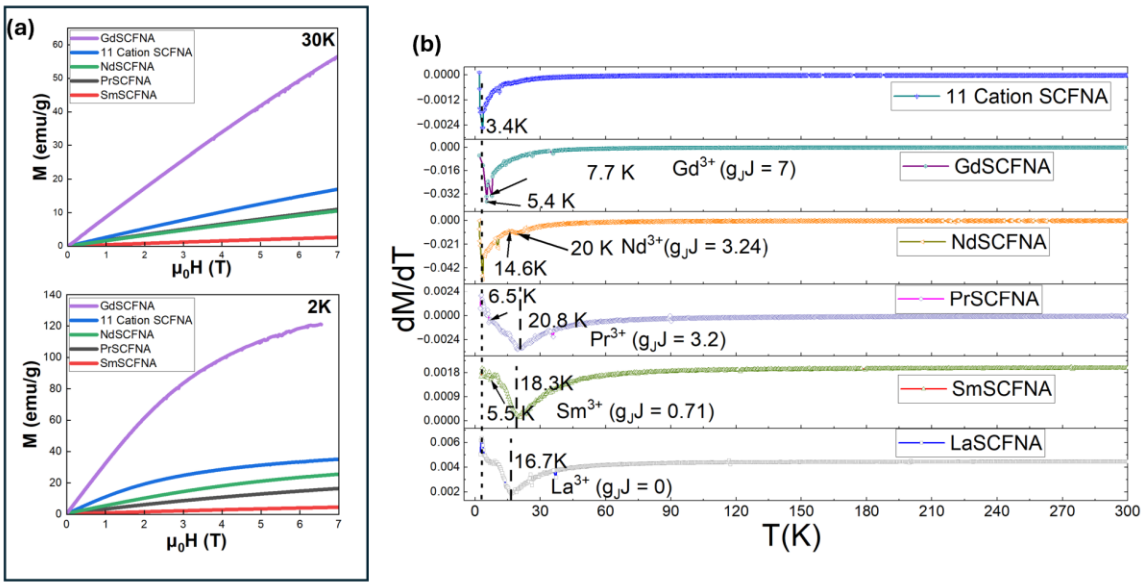

Figure 4.5: (a) Field-dependent magnetization measured up to 7 T at 30 K and 2 K, highlighting the low-temperature magnetic response. (b) Temperature derivative of the magnetization, illustrating the magnetic ordering transitions.

4.6 Thermodynamic Properties

Zero-field heat capacity (C_p) measurements were performed to understand the nature of the magnetic ordering transitions. As shown in Figure 4.6, no sharp λ-anomaly is observed at the magnetic ordering temperature (T_{mo}); instead, C_p/T versus T reveals a broad feature near ~20.8 K for PrSCFNA and ~18.3 K for SmSCFNA. The derivative dC_p/dT provides additional insight: PrSCFNA exhibits a cusp at 6.7 K, whereas SmSCFNA displays a distinct dip at 4.8 K, coinciding with a C_p peak. These signatures resemble previously reported spin-reorientation and magnetization-reversal phenomena in $PrFeO_3$ (~6.5 K) and $SmFeO_3$ (<5 K), respectively [32, 33]. The low-temperature data were quantitatively analyzed using,

$$C_p = \gamma T + \beta T^3 + \delta T^{3/2} \tag{4.2}$$

where γ represents the electronic contribution, β the lattice (phonon) term, and δ the magnetic contribution [34, 35]. Best-fit parameters yield γ = 0.46 J·mol^{-1}·K^{-2} (PrSCFNA) and 0.086 J·mol^{-1}·K^{-2} (SmSCFNA), indicating a significantly larger electronic density of states at the Fermi level for PrSCFNA, consistent with theoretical predictions. The phononic coefficient β was determined as 1.1746 × 10^{-4} J·mol^{-1}·K^{-4} (PrSCFNA) and 9.7658 × 10^{-5} J·mol^{-1}·K^{-4} (SmSCFNA), corresponding to Debye temperatures (θ_D) of 255 K and 271 K, respectively. These relatively low θ_D values imply strong phonon scattering and reduced lattice thermal conductivity. Finally, δ was extracted as 0.1393 and 0.01478 J·mol^{-1}·K$^{-3/2}$ for PrSCFNA and SmSCFNA, respectively, capturing the low-temperature magnetic excitations. The pronounced B-site cation-size variance (Sc^{3+}: 0.885 Å to Al^{3+}: 0.675 Å) was deliberately introduced to enhance configurational disorder, thereby amplifying phonon scattering and suppressing thermal transport [36].

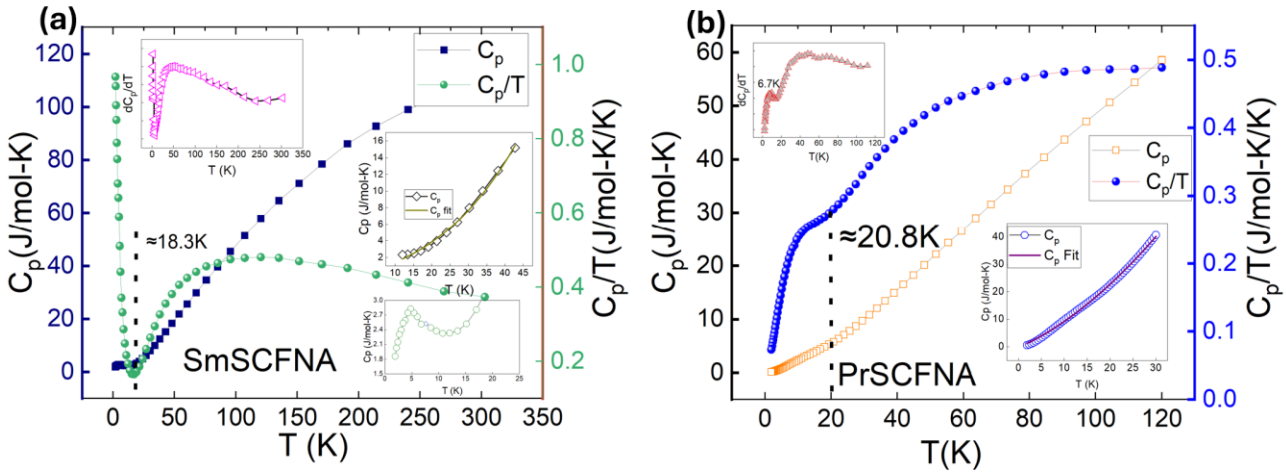

Figure 4.6: Temperature dependence of heat capacity (C_p) and normalized heat capacity (C_p/T) for (a) SmSCFNA and (b) PrSCFNA. Insets display dC_p/dT as a function of temperature along with the fitted curves to the low-temperature C_p data.

4.7 Elastic Properties

Resonant Ultrasound Spectroscopy (RUS) was used to obtain the full set of elastic constants for the RESCFNA perovskite series. As summarized in Figure 4.7, the longitudinal elastic constant c_{11} ranges from 87 GPa to 214 GPa, with the highest value observed for 11-cation perovskite, indicative of enhanced lattice stiffness. The shear modulus c_{44} follows a similar trend, decreasing from 68 GPa for 11-cation sample to ~37 GPa for LaSCFNA. Noticeably, the elastic moduli values for Pr, Nd and Gd perovskites falls in a close numerical range unlike La, Sm, and Eu perovskites – these later ones possess comparatively lower moduli values. However, caution is needed when comparing the elastic moduli values of our samples, as several (especially La and Sm) have a density that's significantly less than the theoretical density. Interestingly, EuSCFNA possesses much lower elastic moduli values despite being close to theoretical density, indicating that this sample is elastically softer than its counterparts.

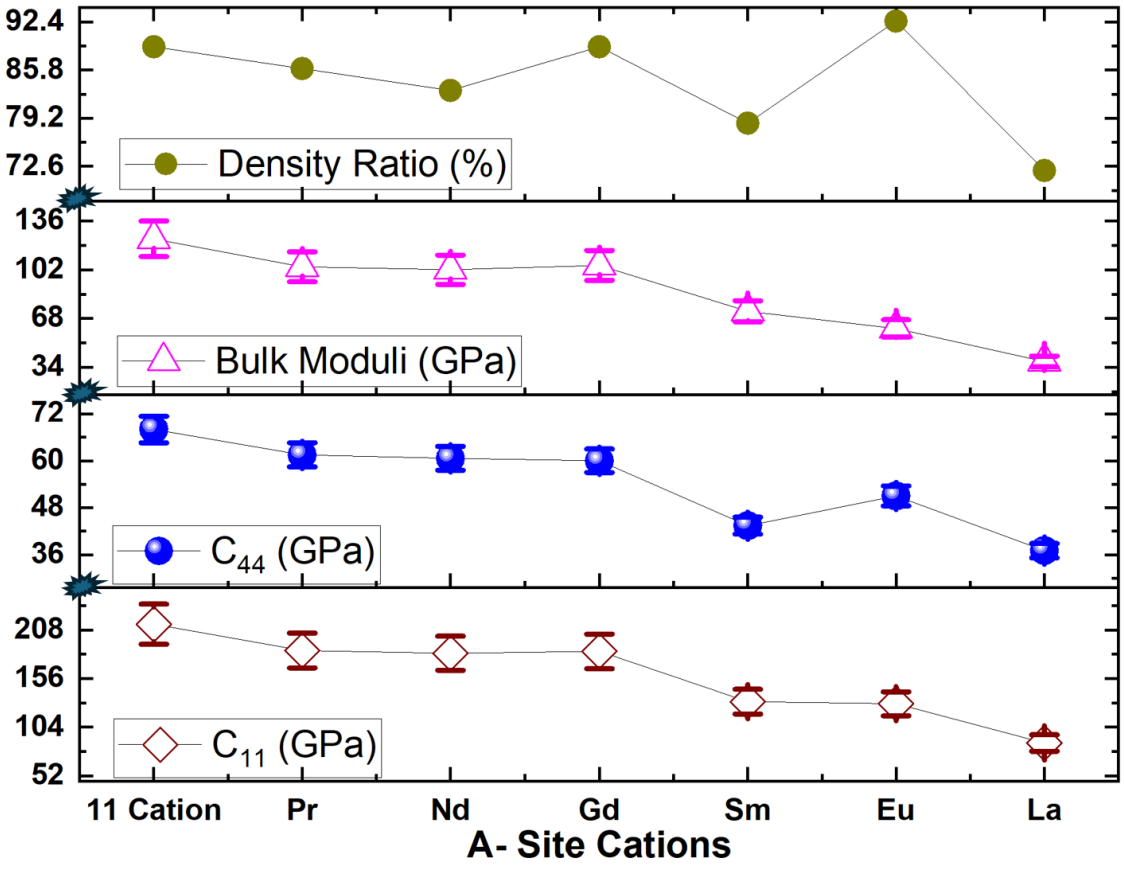

Figure 4.7: Elastic moduli values for the RESCFNA perovskites in consideration with sample density ratio (here the density ratio simply means the ratio of dimensional-experimental density divided by the theoretical density represented in percentage).

CHAPTER 5
STRUCTURE-PROPERTY CORRELATION IN MULTIFUNCTIONAL Eu(Sc/Cr/Fe/Ni/Al)O_3

5.1 Introduction

This chapter investigates the structure-property relationship and multifunctionality in Eu(Sc/Cr/Fe/Ni/Al)O_3 perovskite. Eu-perovskite was chosen because its half-filled $4f^7$ electronic configuration and the presence of intrinsic Eu^{2+} divalent states – which are known to facilitate charge trapping, promote polaron formation, and influence magnetization. Portions of this work are derived from a manuscript currently in preparation, titled "*Probing the Structure–Property Interplay in High-Entropy Perovskite Eu(Sc/Cr/Fe/Ni/Al)O_3 with Multifunctional Characteristics* by Rubayet Tanveer, Shirin Mozaffari, Dylan Windsor, Cale Overstreet, Tatenda Kanyowa, Katharine Page, Haidong Zhou, Bin Hu, Maik Lang, Haixuan Xu, David Mandrus, Veerle Keppens, and William J. Weber."

5.2 Local Bonding Environment in Eu(Sc/Cr/Fe/Ni/Al)O_3

Figure 5.1 presents the room-temperature synchrotron X-ray pair distribution functions (PDFs) of Eu(Sc/Cr/Fe/Ni/Al)O_3, analyzed using small-box fitting of relaxed SQS and averaged *Pnma* structures to resolve its local high-entropy structure. These structural insights are complemented by Raman spectroscopy, which confirms the presence of orthoferrite- and orthochromite-type vibrational modes. The average crystallographic structure of this EuSCFNA perovskite at room temperature, determined via X-ray diffraction (XRD), has been reported in detail in the previous chapter. To investigate the local structure, two distinct models were employed in the PDF refinements: (i) an orthorhombic *Pnma* model with averaged B-site occupancy and (ii) a disordered, relaxed special quasi-random structure (SQS). Interestingly, the average *Pnma* model struggles to emulate the Eu-O bond length distribution precisely, unlike, the SQS model which reproduces a sharp Eu-O peak apparently simulating the data. This can be due to relaxations of the SQS model that pull part of the Eu-O shell to shorter r (Å), cleanly separating it from the first O-O peak. On the other hand, the average *Pnma* model, by construction, locks O into an average position, pushing Eu-O to overlap with O-O and producing the broad, blended peak. Notably, both models exhibit comparable agreement with the experimental data – by producing similar bond distribution results. In the low r-region beginning at ~2.4 Å, the PDFs reveal that the first three peaks correspond to Eu–O, Eu–B (B-site cations), and Eu–Eu coordination. The peak at ~2.48 Å represents the Eu–O nearest-neighbor distance for the Eu atom, while the second and third peaks at ~3.30 Å and ~3.90 Å correspond to the Eu–B and Eu–Eu correlation distances. These bond lengths are consistent with values reported in previous studies [37, 38]. Figures 5.1(c) and 5.1(d) display the partial PDFs for Eu–B and O–B atomic pairs obtained from SQS-based fits. Peak positions systematically shift to larger distances with increasing B-site ionic radius, with Sc – the largest B-site cation – exhibiting the longest Eu–Sc and Sc–O bonds. Interestingly, Ni and Cr deviate significantly from this trend. Eu–Ni correlations are unexpectedly short, whereas Ni–O bonds are among the longest, while Cr–O bonds are the shortest of all B-site cations without a proportional reduction in Eu–Cr distances. This anomalous bonding behavior persists across

multiple randomized, relaxed configurations (Fig. 5.2), confirming that it is intrinsic to the disordered lattice. Figure 5.1(e) shows bond valence sums (BVS) derived from PDF-refined bond lengths. Sc, Fe, and Al yield BVS values consistent with their nominal +3 oxidation states, while Ni exhibits a valence near +2, consistent with Ni^{2+}, and Cr a higher value of ~3.6, suggesting mixed Cr^{3+}/Cr^{4+} valence with a dominant Cr^{4+} population. These results, together with local Eu–Ni/Cr and O–Ni/Cr environments, suggest enhanced electrostatic attraction between Eu^{3+} and Ni^{2+}, leading to Eu–Ni bond contraction, potential small-polaron formation, and a possible charge-glass or cooperative charge-disproportionation mechanism [36, 39-44].

Figure 5.1(f) presents the Raman spectrum of EuSCFNA at room temperature, revealing Eu^{3+} translational modes (<200 cm^{-1}), BO_6 octahedral tilts (250–400 cm^{-1}), bending (~470 cm^{-1}), anti-stretching (~550 cm^{-1}), and breathing/stretching (~650 cm^{-1}). These assignments match reported orthoferrite/orthochromite modes, confirming a Pnma lattice with subtle local distortions induced by high-entropy cation distribution [45-47].

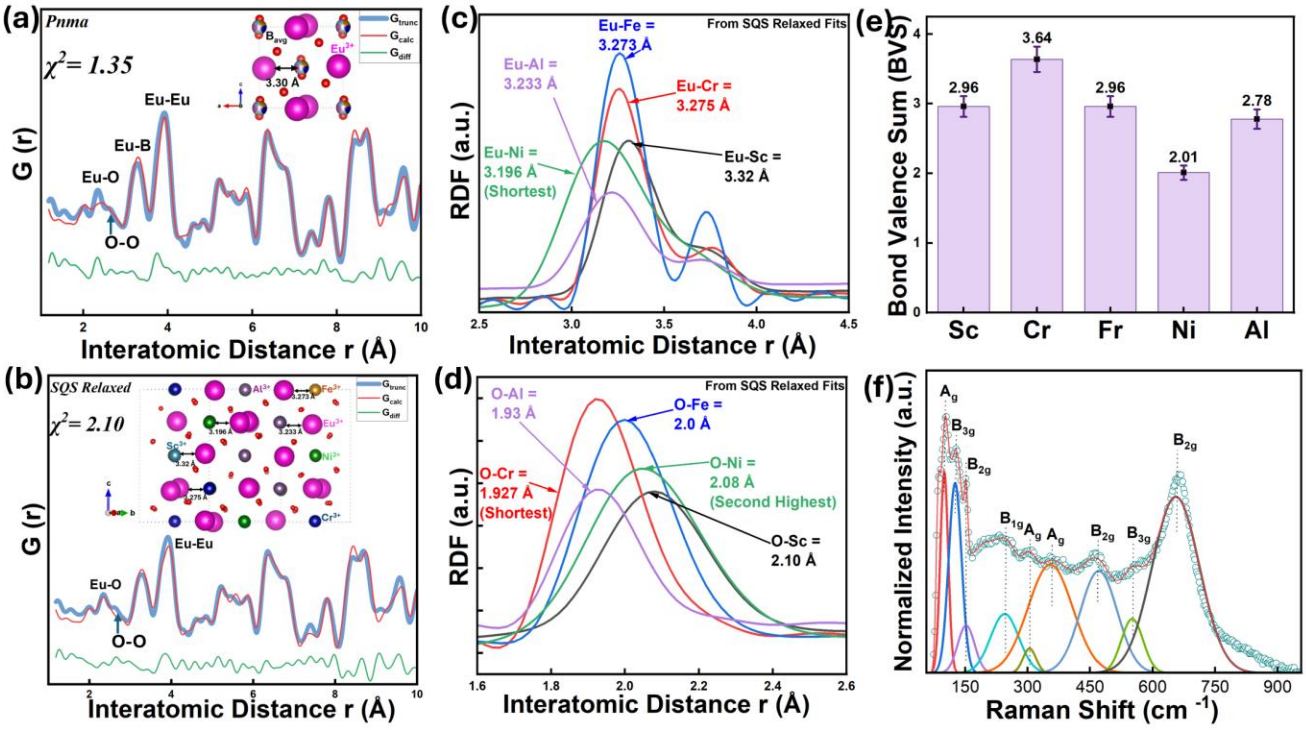

Figure 5.1: Local structural characterization of Eu(Sc/Cr/Fe/Ni/Al)O_3 perovskite. (a) Total PDF refined using the Pnma average structure, (b) total PDF refined with a relaxed SQS model, (c) partial PDFs for Eu–B bonds, and (d) partial PDFs for O–B bonds highlighting anomalous Ni bond-length distributions, (e) bond valence sum (BVS) analysis of B-site cations, and (f) deconvoluted room-temperature Raman spectrum (473 nm excitation) confirming orthoferrite/orthochromite vibrational modes.

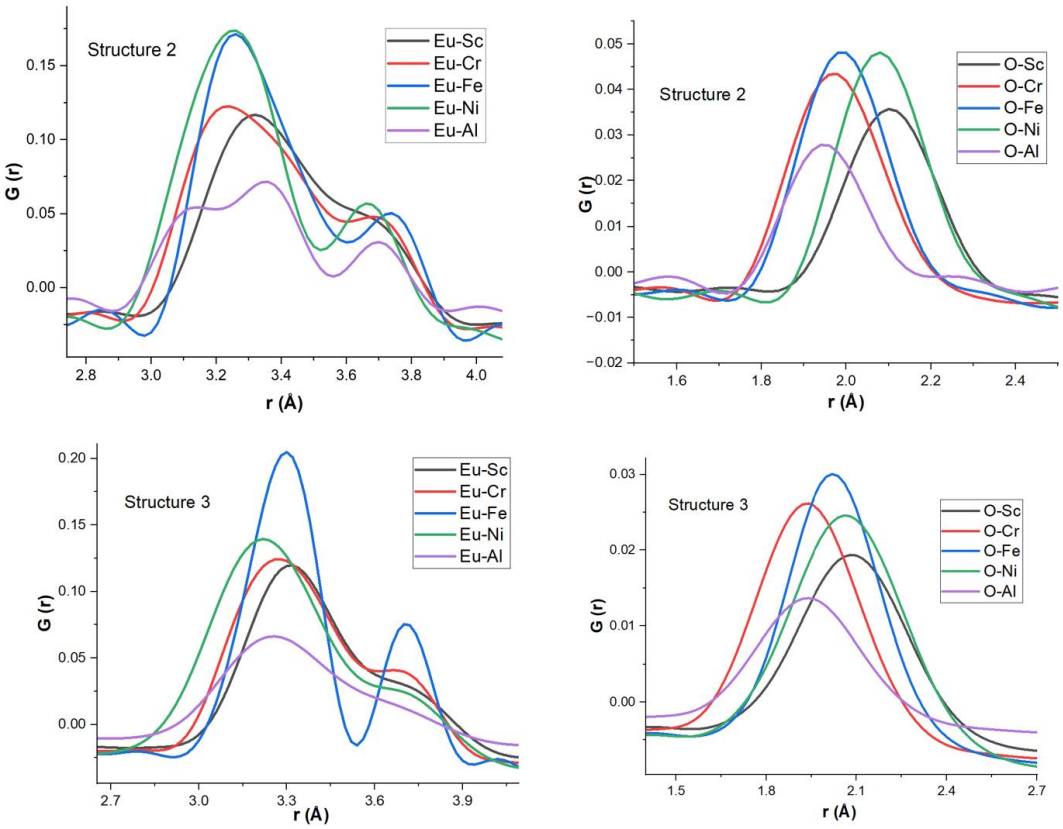

Figure 5.2: Eu–B and O–B bond length distributions across various relaxed structural models, showing a consistent relative trend in bond distances.

5.3 Temperature Dependent XRD Analysis

Figure 5.3 provides a detailed temperature-dependent X-ray diffraction (XRD) analysis of Eu(Sc/Cr/Fe/Ni/Al)O_3 across a broad temperature range, from room temperature down to 10 K. The diffraction patterns confirm that the perovskite preserves its orthorhombic symmetry ($a \neq b \neq c$; $\alpha = \beta = \gamma = 90°$) over the entire temperature interval, consistent with the Pnma space group. Figure 5.3(a) highlights the evolution of the (121) reflection as a function of temperature, where an intriguing intensity anomaly is observed. At higher temperatures, the peak intensity is relatively strong, gradually decreases upon cooling to ~90 K, and subsequently begins to rise again. The change is not smooth but displays abrupt intensity drops at specific temperatures – most notably between 250–240 K and again between 100–90 K – hinting at incipient structural transitions within these regions.

Figure 5.3(b) examines the temperature-dependent broadening of the (240)/(321) reflections (top panel) and the corresponding variation of the XRD-derived density (bottom panel) between 290 K and 10 K (see Figure 5.4 for magnified view). The reflections remain sharp and resolution-limited above ~140 K, but progressively broaden below this temperature, signifying the onset of local structural disorder or subtle symmetry lowering. The XRD-derived density exhibits a parallel temperature evolution, with distinct slope changes near 260 K, 140 K, and 90 K. Together, these

observations suggest a strong coupling between structural and electronic degrees of freedom in this perovskite system.

The temperature evolution of the unit cell volume and lattice parameters (a, b, c), shown in Figure 5.3(c), reveals a gradual thermal contraction punctuated by a sharp discontinuity between 150 K and 130 K. Above 140 K, lattice parameters a and b show pronounced decreases, whereas c remains nearly constant or slightly expands, consistent with anisotropic thermal contraction. Below 140 K, the difference between a and c becomes nearly constant, suggesting a stabilization of the structural distortion. These changes correlate with the peak broadening trends seen in Fig. 5.3(b), which extend throughout the 10–140 K range, reinforcing the notion of a thermally driven structural evolution.

The sharp anomaly at 140 K likely marks the onset of charge ordering or charge disproportionation phenomena, and the more subtle anomalies near 260 K and 90 K support the existence of multiple temperature-dependent structural rearrangements. Importantly, these structural observations are corroborated by electrical resistivity measurements discussed later, which show corresponding features at these temperatures.

The anomalous low-temperature behavior of lattice parameters, coupled with diffraction peak broadening and intensity suppression, has been previously interpreted through two plausible structural scenarios [48, 49]. One scenario suggests a continuous distribution of lattice parameters, wherein multiple local maxima evolve dynamically with decreasing temperature, causing shifts in their positions and intensities – consistent with a gradual reorganization of the lattice on cooling. The alternative interpretation involves the coexistence of discrete structural domains or phases, each possessing a coherence length that exceeds the intrinsic coherence length of the probing X-rays. In this case, the diffraction peak broadening would result from varying relative phase fractions as the temperature changes.

These findings are consistent with the anomalous Ni and Cr radial distributions observed in Figures 5.1(c–d), particularly below 140 K, which may indicate the emergence of disproportionated Ni^{2+}, Cr^{3+}, and Cr^{4+} sublattices. This scenario aligns with literature reports on charge-order-driven structural transitions in related nickelate, chromate, and manganate perovskites, where charge disproportionation typically drives a lowering of symmetry from Pnma to at least $P2_1/n$ [48-51]. However, given that Ni and Cr together constitute less than 40% of the total B-site occupancy in this high-entropy perovskite, the transition is likely more subtle, possibly second-order in nature, rather than a fully cooperative first-order transition.

Overall, the combined temperature-dependent diffraction and lattice parameter data indicate that $Eu(Sc/Cr/Fe/Ni/Al)O_3$ undergoes a series of subtle structural rearrangements upon cooling, with the most pronounced event occurring near 140 K. This transition likely reflects the onset of charge localization or ordering phenomena, which couple strongly to lattice distortions. Further neutron diffraction studies on this and related rare-earth high-entropy perovskites will be crucial for fully elucidating the microscopic origin of these temperature-driven transitions and distinguishing between continuous lattice parameter distributions and phase-coexistence models.

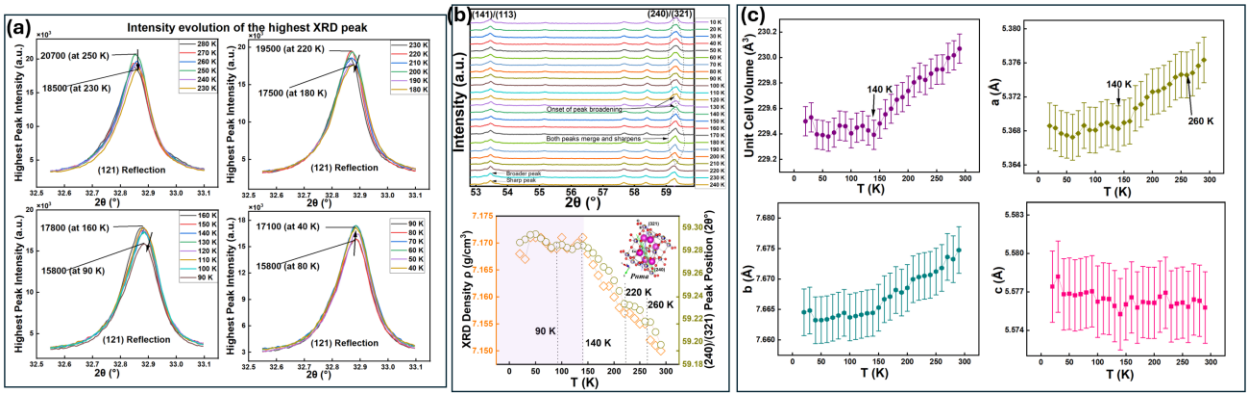

Figure 5.3 : Temperature-dependent evolution of X-ray diffraction (XRD) patterns: (a) anomalous intensity variation of the dominant (121) reflection, (b) 2θ region from 53°–60° across 240–10 K (top) with corresponding XRD-derived density and Gaussian-fitted (240)/(321) peak positions as a function of temperature (bottom), and (c) unit cell volume and lattice parameters showing a distinct discontinuity near 140 K.

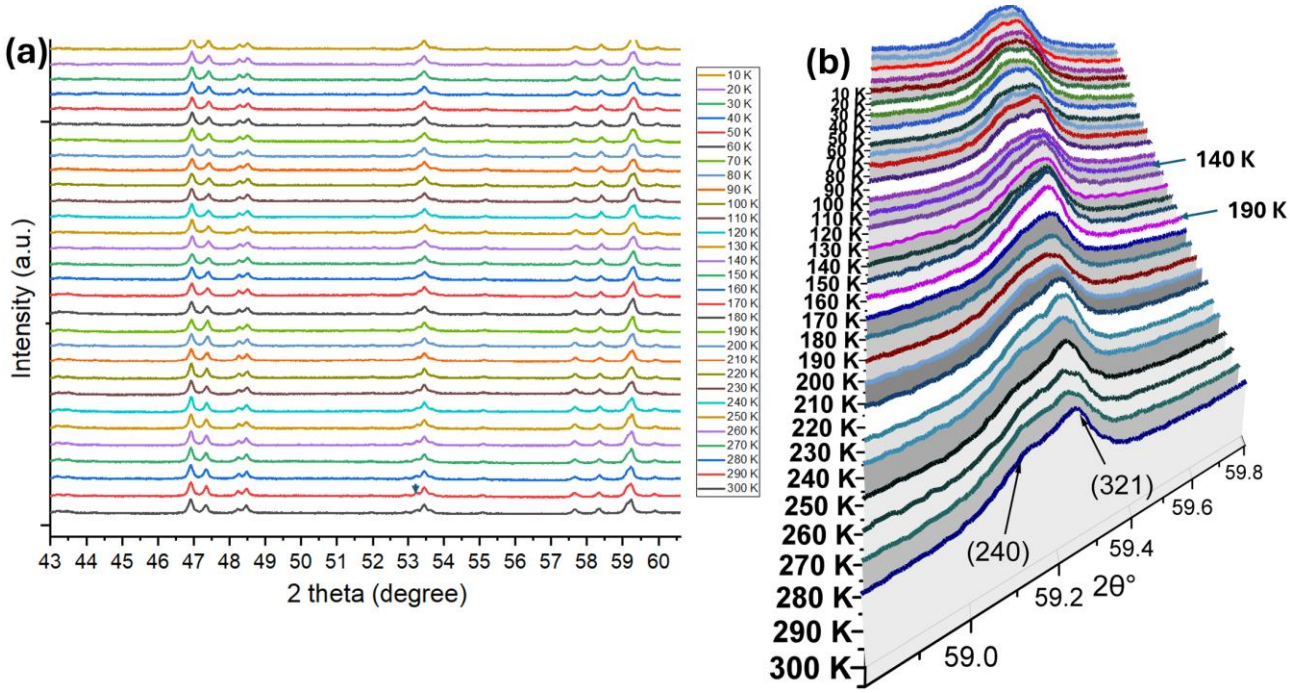

Figure 5.4: Illustration of the temperature-driven evolution of selected XRD peaks, highlighting variations in peak intensity, position, sharpening and widening across the measured temperature range.

5.4 AC Impedance Analysis

Figure 5.5 (a) displays the temperature dependence of the electrical resistivity of Eu(Sc/Cr/Fe/Ni/Al)O_3 measured between 350 K and 100 K using a two-probe high-resistance AC configuration. A sharp rise in the resistivity trend is observed around ~140 K. The material exhibits insulating behavior, and below ~100 K the resistivity increases beyond the measurable range of the high-resistance setup, precluding reliable quantification of resistivity values in this low-temperature regime. Figure 5.5 (b) presents the resistivity in natural log scale for activation energy analysis. The temperature-dependent expression for small polaron resistivity can generally be formulated based on the following equation [52-55],

$$\rho(T) = \rho_0 T \exp\left(\frac{E_a}{k_B T}\right) \tag{5.1}$$

where ρ_0 is a material-dependent constant and a function of charge carrier density, k_B is the Boltzmann constant, and E_a is the activation energy. Here, $ln\ (\frac{\rho}{T})$ vs. $1/T$ should yield a linear region with a slope proportional to E_a. Although the resistivity data were analyzed using multiple conduction models, including Efros–Shklovskii and Mott variable-range hopping (Fig. 5.6), no single linear regime spans the entire temperature range. Instead, distinct changes in slope are observed at approximately ~260 K and ~140 K, each corresponding to successive reductions in activation-energy. Notably, all examined models capture this behavior consistently, yielding comparable activation energy values within the individual temperature regimes. These characteristic inflection points are further corroborated by pronounced features in the AC phase-angle versus temperature response shown in Fig. 5.5 (c). A reproducible peak at approximately 260 K (see Fig. 5.7 b and 5.7 e) likely signifies the emergence of additional lattice polarons, consistent with the local distortions inferred from the PDF analysis. In contrast, the sharp increase in phase angle observed near 140 K suggests a transition from purely resistive (ohmic) behavior to a non-ohmic capacitive or inductive response. This latter feature is consistently reproduced across multiple measurements and appears to correlate with the structural changes identified by the XRD analysis (see Fig. 5.7 a–c).

The correlation between electrical and structural changes – evidenced by a decrease in activation energy below ~260 K – suggests formation of new polarons and the involvement of optical phonon-assisted hopping mechanisms [56, 57]. Notably, the Debye temperature extracted from low-temperature heat-capacity fitting is approximately 225 K, which coincides with the temperature range in which several anomalous structural features were identified (Fig. 5.7 a). In the previous chapter, we elucidated that electrical conductivity within these rare-earth RSCFNA (R = rare-earth ions) perovskite systems at room temperatures can primarily be attributed to the Ni^{3+}-ions (also see Fig. 5.7 d). This conclusion is supported by the fact that the single-component perovskites $RCrO_3$ and $RFeO_3$, with significantly larger band gaps at room temperature, exhibit insulating behavior. Furthermore, our photoluminescence studies (discussed later) confirm the presence of a small concentration of Eu^{2+} ions as natural impurities in the investigated EuSCFNA perovskite.

In this material, the dominant charge carriers at elevated temperatures are presumed to be holes associated with Ni^{3+} species. These holes are not expected to bind to Eu^{3+}, as Eu remains predominantly in the trivalent state under ambient and moderately elevated temperatures. Rather,

donor–type defects – such as oxygen vacancies – can locally compensate Ni^{3+} ions, leading to their partial reduction to Ni^{2+}. In this context, hole transport likely proceeds via thermally activated hopping between adjacent Ni^{3+} and Ni^{2+} sites (i.e., small-polaron hopping). The associated charge-transfer process may be further influenced by the presence of local Eu^{3+}–Ni^{2+} electrostatic interactions, which can stabilize short Eu–Ni distances and facilitate repeated electron–hole exchange within the perovskite lattice [56].

In Eu(Sc/Cr/Fe/Ni/Al)O_3, a hole located on a Ni^{3+} site may hop to a neighboring Ni^{2+} site only if a new lattice distortion is created on that neighboring site. According to Holstein, the hopping rate is therefore thermally activated, and the resistivity follows [58, 59],

$$E_a = \frac{1}{2}\alpha\hbar\omega_0 - t \tag{5.2}$$

where t is the transfer integral between neighboring cation sites, $\hbar\omega_0$ is the optical phonon energy and the electron-phonon interaction α is given as,

$$\alpha = e^2\left(\frac{1}{\varepsilon_\infty} - \frac{1}{\varepsilon_0}\right)\sqrt{\frac{m}{2\omega_0}} \tag{5.3}$$

where m denotes the band-mass, and ε_0 and ε_∞ are the static and high-frequency dielectric constants. The above equations can be understood linking with Fig. 5.5 (c), where appearing features at ~260 K may indicate changes in the dielectric constant of the medium due to formation of small polarons – possibly linked with shorter Eu-Ni bond length observed with RDF analysis (Fig. 5.1c) – affecting the electron-phonon interaction term and thereby dropping the activation energy. Upon further cooling (≈140 K), abrupt changes in both the activation energy and the XRD-derived structural parameters indicate a transition toward a more localized hopping regime, likely driven by a cooperative charge disproportionation in which Ni^{3+} and Cr^{3+} cations reorganize into Ni^{2+} and Cr^{4+} valence states. This is consistent with the ground-state BVS analysis, which reveals only Ni^{2+} and mixed Cr^{3+}/Cr^{4+} species, despite the high-temperature transport data clearly requiring the presence of Ni^{3+}. Such behavior is characteristic of a crossover from a thermally activated small-polaron regime to a locally ordered state of reduced carrier mobility and bears strong resemblance to the "polaron-condensation" scenario reported in other correlated perovskite systems [60]. The reduction in activation energy E_a at lower temperatures, despite the expected strengthening of the electron–phonon coupling, can be explained by the contribution of the transfer integral $t = \langle\psi_i|\hat{H}|\psi_j\rangle$. Which quantifies the electronic overlap between neighboring lattice sites. A larger 't' corresponds to greater electronic overlap between adjacent transition-metal sites and thus reduces the energy barrier for polaron hopping. The continuous contraction of the XRD-derived unit cell volume down to ~140 K supports an enhancement of orbital overlap assumption, which increases 't' and counteracts the effect of stronger lattice coupling. Consequently, the apparent decrease in activation energy results from the interplay between an increasing transfer integral and the evolving electron–phonon coupling, both of which collectively govern the temperature dependence of the polaron hopping energy.

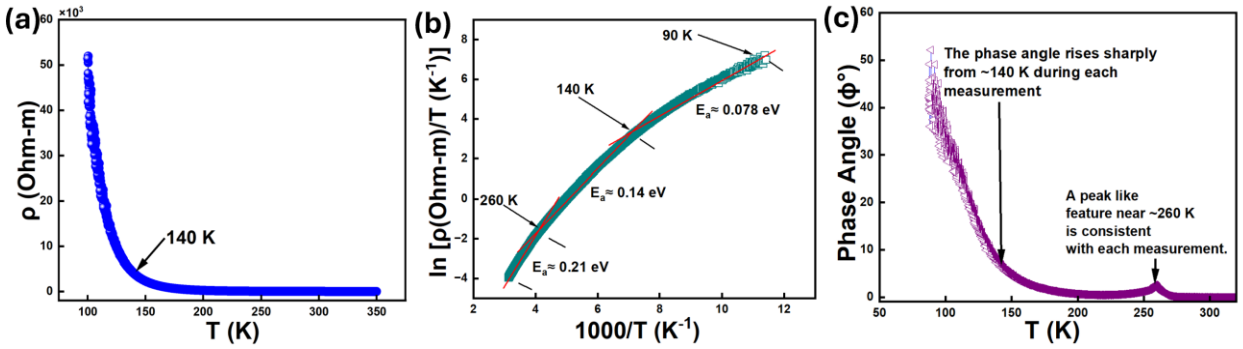

Figure 5.5: (a) Temperature-dependent electrical resistivity of Eu(Sc/Cr/Fe/Ni/Al)O_3 measured over the 100-350 K interval, illustrating the activated of charge transport behavior with temperature variation. (b) Plot of the natural logarithm (ln ρ/T) versus inverse temperature (1000/T), providing insight into the change in activation energy at different temperature regimes. (c) variations in the AC resistivity phase angle as a function of temperature.

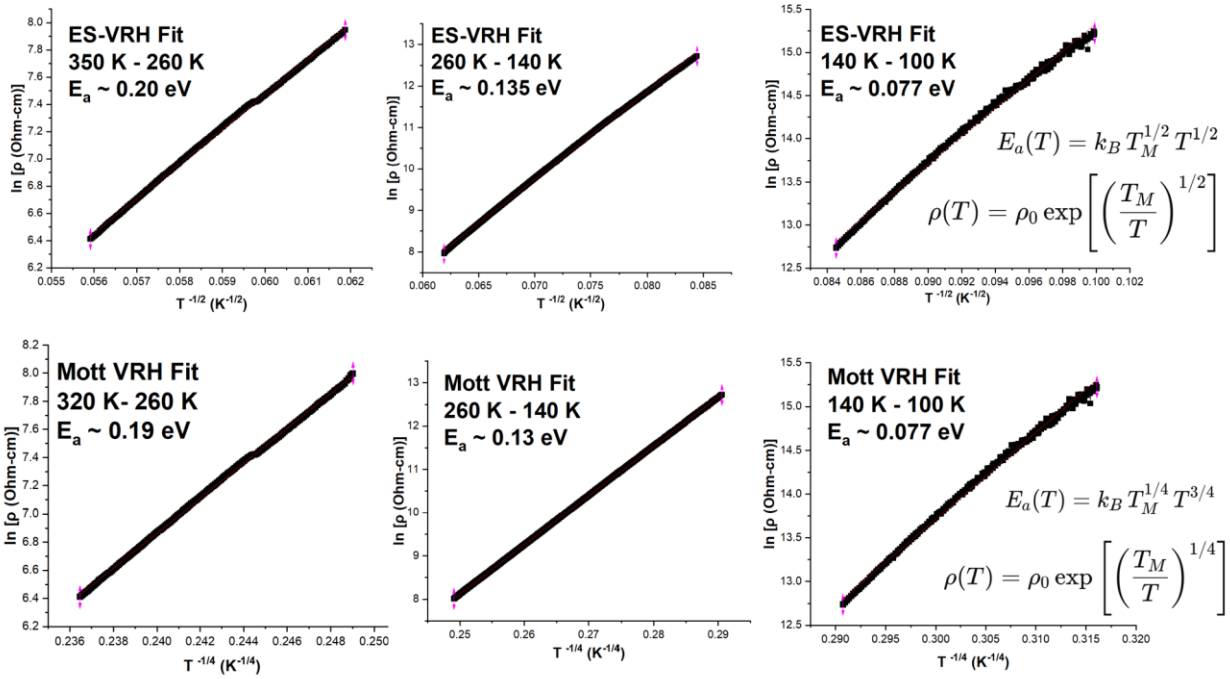

Figure 5.6: Various models demonstrating comparable activation energies and temperature-dependent behavior, aligning closely with the characteristic trends predicted by small-polaron hopping conduction mechanisms.

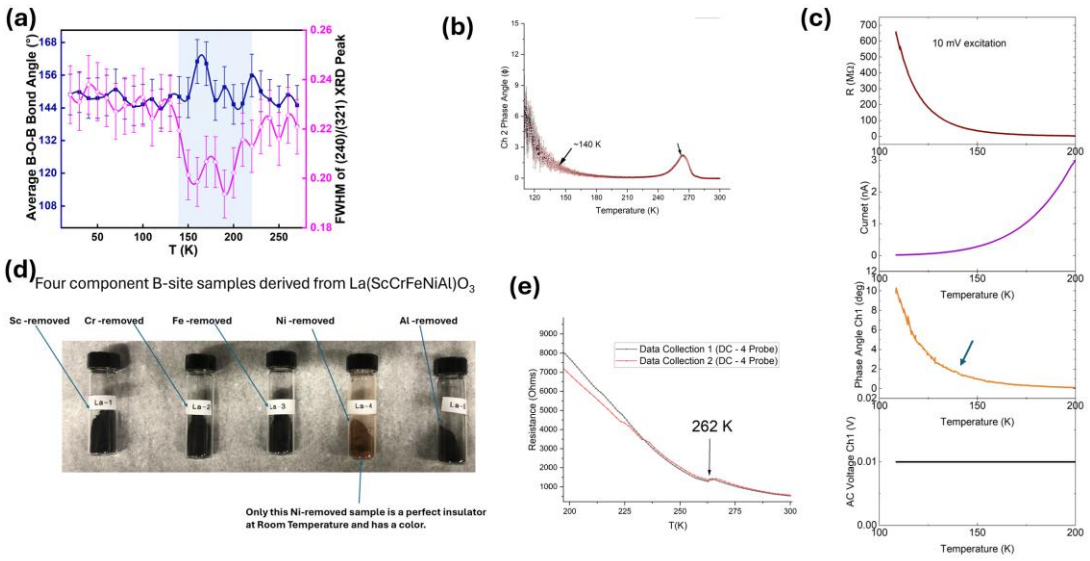

Figure 5.7: (a) The temperature trend of average B-O-B bond angle and Full Width Half Maxima (FWHM) of doubly degenerate (240) and (321) X-ray reflection exhibiting bond angle widening and peak broadening at the same region where activation energy drops. (b) and (c) Showing recurrent features at ~140 K and ~260 K with different measurements. (d) Showing four component B-site samples derived from the five component RE(Sc/Cr/Fe/Ni/Al)O_3 (RE= Rare Earth) parent at room temperature, where only the composition with Ni removed is a perfect insulator with a non-black color. This signifies that Ni is possibly the major contributor to conductivity and some Ni-ions may have a different oxidation state (possibly Ni^{3+}- which normally possesses lower temperature conductivity in octahedral oxide coordination) than its ground state (Ni^{2+}).

5.5 Magnetic and Thermodynamic Property Analysis

Figure 5.8 (a) shows that the EuSCFNA perovskite undergoes a long-range antiferromagnetic transition at approximately 17 K, marked by the bifurcation of the zero-field-cooled (ZFC) and field-cooled (FC) magnetization. In the previous chapter, we showed that this transition was observed for analogous rare-earth perovskites (R = La, Pr, Sm) with identical B-site compositions, and it was elucidated that the magnetic ordering originates from the B-site sublattice. The data presented in Figure 5.8 (b) confirm that the sample does not exhibit saturation even at temperatures as low as 2 K. While the divergence of ZFC and FC magnetization and an absence of a lambda anomaly in C_p vs T curve (Fig. 5.8 (d)) are often indicative of competing glassy dynamics or spin-freezing behavior, the AC susceptibility results shown in Figure 5.8 (c) provide a contrary conclusion. The absence of a frequency-dependent shift in the Néel temperature (TN) confirms a long-range antiferromagnetic order rather than spin-glass behavior.

The heat capacity measurements conducted under 0 T and 5 T magnetic fields between 2 K and 200 K, shown in Figure 5.8 (d), are nearly overlapping, except for a slight divergence in the intermediate temperature range near ~100 K to 140 K region. Figure 5.8 (e) elucidates this feature further through a derivative heat capacity versus temperature plot. Intriguingly, the derivative heat capacity curves for both 0 T and 5 T magnetic fields remain closely aligned above ~130 K but begin to diverge distinctly below this temperature. This bifurcation suggests an intriguing

correlation with magnetic ordering. In several rare-earth nickelates, such as $EuNiO_3$, $GdNiO_3$, and $DyNiO_3$, within their insulating regime, Ni ions form two distinct magnetic sublattices: Ni^{2+} exhibiting magnetic ordering and the other Ni^{4+} being non-magnetic. When these magnetic sublattices order, their signature is primarily detectable through heat capacity measurements, without leaving discernible imprints on magnetization-temperature (*M-T*) curves [39, 40, 49, 50, 61]. Therefore, the bifurcation observed in Figure 5.8 (e) is most plausibly attributed to the ordering of these disproportionated or charge ordered magnetic Ni^{2+} sublattices.

Another magnetic component occupying the *B*-site is *Fe*, and it is well-documented that most rare-earth ferrite perovskites (*$RFeO_3$*) typically exhibit a spin-switching or spin-reorientation behavior in their zero-field-cooled (*ZFC*) and field-cooled (*FC*) magnetization curves, rather than displaying distinct temperature-dependent magnetic orderings or saturation features in M/H measurements [32, 62]. Conversely, Cr-ions in rare-earth chromites in oxide octahedral environment, such as $EuCrO_3$, have been shown to adopt a G_x-type antiferromagnetic ordering. This arrangement is accompanied by a slight ferromagnetic canting along the c-axis, which manifests as a bifurcation in *ZFC* and *FC* magnetization curves – a phenomenon confirmed through neutron diffraction studies [4]. Hence, the bifurcation observed in the *ZFC* and *FC* curves in Fig. 5.8 (a) can most plausibly be attributed to the canted antiferromagnetic ordering of the Cr-ions in the B-site.

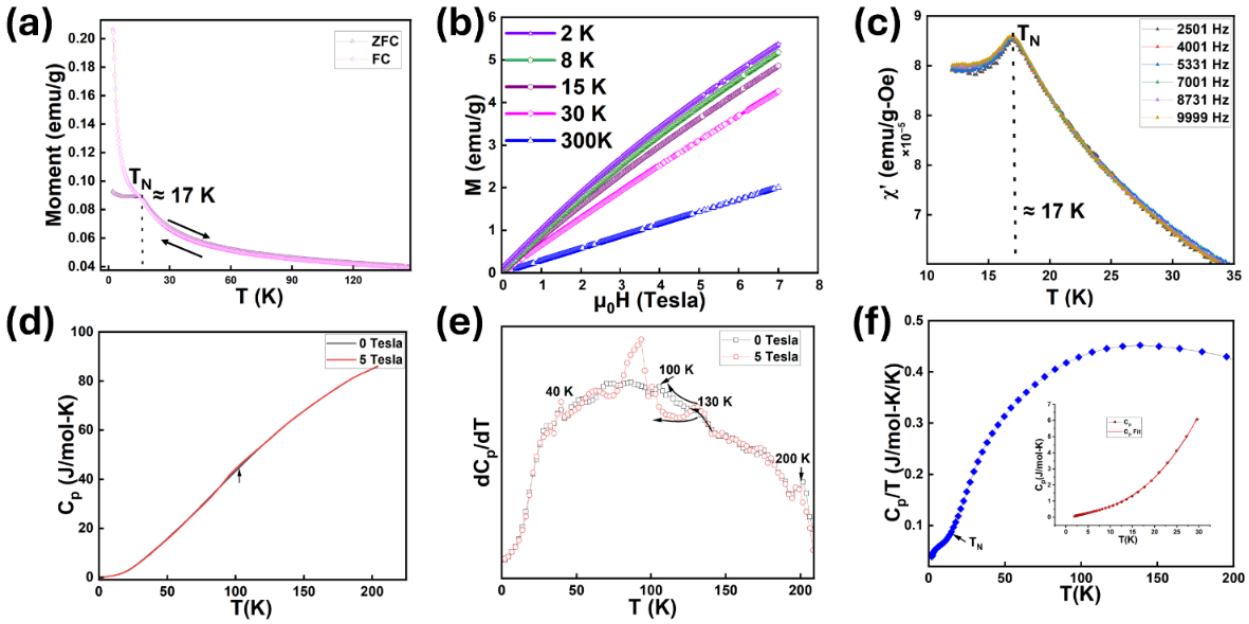

Figure 5.8: Magnetic and thermal behavior of the $Eu(Sc/Cr/Fe/Ni/Al)O_3$ perovskite. (a) The temperature dependence of zero-field-cooled (ZFC, warming) and field-cooled (FC, cooling) DC magnetic moment. (b) The M/H curves in temperature range from room temperature to 2 K. (c) The real part of the AC magnetic susceptibility (d) Heat capacity (C_p) measurements conducted from 2 K to 200 K under 0 T and 5 T magnetic fields (e) The derivative of heat capacity as a function of temperature (f) The C_p/T vs. temperature.

Nonetheless, future neutron diffraction investigations could obtain further insights into this magnetic behavior. The C_p/T vs T curve, however, exhibits a broad dip near the Néel Temperature, and the low-temperature heat capacity was fitted with the following equation [10],

$$C_{\mathrm{p}} = \gamma T + \beta T^3 + \delta T^{3/2} \tag{5.4}$$

From the fit, the lattice contribution was obtained as β = 1.695E-4 J/mol-K^4, and applying the relation $\beta = 234Nk_{\mathrm{B}}/\theta_{\mathrm{D}}^3$, (where N= no. of ions per mole, and k_{B}= Boltzmann Constant), the Debye Temperature was calculated as θ_{D} = 225 K.

5.6 Photoluminescence Property Analysis

Figure 5.9 presents the temperature-dependent photoluminescence (PL) emission spectra of *Eu(Sc/Cr/Fe/Ni/Al)O$_3$* under excitation at *343 nm*, accompanied by detailed deconvoluted analyses of peaks at 100 K and 295 K. Figure 5.9 (a) highlights two distinct emission features: a broad peak on the higher energy side, spanning approximately 2.0 eV to 3.4 eV, which is attributed to $4f^6 5d^1 \rightarrow 4f^7$ transitions characteristic of Eu^{2+} [63-65]. The second, sharper peak observed at ~1.93 eV, corresponds to the $^5D_0 \rightarrow {}^7F_3$ transitions of Eu^{3+} – signifying *J* mixing as forbidden by selection rule – may be the mixture of $^7F_2$ (hypersensitive to local crystal field by intensity changes) and $^7F_4$ transitions [66, 67]. The observation that most of the intensity bands in Fig. 5.9 are attributed to Eu^{2+} can be explained by the reduction of Eu^{3+} ions facilitated by the presence of oxygen vacancies within the system. This reduction process is likely initiated during the vacuum hot-pressing stage, where oxygen-deficient conditions promote the stabilization of Eu^{2+}. Furthermore, these oxygen vacancies appear to remain trapped within the lattice structure, persisting even after the final sintering process in ambient air – promoting ligand to metal charge transfer (LMCT) [66, 68].

An intriguing and anomalous trend is evident in both Figures 5.9 (a) and 5.9 (b): the PL intensity for both emission features diminish below 200 K, with a pronounced decline occurring within the 150 K–100 K range. Comparable temperature-induced quenching of the D→F transitions has been reported in other Eu-doped oxides [69, 70]. This counterintuitive reduction in emission with decreasing temperature can be rationalized in terms of an enhanced non-radiative decay rate arising from strengthened electron–phonon coupling. Specifically, the multiphonon relaxation rate for rare-earth transitions [71],

$$W_{nr} = C \exp\left(-\frac{\alpha \Delta E}{\hbar \omega_{max}}\right) \tag{5.5}$$

describes the non-radiative decay rate of an excited electronic state via a multiphonon process. Where C is a constant related to electronic matrix element and vibrational frequency. The decay rate depends exponentially on the electron–phonon coupling constant (α), the energy gap ΔE, and the maximum phonon energy $\hbar\omega_{max}$.

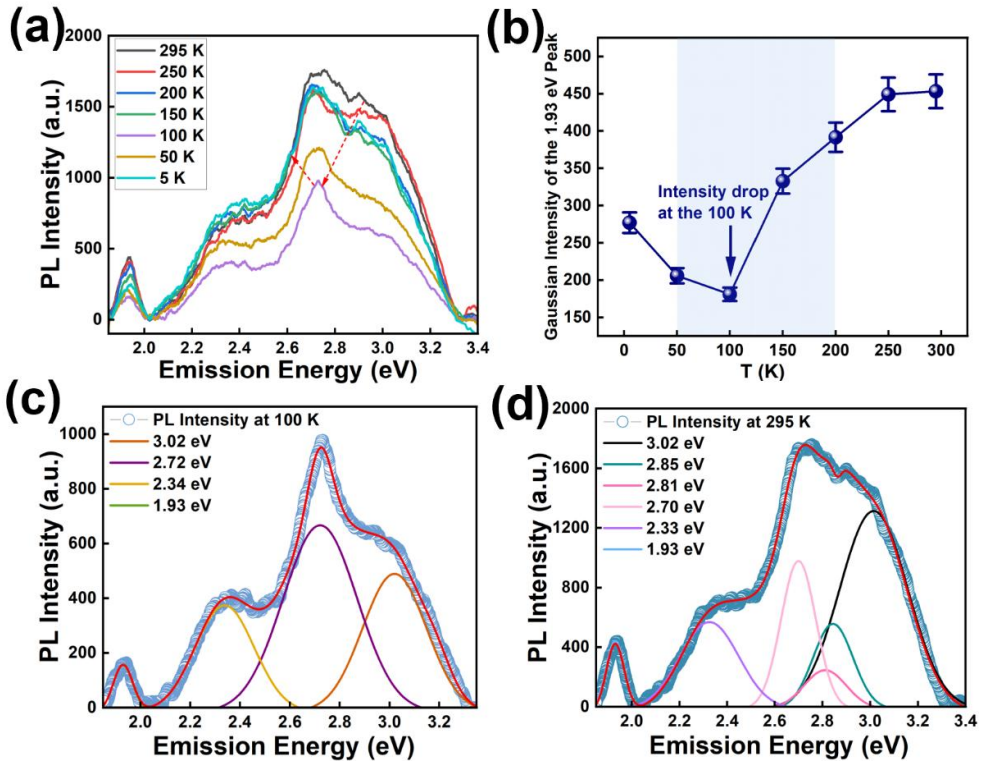

Figure 5.9: (a) PL emission spectra of Eu(Sc/Cr/Fe/Ni/Al)O_3 from 5 K to 295 K with excitation wavelength 343 nm. (b) Gaussian fitted intensity of the 1.93 eV peak exhibits an unusual intensity drop in the temperature range from 150 K to 100 K. (c) The deconvoluted Intensity of the 100 K exhibits peak sharpening. (d) The deconvoluted intensity at 295 K shows a contribution from additional emission bands at higher temperatures.

CHAPTER 6
PROPERTIES OF ENTROPY ENHANCED YITTRUM IRON GARNETS

6.1 Introduction

This chapter inspects the structure-property relationship, effect of local ordering on bulk magnetic and photoluminescence properties and multifunctionality in two entropy enriched garnets compositioned as : $Y_3Fe_4(Sc/Cr/Ga/Al)_1O_{12}$ (Fe80-YIG) and $Y_3Fe_3(Sc/Cr/Ga/Al)_2O_{12}$ (Fe60-YIG) both derived from Yttrium Iron Garnet (YIG). YIG has long been interesting due to intriguing properties that include spin wave, thermochromism, frequency dependance, and low Gilbert damping. However, emerging applications demand the introduction of configurational entropy into YIG, supporting technologies such as cluster-glass reservoir computing, phosphor-converted LEDs (pc-LEDs), photothermal devices, and related systems. Portions of this work are derived from a manuscript currently under review with *Acta Materialia* "*Decoding the role of short-range structural order on magnetic and luminescent properties in entropy-enriched yttrium iron garnets* by Rubayet Tanveer, Dylan Windsor, Cale Overstreet, Tatenda Kanyowa, Bin Hu, Maik K. Lang, Haixuan Xu, Veerle Keppens, William J. Weber."

The deliberate incorporation of compositional heterogeneity – achieved through enhanced configurational entropy [6, 19, 72, 73] – has emerged as a powerful design principle for tailoring functional properties, stabilizing diverse cation chemistries, and introducing controlled structural disorder that can give rise to emergent phenomena. Yet, applying this entropy-driven strategy to the structurally intricate *Ia$\bar{3}$d* garnet framework of $Y_3Fe_5O_{12}$ (YIG) is particularly challenging. The garnet architecture is characterized by site-specific rigidity, especially with respect to substitution at the Fe^{3+} sublattice. In the canonical YIG structure, Y^{3+} exclusively occupies the large dodecahedral sites, while Fe^{3+} is distributed between octahedral and tetrahedral coordination environments (Fig. 6.1). Because Y^{3+} occupancy is fixed, complete substitution is only feasible for smaller trivalent cations such as Al^{3+} and Ga^{3+}, which can accommodate both octahedral and tetrahedral positions. By contrast, larger trivalent cations - e.g., Sc^{3+}, Cr^{3+}, and In^{3+} - can only partially substitute into octahedral sites [74].

To investigate local atomic arrangements beyond the average crystallographic structure, synchrotron X-ray total scattering measurements were analyzed through pair distribution function (PDF) fitting using ensembles of ten relaxed, randomly generated structural models—five for each composition. For each sample, three models enforced exclusive octahedral coordination for Sc^{3+} and Cr^{3+}, while the remaining two permitted full cationic freedom across both octahedral and tetrahedral sublattices, thereby mimicking realistic site disorder among Al^{3+}, Ga^{3+}, Sc^{3+}, and Cr^{3+}. In both compositions, models with constrained octahedral occupancy produced the best agreement with experimental PDF data, indicating a strong preference of Sc^{3+} and Cr^{3+} for octahedral coordination sites.

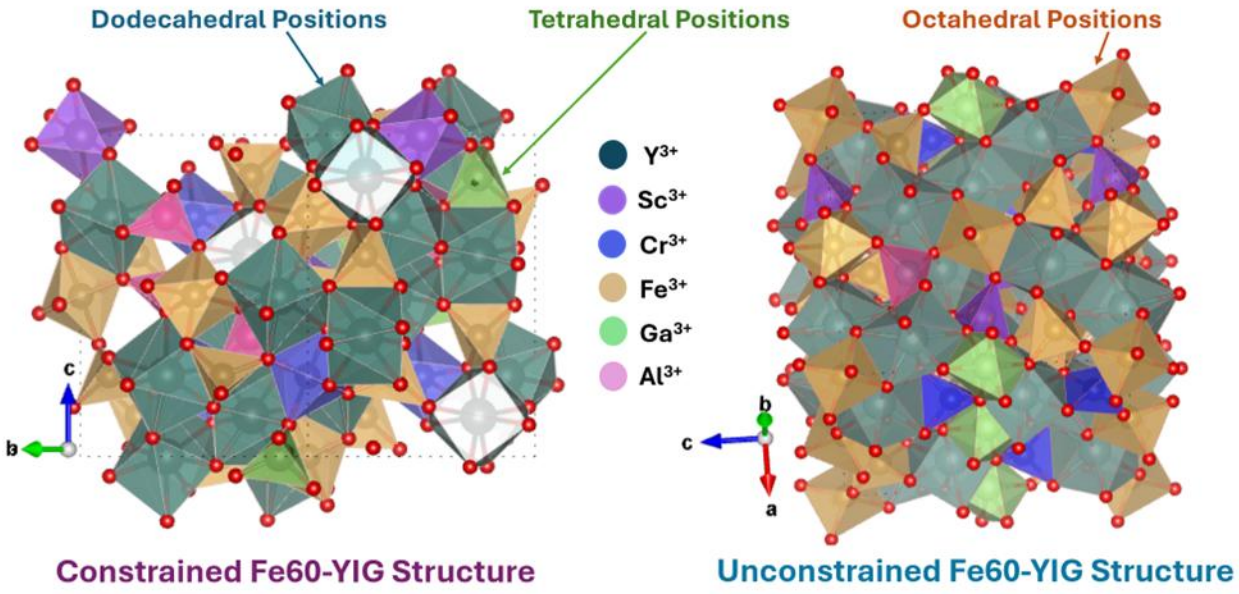

Figure 6.1: Pictorial unit cells of the PDF fitted randomized structure for both constrained (left) and unconstrained (right) Fe60-YIG sample illustrating the structural complexity and compositional disorder inherent to entropy-enhanced garnet structures.

6.2 Average Structure and Phase Purity

Figures 6.2 (a) and 6.2 (b) present the Rietveld-refined X-ray diffraction (XRD) patterns for the synthesized garnet-type structures $Y_3Fe_4(Sc/Cr/Ga/Al)_1O_{12}$ (Fe80-YIG) and $Y_3Fe_3(Sc/Cr/Ga/Al)_2O_{12}$ (Fe60-YIG). Both materials are confirmed to adopt the cubic YIG-like structure with space group *Ia3̄d*, as evidenced by the agreement between the experimental and calculated diffraction profiles. The Fe80-YIG sample exhibits a single-phase pattern with no detectable signatures of secondary crystalline phases, indicating successful phase-pure synthesis under the applied conditions. In contrast, the Fe60-YIG sample shows a minor secondary reflection near $2\theta \approx 33.3°$, which corresponds to a trace amount of a $YCrO_3$-like impurity phase [75-77]. The presence of this secondary phase is attributed to the increased Cr content in the Fe60-YIG composition, which likely exceeds the solubility limit under the current synthesis parameters. All observed Bragg peaks are indexed consistently with previously reported patterns for YIG-like garnet structures [78-80].

Figures 6.2(c) and 6.2 (d) depict the room-temperature Raman spectra of the Fe80-YIG and Fe60-YIG compositions, providing details into their local bonding environments and lattice vibrational dynamics. In both materials, the low-frequency region (~100-300 cm^{-1}) is dominated by translational vibrations of Y^{3+} cations, including external lattice modes of $Ga/Al/FeO_4$ tetrahedra and $Sc/Cr/Ga/Al/FeO_6$ octahedra. The intermediate region (~300-600 cm^{-1}) comprises primarily bending vibrations of oxygen atoms within these polyhedral units, typically manifesting as E_g and T_{2g} symmetry modes associated with internal deformations of the Fe, Ga, Al, Cr, and Sc-coordinated sites. The high-frequency modes (~600-800 cm^{-1}) are characterized by strong cation–oxygen stretching vibrations, particularly the symmetric A_{1g} modes attributed to FeO_6, FeO_4 and

substituted Sc/Cr/Ga/AlO_6 octahedra and Ga/AlO_4 tetrahedra. These spectral features and mode assignments are in excellent agreement with previously reported Raman analyses of YIG and related substituted garnet systems [79, 81, 82].

Interestingly, there are some changes in the relative peak intensities especially, the intensity of the highest E_g+T_{2g} translational mode drops as we increase the substitution of Fe sites with other cations. This can be explained in the view of Franck-Condon (FC) principle where the translation intensity can be related as [82, 83],

$$I \propto |\mu_{fi}|^2 \cdot |\langle \chi_f(Q) \mid \chi_i(Q) \rangle|^2 \tag{6.1}$$

where $|\langle \chi_f(Q) \mid \chi_i(Q) \rangle|^2$ is the Franck-Condon factor related to the overlapping between initial and final vibrational states and μ_{fi} is the electronic transition dipole moment.

From the perspective of the FC principle, two primary mechanisms may account for the observed spectroscopic trends upon substitution at Fe^{3+} sites. First, the replacement of Fe^{3+} ($3d^5$) with electronically inert, closed-shell cations such as Al^{3+}, Ga^{3+}, or Sc^{3+} effectively eliminates localized d-electrons, thereby reducing the coupling between electronic and vibrational states. This diminishes the modulation of the polarizability tensor during lattice vibrations, leading to suppressed Raman activity. Second, such substitutions are likely to stiffen the lattice framework, resulting in a reduction of the Franck-Condon factor due to smaller equilibrium displacements along the excited-state potential energy surface [82, 83].

Notably, this effect is particularly pronounced in the A_{1g} mode near 735 cm^{-1}, which corresponds to the symmetric Fe-O stretching vibration within the FeO_6 octahedra. High-frequency Raman modes are inherently sensitive to variations in local bond length, bond strength, and lattice rigidity, thus serving as a direct probe of short-range structural distortions.

Additionally, substitution by lighter cations may increase the amplitude of atomic displacements, enabling transitions to higher vibrational levels and thereby broadening the A_{1g} feature through enhanced multi-phonon scattering processes. Furthermore, these observations are in strong agreement with prior experimental observations involving the substitution of Fe^{3+} with non-3d, lighter cations [84, 85].

6.3 Investigation of Local Bonding Environment

To model the synchrotron X-ray pair distribution function (PDF) data, a total of ten randomly generated structures – five each for the Fe80-YIG and Fe60-YIG samples – were relaxed and analyzed. These structures included both constrained (Sc and Cr cations restricted exclusively to octahedral coordination sites) and unconstrained (Sc and Cr allowed to occupy both octahedral and tetrahedral sites) models. Fig. 6.3 provides total PDF fits for all structural models clearly indicating an extra peak at ~1.5 *Å* for all Fe80-YIG structures which could not be modeled possibly indicating a chemical short-range ordering (CSRO) (total PDFs are also summarized in Fig 6.4 for all the structures).

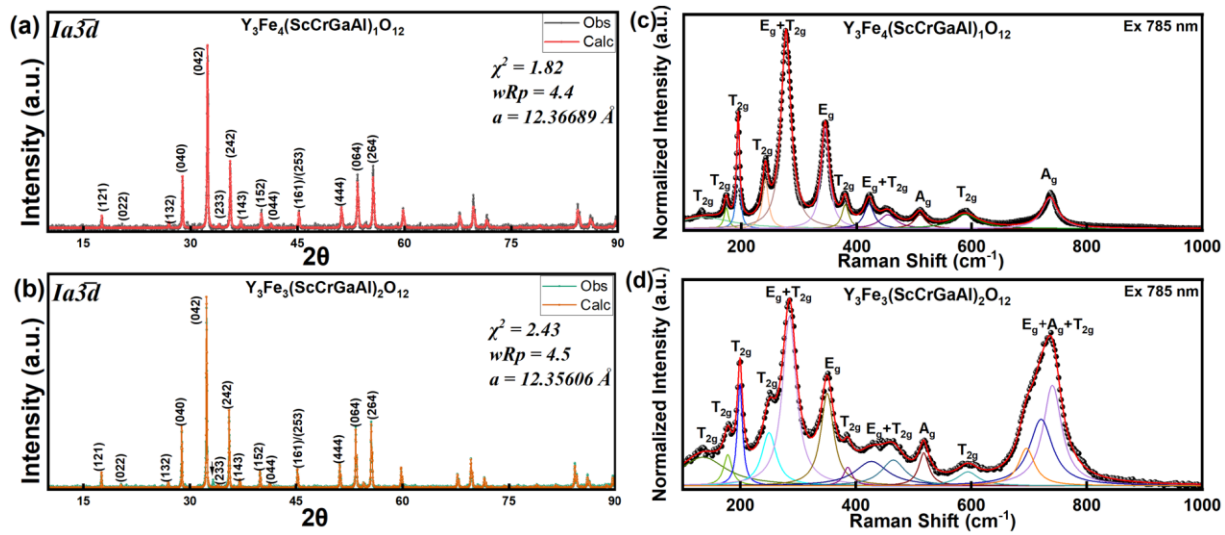

Figure 6.2: Rietveld refined room temperature x-ray diffraction (XRD) patterns of a) $Y_3Fe_4(Sc/Cr/Ga/Al)_1O_{12}$ (Fe80-YIG) and b) $Y_3Fe_3(Sc/Cr/Ga/Al)_2O_{12}$ (Fe60-YIG) fitted with $Ia\bar{3}d$ space group. The arrow indicates a small $YCrO_3$ impurity. Deconvoluted room temperature Raman spectra of c) $Y_3Fe_4(Sc/Cr/Ga/Al)_1O_{12}$ and d) $Y_3Fe_3(Sc/Cr/Ga/Al)_2O_{12}$.

Following the overall fit to the total PDF, individual atomic pair distances were examined through the corresponding partial radial distribution functions (RDFs) to gain deeper insights into local structural environments. For both the constrained and unconstrained structural models applied to the two samples, the Y-Fe partial radial distribution exhibits two well-defined peaks at *~3.13 Å* and *~3.49 Å*, corresponding to Fe atoms occupying tetrahedral and octahedral positions, respectively (Fig. 6.3c and 6.3e). The relative intensities of the tetrahedral and octahedral peaks remain largely consistent across all fitted structures in Fig. 6.3c, indicating that the population of Fe ions occupying these two coordination environments is nearly identical among the Fe80-YIG randomly generated structure models. Interestingly, despite this compositional uniformity, the O-Fe partial radial distribution functions (Fig. 6.3d) exhibit significant variation in both peak position and shape. Notably, at least four of the structures show pronounced asymmetry in the O-Fe distribution, suggestive of distortions in the FeO_6 and FeO_4 polyhedra. In contrast, the first two peaks in Fig. 6.3e clearly exhibits large, inverse intensity variation – representing a complementary distribution of Fe radial function in the Fe60-YIG sample – the structure with highest tetrahedral peak has the lowest octahedral peak and vice versa. Noticeably, the O-Fe peak intensity in Fig. 6.3f systematically shifts to a higher atomic distance as more Fe ions occupy octahedral positions (see Fig. 6.3e). Therefore, unlike the Fe80-YIG system, the variation in the O-Fe peak position in Fe60-YIG primarily arises from the site-selective occupancy of Fe ions, rather than from distortions within a fixed coordination environment.

Fig. 6.3 (g-j) provides the partial radial distribution of O-Y and O-O pairs for the Fe80 and Fe60-YIG samples, respectively. Only one Fe80-YIG structure (constrained structure no. 3, plotted in blue) exhibits an asymmetric distribution for the O-Y pair signifying distorted dodecahedral coordination (Fig. 6.3g). Interestingly, this is the same structure that displayed a symmetric

distribution for O-Fe bonding environment in Fig. 6.3d. This basically implies a definite distortion in Fe80-YIG sample in either Fe-O coordinated octahedral/tetrahedral environment (higher probability), or the Y-O coordinated dodecahedral polyhedron (very unlikely) – this distortion is clearly visible in the total PDF fit for the Fe80-YIG sample (the hump-like peak at ~1.5 Å marked with an arrow in Fig. 6.3a) – possibly indicates a chemical short range order (CSRO) or a clustering among smaller cations (see magnetic behavior discussion below for detail). The O-O partial radial distribution functions, shown in Figs. 6.3h and 6.3j, exhibit a clear peak splitting in the unconstrained structures, indicative of the presence of distinctive O-O bonding environments. This behavior likely originates from the incorporation of large Sc^{3+} ions into both tetrahedral and octahedral sites. The occupation of the smaller, more spatially confined tetrahedral sites by Sc induces significant local strain and polyhedral distortions, thereby stretching the distribution of O-O bond lengths and increasing the structural energy. In contrast, the constrained models – where Sc is restricted to occupy only the octahedral sites – effectively suppress such strain and distortion, promoting greater local symmetry and thermodynamic stability.

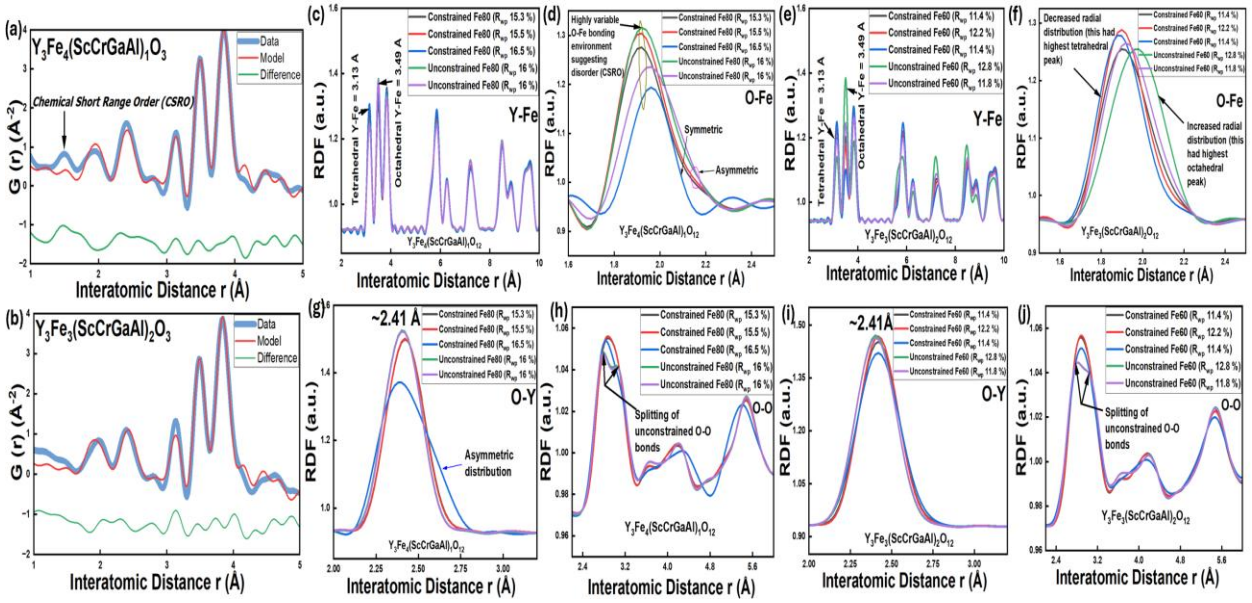

Figure 6.3: Total pair distribution function (PDF) fits for (a) Fe80-YIG and (b) Fe60-YIG. Partial radial distribution functions (RDFs) depicting interatomic correlations for various atomic pairs: (c) Y-Fe and (d) O-Fe distances in Fe80-YIG; (e) Y-Fe and (f) O-Fe distances in Fe60-YIG; (g) O-Y and (h) O-O distances in Fe80-YIG; and (i) O-Y and (j) O-O distances in Fe60-YIG, fitted using both constrained and unconstrained relaxed randomly generated structures to capture variations in local atomic environments.

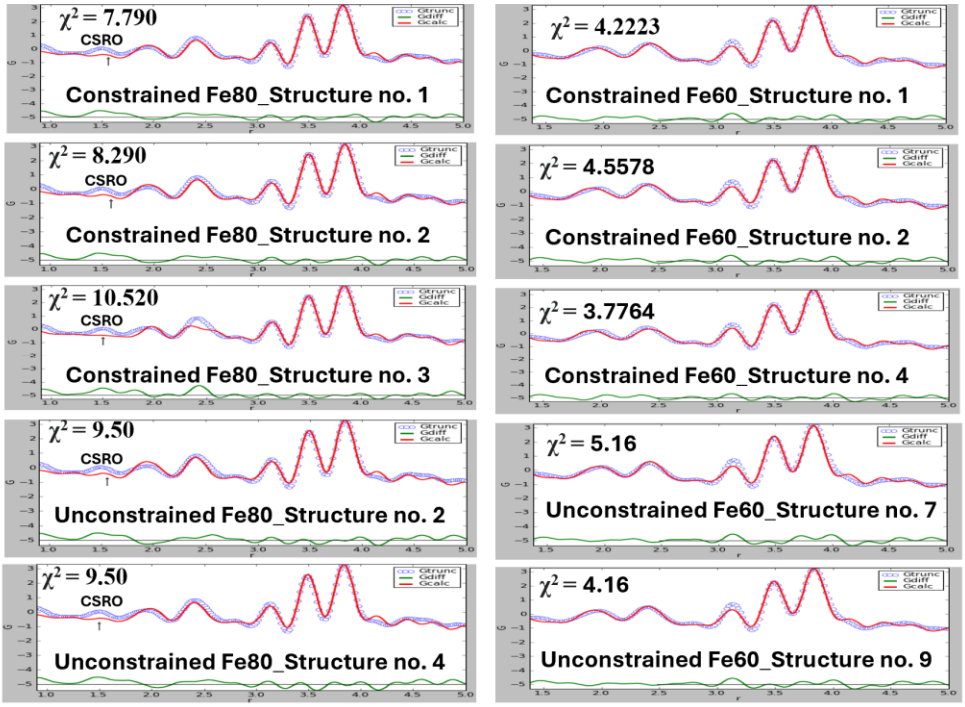

Figure 6.4: Total PDF fits from 1-5 Å with all the constrained and unconstrained structure denoting chemical short-range ordering (CSRO) in Fe80-YIG (left column) sample. The CSRO was not observed in Fe60-YIG (right column).

The partial radial distribution functions corresponding to Y-O and (Cr, Sc, Ga)-O atomic pairs are shown in Fig. 6.5 (a–l). These plots clearly demonstrate that the site-specific occupancy of the substituent cations exerts a significant influence on their local oxygen coordination environment. For each substituting species, an increased occupancy of octahedral sites correlates with a systematic shift of the corresponding cation-oxygen bond distribution toward higher interatomic distances. In contrast, when a greater proportion of a given cation preferentially occupies tetrahedral sites, the same cation-oxygen bonding distribution shifts toward shorter bond lengths. Therefore, in such multicomponent garnet systems, multiple trivalent cations can trade places between tetrahedral and octahedral sites. This should allow a compensating structural effect. For example, if some Al^{3+} moves to octahedral sites (increasing local O–Al bond length), but Ga^{3+} (larger) moves to tetrahedral sites (which would usually shorten O–Ga bonds), these changes should compensate each other volumetrically. So, even if individual bonds stretch or compress, the net unit cell volume remains nearly unchanged – especially when the lattice parameter is a constant.

Figures 6.5 (a–l) further reveal that, in general, the unconstrained structural models exhibit greater local disorder beyond the first coordination shell – particularly in the second and third nearest-neighbor distances – compared to their constrained counterparts, in which Cr^{3+} and Sc^{3+} are restricted to octahedral coordination. Specifically, the unconstrained configurations produce broader, non-Gaussian, and significantly blunted peaks in the partial radial distribution functions for both Cr–O and Sc–O bonding environments, indicative of increased structural heterogeneity

and reduced local symmetry. This observation is further corroborated by both the total PDF fits and comparative DOS calculations, shown in Fig. 6.6, where the constrained models provide superior agreement with the experimental data in the 4-6 Å range (highlighted with an arrow). These results strongly support the conclusion that Cr and Sc preferentially stabilize in octahedral coordination. It is also evident from Fig. 6.5 (e–h) that Sc^{3+} can induce the greatest degree of local structural disorder among the dopant species, likely attributable to its relatively large ionic radius. Even minor variations in the site occupancy of Sc^{3+} result in pronounced shifts in the Sc-O bonding distances, reflecting the high sensitivity of the local coordination environment to the spatial constraints imposed by Sc incorporation.

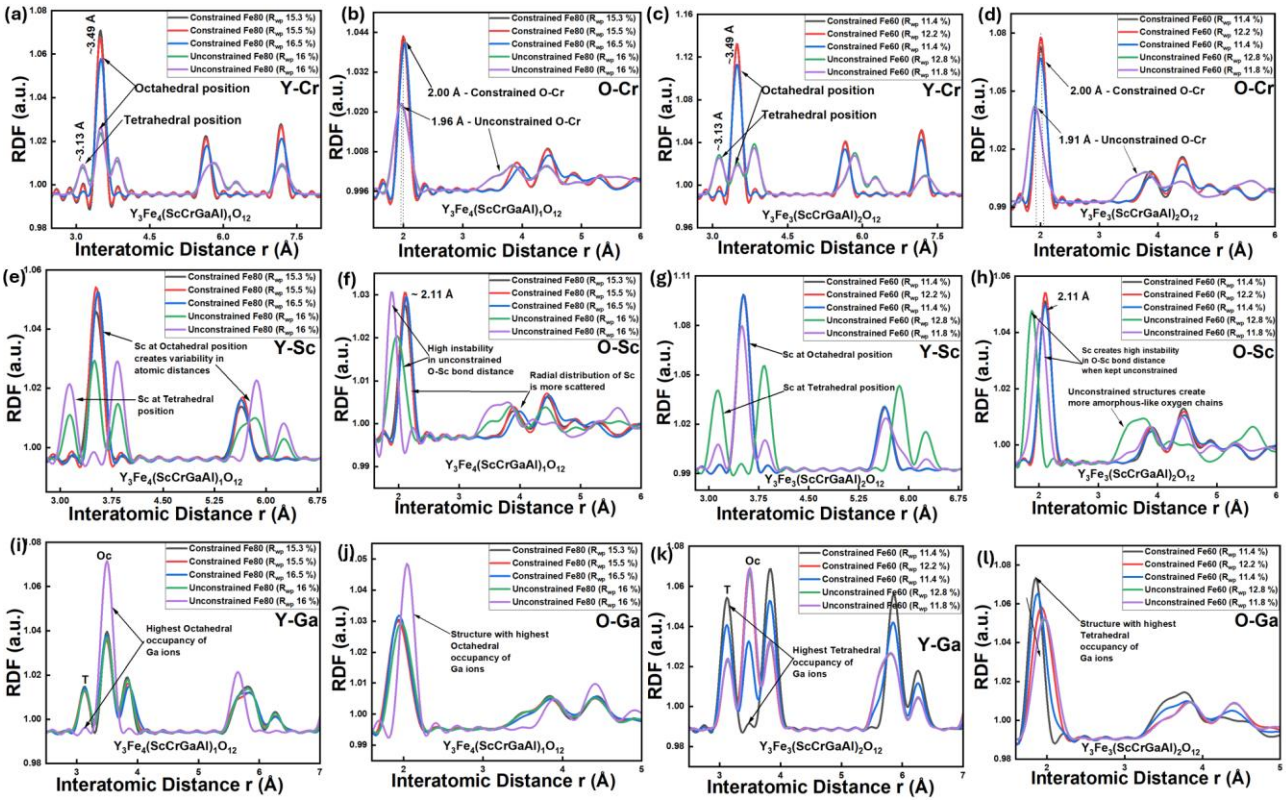

Figure 6.5: Partial radial distribution functions (RDFs) depicting interatomic correlations for substituting atomic pairs: (a) Y-Cr and (b) O-Cr distances in Fe80-YIG; (c) Y-Cr and (d) O-Cr distances in Fe60-YIG; (e) Y-Sc and (f) O-Sc distances in Fe80-YIG; (g) Y-Sc and (h) O-Sc distances in Fe60-YIG; (i) Y-Ga and (j) O-Ga distances in Fe80-YIG; (k) Y-Ga and (l) O-Ga distances in Fe60-YIG, fitted using both constrained and unconstrained relaxed randomly generated structures.

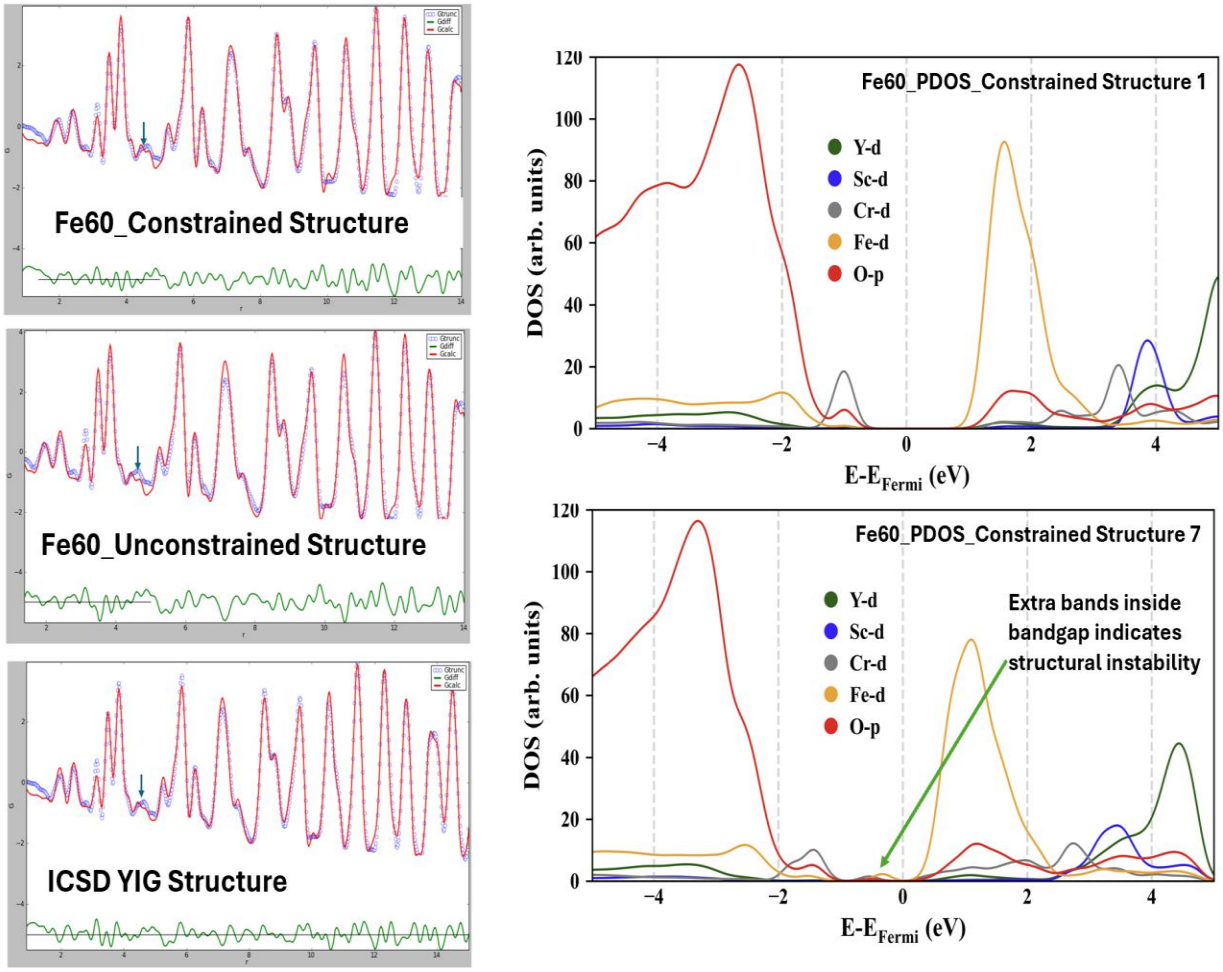

Figure 6.6: Total pair distribution function (PDF) refinements were performed over the real-space range of 1–14 Å for Fe60-YIG using three structural models: (Top-left) constrained randomly generated structures with Sc^{3+} and Cr^{3+} restricted to octahedral sites, (Mid-left) unconstrained randomly generated structures with full site disorder among all substituent cations, and (Bottom-left) the ICSD reference YIG structure [86] (ICSD #45679) for baseline comparison. The left column this illustrates that both the constrained model and the ICSD-based structure yielded significantly improved agreement in the intermediate-range correlations (particularly from ~4 to 6 Å) relative to the unconstrained model, highlighting the importance of site-specific cation ordering. The right panel compares the electronic density of states (DOS) of representative constrained and unconstrained structures, showing that the unconstrained configurations exhibit pronounced mid-gap states – indicative of local structural instability and potential defect states – whereas the constrained structures preserve a clean bandgap consistent with the known electronic structure of YIG.

6.4 Investigation of Magnetic Properties

Figure 6.7 (a) presents the temperature-dependent magnetization of the Fe80-YIG sample measured between *2 K* and *390 K* under both zero-field-cooled (ZFC) and field-cooled (FC) conditions at an applied field of 100 Oe. The data indicate that the system approaches its Curie temperature (T_c) near *390 K*, although the instrumental limitations prevent us from extending the data through the transition. The ZFC-FC bifurcation observed below *145 K*, is indicative of a spin glass–like state. The heat capacity (C_p) measured from *2 K* to *250 K* does not reveal any anomalies near the bifurcation point, suggesting the presence of a non-equilibrium cluster glass-like state [Fig. 6.7 (c)]. However, at elevated temperatures, two broad features appear at *~324 K* and *~348 K* in the C_p vs T data, which are further corroborated by pronounced peaks in the temperature derivatives dC_p/dT and dM/dT vs T data (see Figs. 6.8 a–6.8 d), indicating multiple competing magnetic phases within the system.

The emergence of glassy magnetic behavior in the Fe80-YIG sample can be rationalized in the context of chemical short-range ordering (CSRO), as evidenced by a distinct peak in the experimental pair distribution function (PDF) at ~1.5 Å (see Fig. 6.4) and corroborated by recent experimental studies. Specifically, Mössbauer spectroscopy studies have shown that substitution of Fe^{3+} by Al^{3+} – a dopant with a significantly smaller ionic radius – preferentially and predominantly populates tetrahedral sites in the YIG lattice, thereby inducing multiple magnetic blocking temperatures and bifurcation in ZFC-FC magnetization curves at comparable temperature ranges to those observed in this work [87, 88]. This interpretation is consistent with the pronounced peak near *1.5 Å* in our experimental PDF data, a feature that cannot be reproduced by either the randomly generated models or standard YIG structural files. Notably, the Shannon crystal radii of tetrahedral coordination for Al^{3+} and O^{3+} are *~0.53 Å* (can be as low as *0.39 Å* depending on the coordination) and *~1.24 Å*, respectively [89]. As illustrated previously in the PDF section, occupation of tetrahedral sites tends to reduce the metal-oxygen bond length, and the presence of local clustering with oxygen vacancy ordering may further shorten this distance, leading to the appearance of a localized Al-O peak at *~1.5 Å*. In the canonical YIG structure, long-range magnetic ordering predominantly arises from superexchange interactions along $Fe^{3+}(T)–O^{2-}–Fe^{3+}(Oc)$ pathways, involving tetrahedral and octahedral iron sites. However, in the current system, partial substitution of Fe^{3+} by Cr^{3+} at octahedral sites introduces *Fe-O-Cr* linkages into the magnetic network. This structural modification, when compounded by chemical short-range order (CSRO) and local cation clustering, disrupts the integrity of the *Fe-O-Fe* exchange framework. Concurrent structural distortions – such as Al-rich cluster formation or oxygen sublattice displacements – further perturb local bond angles and bond lengths, altering the magnetic exchange coupling constant (J). Therefore, many *Fe-O-Fe* and *Fe-O-Cr* interaction chains become spatially inhomogeneous – leading to regions that order at different temperatures – forming distributed spin-freezing events.

The temperature-dependent magnetization behavior of the Fe60-YIG sample is presented in Fig. 6.7 (d). Both zero-field-cooled (ZFC) and field-cooled (FC) curves exhibit a well-defined ferromagnetic-to-paramagnetic transition, with an apparent Curie temperature (T_c) at *260 K*. This transition is further substantiated by the field-dependent magnetization (M–H) data, which shows clear saturation at *260 K* but a fully paramagnetic response at *300 K* (Fig. 6.7 (e)). Correspondingly, the heat capacity (C_p) data reveals a subtle anomaly at *~260 K* (Fig. 6.7 (f)), consistent with the

magnetic transition. This T_c is further validated by the inflection points in the temperature derivative of magnetization (*dM/dT*) and the inverse magnetization (*1/M*) plot (see Figs. 6.8 e-6.8 f). Interestingly, comparing the dM/dT plots from both samples, it is apparent that Fe80-YIG exhibits significantly more pronounced glassy behavior compared to the Curie-Weiss behavior of Fe60-YIG. The glassy magnetic response of the Fe80-YIG sample can be predominantly attributed to the presence of chemical short-range ordering (CSRO) and local cationic clustering, as evidenced by the PDF analysis.

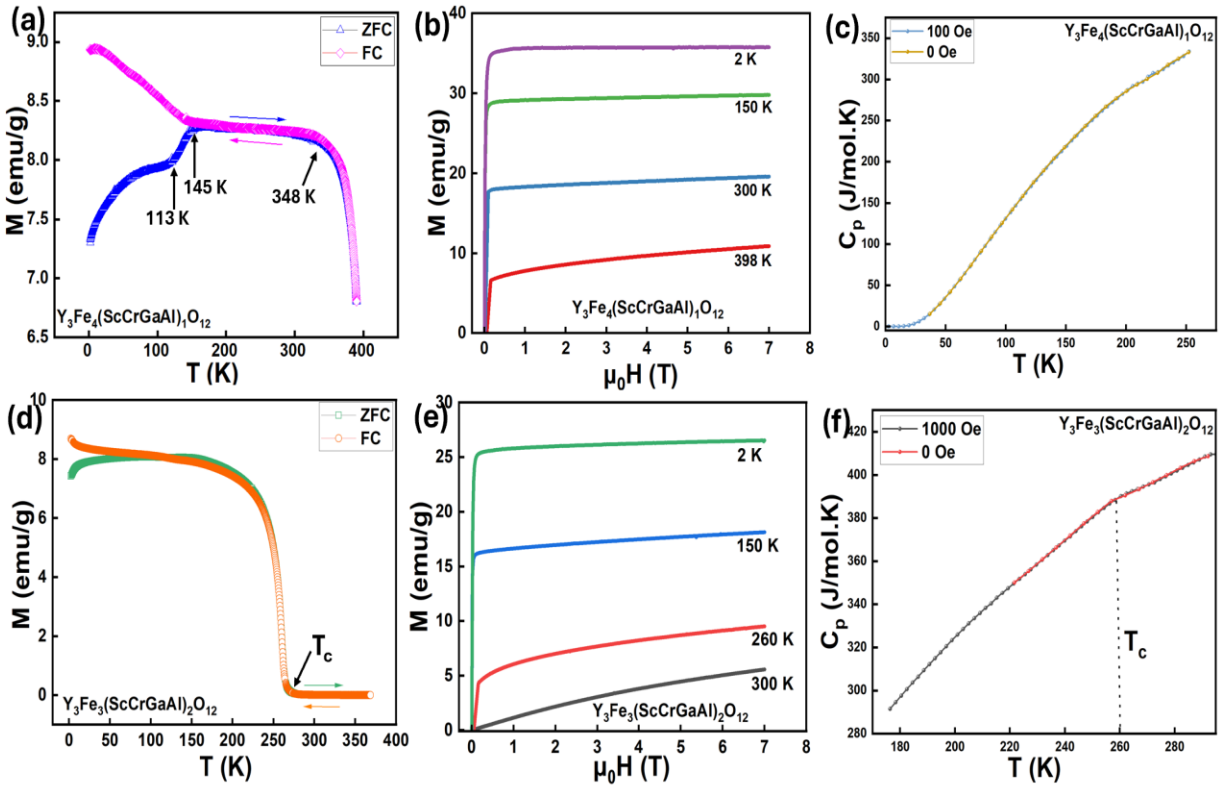

Figure 6.7: Magnetic behavior of the garnet samples: (a) Temperature-dependent magnetization curves for the Fe80-YIG composition under zero-field-cooled (ZFC) and field-cooled (FC) conditions measured at an applied field of 100 Oe, (b) Magnetic moment vs field at different temperature regimes and (c) Heat capacity (C_p) as a function of temperature for Fe80-YIG, revealing no thermodynamic signatures near ZFC-FC bifurcation; (d) Magnetic moment vs Temperature (ZFC and FC collected at 100 Oe), (e) Magnetic moment vs field at different temperature regimes and (f) Temperature dependent heat-capacity showing clear deflection at the curie temperature (T_c) for the Fe60-YIG sample.

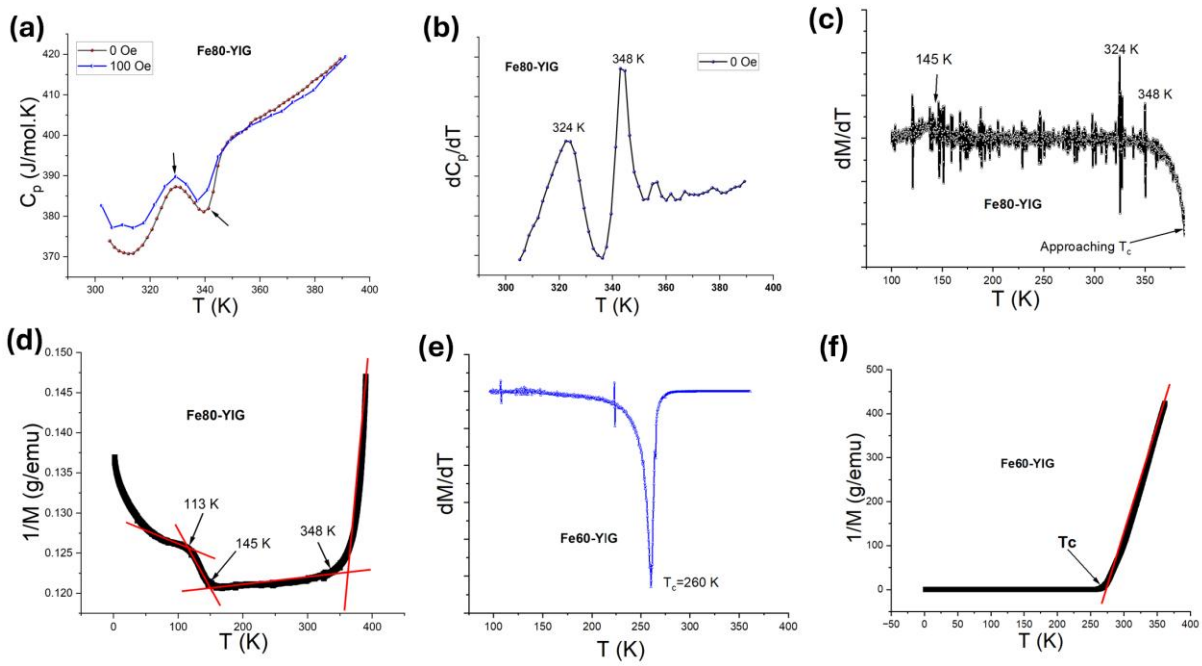

Figure 6.8: (a-b) Higher temperature data of the heat capacity and its derivative vs. temperature for Fe80-YIG. (c and e) showing derivative magnetization vs. T data for both samples – also showing a glassier magnetic nature of the Fe80-YIG sample. (d & f) Inverse magnetic moment (susceptibility should follow the same trend) plot showing perfect Curie-Weiss nature of the Fe60 sample.

To further investigate the spin glass behavior in Fe80-YIG, AC susceptibility data were collected at different frequencies with *0 Oe* applied dc field (Fig 6.9a and 6.9b). Both real and imaginary parts exhibit a large variation in their peak position with a shift to higher temperatures and a drop in their intensity with increasing frequencies which is a dynamic feature for the spin glass system. To further elucidate this behavior, we calculated the $\Delta T_f/[T_f log\ (\omega)]$ factor. For canonical spin glass systems, the value of this factor should be around ~ *0.010* to ~ *0.0050*, for cluster glasses *~0.050 - ~0.020* and the factor exhibits a much higher value ~ 0.30 for superparamagnets [90-93]. For our Fe80-YIG sample, we obtain a value of ~ *0.0270*, which suggests a cluster glass like behavior. For magnetically interacting clusters the Vogel-Fulcher law is given as,

$$\omega = \omega_0 \exp\left[-E_a/k_B(T_f - T_0)\right]$$

Where, ω is the driving frequency, E_a is the activation energy for spin flips and T_0 represents the Vogel-Fulcher temperature generally represents interaction strengths between the spins. Fitting a selected blocking temperature (T_f) position at varying frequencies using above equation yields characteristic relaxation time $\tau_0 = 10^{-8}s$, again consolidating the cluster-glass hypothesis (Fig 6.9c).

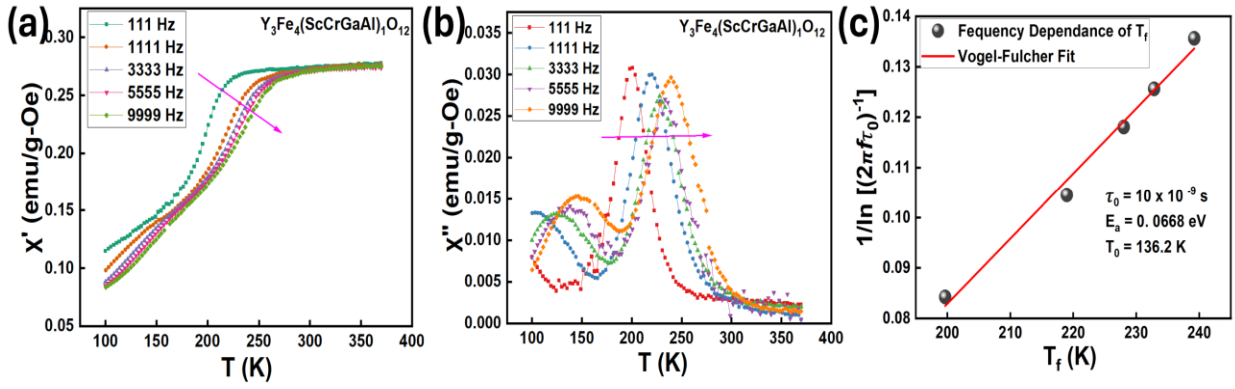

Figure 6.9: AC susceptibility data for the (a) Real (χ') and (b) Imaginary (χ'') part with varying frequency range collected at 0 Oe; and (c) Variation of a selected blocking temperature (here termed as T_f) with the frequency of the applied AC field, fitted with Vogel-Fulcher law.

6.5 Investigation of Luminescent Properties

The temperature-dependent photoluminescence (PL) spectra and corresponding room-temperature deconvoluted emission bands are shown in Fig. 6.10 (a–d). For both Fe80-YIG and Fe60-YIG samples, most PL bands exhibit a pronounced enhancement in intensity as the temperature decreases, consistent with reduced non-radiative recombination pathways at lower thermal energies. Notably, a distinct emission band at *2.07 eV* in the Fe60-YIG sample diminishes and ultimately vanishes at cryogenic temperatures – likely due to the suppression of vibronic coupling and the reduced efficacy of phonon-assisted transitions in this regime.

All observed emission peaks within the *2.49–3.00 eV* range are attributed to the spin-allowed $^4T_1 \rightarrow {}^4A_2$ transitions of Cr^{3+} ions [94]. Among these, the dominant peak near *~2.7 eV* displays a marked increase in intensity and narrowing in the Fe60-YIG sample compared to Fe80-YIG. The rise in the intensity (see Fig. 6.11) reinforces the assignment of the transition to Cr^{3+}, as Fe^{3+} is progressively substituted by Cr^{3+} in this composition. Additionally, the observed spectral narrowing of the emission bands indicates increased localization of the electronic transitions, suggesting a more uniform and homogeneous crystal field environment. This spectral sharpening likely reflects a suppression – or potential elimination – of the chemical short-range ordering (CSRO) that was prominent in the Fe80-YIG sample.

To understand the complete process we consider, the *343 nm* laser excites charges from O^{2-} to Fe^{3+} and Cr^{3+} which likely promotes the electrons to higher-energy states. These excited electrons then undergo radiative recombination back to the Cr^{3+} ground state, following spin-allowed selection rules. Interestingly, excited electrons from Fe^{3+}, if they recombine radiatively, should recombine to $^4A_2$ ground state of Cr^{3+} to satisfy the spin selection rule and decent amount of orbital overlapping. A schematic energy level diagram, incorporating the calculated electronic density of states (DOS) and the Tanabe–Sugano diagram, is provided in Fig. 6.12 to illustrate these transitions.

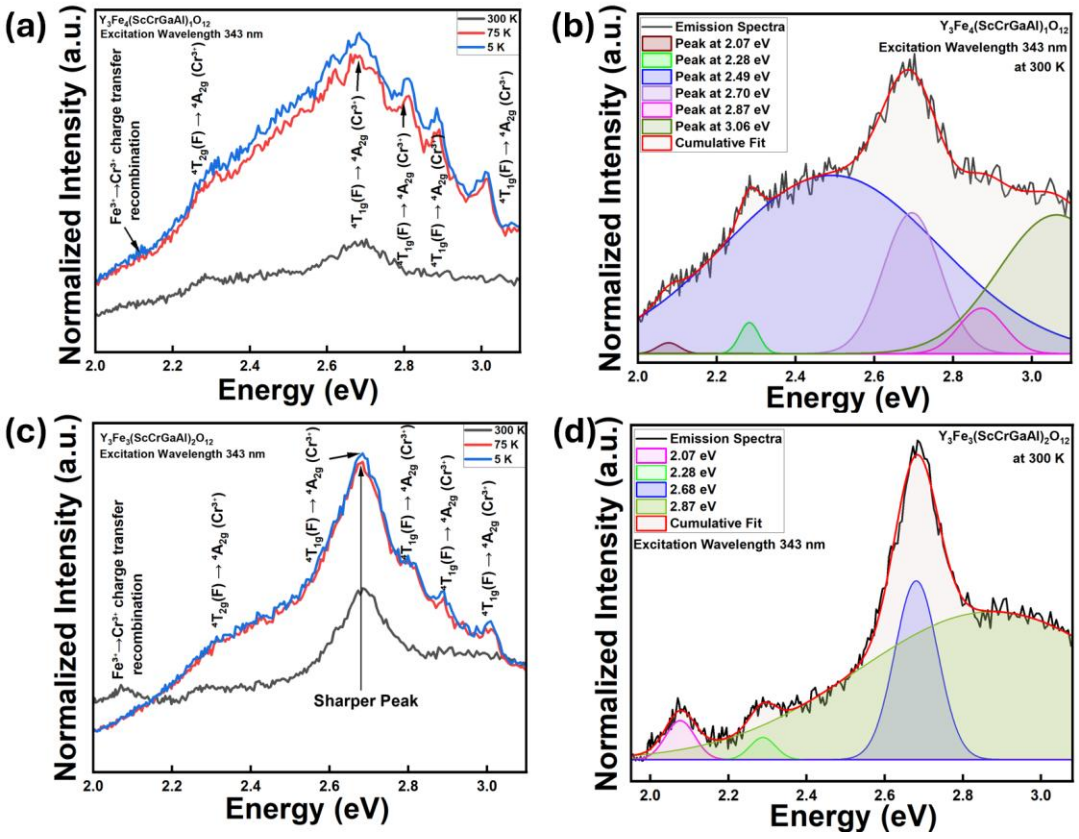

Figure 6.10: Temperature-dependent photoluminescence (PL) response of garnet samples. (a) PL emission spectra of Fe80-YIG as a function of temperature, highlighting thermally induced spectral changes; (b) Deconvolution of the room-temperature (300 K) PL spectrum for Fe80-YIG, illustrating individual emission contributions. (c) Temperature-dependent PL spectra of the Fe60-YIG sample, revealing distinct emission behavior compared to Fe80-YIG; (d) Deconvoluted PL spectrum of Fe60-YIG at 300 K, showing the relative contributions of individual electronic transitions.

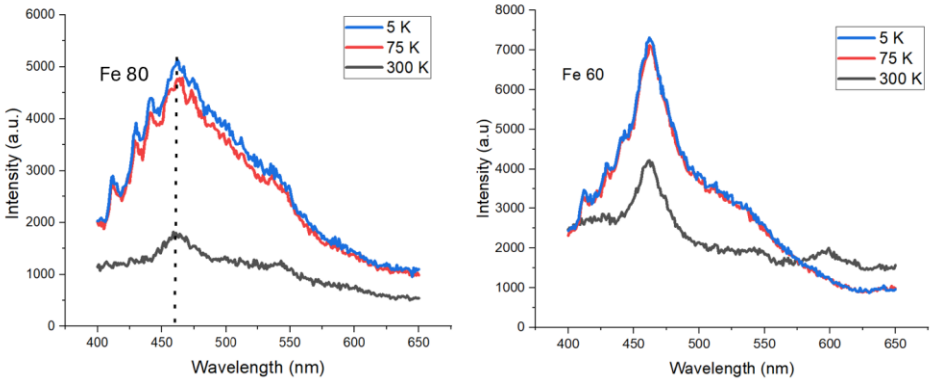

Figure 6.11: PL data for both samples on wavelength scale showing higher intensity for Fe60-YIG sample for a same selected area and applied current.

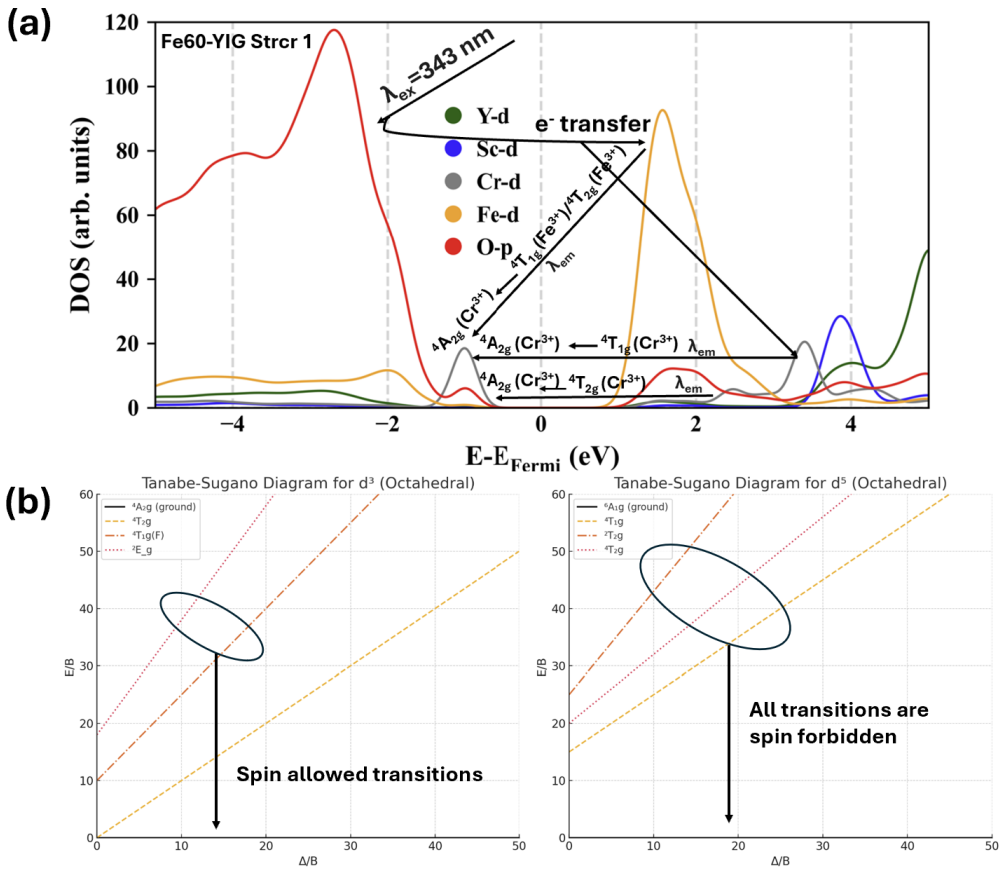

Figure 6.12: A detailed illustration of the transition bands with calculated DOS and Tanabe-Sugano diagram emphasizing spin-allowed transitions.

CHAPTER 7
CONCLUSION

7.1 Summary of Findings

In this dissertation we have explored the synthesis, structure, and multifunctional properties of compositionally complex oxides across two different crystallographic frameworks, orthoferrite/orthochromite-perovskites, and garnets with yttrium iron garnet (YIG) as model structure. Through the combinations of synthesis, advanced characterization, and structure-property correlation, we have investigated how configurational entropy can be leveraged to modulate lattice distortion, cationic distribution, and inclusion of more than one functional property.

In the first part, the high-entropy design concept was employed to synthesize a suite of polycrystalline rare-earth perovskite oxides $REBO_3$ (RE = rare earth; B = $Sc_{0.2}Al_{0.2}Cr_{0.2}Ni_{0.2}Fe_{0.2}$). Despite the significant size diversity introduced by five disparate transition-metal cations on the B site, all compositions successfully crystallized in the orthorhombic *Pnma* perovskite structure. The structural stability of this framework attests to its remarkable flexibility to accommodate both ionic-size mismatches. Temperature-dependent transport measurements revealed thermally activated electronic conductivity. Meanwhile, magnetic measurements uncovered low-temperature ordering transitions in $PrBO_3$, $SmBO_3$, $EuBO_3$ and $LaBO_3$. These results highlight the feasibility of entropy inspired engineering in tailoring the functional properties, providing a new route to systematically tune functional responses through controlled disorder.

The second part of the dissertation focused on a detailed structural and functional investigation of $Eu(Sc/Cr/Fe/Ni/Al)O_3$ – a member of the RESCFNA family, representing a model high-entropy perovskite with pronounced electronic and magnetic originating from B-site and plausible luminescent behavior from A-site Eu. A comprehensive suite of structural, vibrational, electronic, and thermodynamic characterization techniques was employed to unravel the underlying structure–property correlations. Raman spectroscopy confirmed a bonding environment consistent with orthorhombic *Pnma* symmetry, while small-box pair distribution function (PDF) refinements using relaxed special quasi-random structures (SQS) uncovered anomalous local bonding environments – short Eu–Ni and long Ni–O bond distances were observed, suggesting preferential Eu–Ni electrostatic interactions. Temperature-dependent X-ray diffraction detected a distinct structural anomaly near 140 K, coinciding with changes in the slope of $\ln(\rho/T)$ vs $1/T$ and with reproducible features in the AC phase-angle response against temperature. Within the framework of Holstein's small-polaron model, these observations were interpreted as a transition in conduction mechanism – from high-temperature $Ni^{2+} \leftrightarrow Ni^{3+}$ hopping to a low-temperature regime dominated by $Cr^{3+} \leftrightarrow Cr^{4+}$ or oxygen-vacancy-mediated transport. Complementary magnetic studies confirmed long-range antiferromagnetic ordering near 17 K, along with thermodynamic studies indicating disproportionated sublattice ordering around ~140–130 K – corroborating the temperature dependent XRD and resistivity data. Photoluminescence (PL) measurements further supported this interpretation, showing strong quenching of Eu^{2+}/Eu^{3+}-based emission below 150 K, consistent with enhanced non-radiative relaxation mediated by multiphonon coupling and polaron formation. Collectively, these results elucidate how chemical disorder and correlated electron–phonon interactions cooperate to produce strongly coupled structural, electronic, and magnetic responses in high-entropy perovskites.

In the third part of this dissertation, we have applied the configurational entropy enhancement strategy to yttrium iron garnet ($Y_3Fe_5O_{12}$, YIG) to induce multifunctionality. Here, the configurational entropy of the Fe^{3+} sublattice was systematically changed through partial

substitution with multiple iso-valent cations (Sc^{3+}, Cr^{3+}, Ga^{3+}, and Al^{3+}), despite the intrinsic rigidity and site selectivity of the garnet structure. High-resolution synchrotron total-scattering (PDF) analysis, using ensembles of relaxed randomly generated structural models, provided insights into local atomic arrangements, cation-site preferences and their impact on oxygen bonding environment, local ordering inaccessible via conventional XRD or Raman methods.
Importantly, in the composition $Y_3Fe_4(Sc/Cr/Ga/Al)_1O_{12}$, the PDF results identified a cluster-like chemical short-range order (CSRO) manifested as Al^{3+} ions predominantly occupying tetrahedral positions. We also predicted that this selective occupation disrupted extended Fe-O-Fe superexchange pathways, introducing magnetic inhomogeneity that fragmented spin networks and gave rise to cluster-glass behavior at low temperatures. Simultaneously, Cr^{3+} incorporation modified the local crystal-field symmetry and enhanced photoluminescence intensity, imparting additional luminescent functionality.

7.2 Broader Implications

When taken together, these studies advance the understanding and the role of configurational entropy as a new frontier in multifunctional materials design. Our study demonstrates that compositional disorder, when judiciously engineered, is not a mere perturbation but a controllable design parameter capable of governing energy landscapes, carrier generation and mobility, magnetic ordering, and luminescence. The investigated tolerance of both the perovskite and garnet frameworks to vast chemical diversity somehow challenges the long-held notion that structural order and functional performance are mutually exclusive. Instead, the results reveal that localized distortions, electrostatic asymmetries, and short-range order can be harnessed to elicit emergent functionalities inaccessible in conventional, compositionally simple oxides.

7.3 Future Work

Multiple other advanced characterization techniques like electron-energy loss spectroscopy (EELS), or Mössbauer spectroscopy can be applied to this group of samples to experimentally verify the precise charge states of the cations. Temperature-dependent synchrotron data can provide more information about local ordering at various temperature-regimes which could also be correlated with other functional characterization techniques. Chemical-short range order (CSRO) could also be investigated via high resolution transmission electron microscopy. Using machine learning models with combination of Extended X-ray absorption fine structure (EXAFS) for all the reported structures could also provide plethora of local structural information.

Bibliography

1. Goodenough, J.B., *Electronic and ionic transport properties and other physical aspects of perovskites.* Reports on Progress in Physics, 2004. **67**(11): p. 1915.
2. Torrance, J., et al., *Systematic study of insulator-metal transitions in perovskites R NiO 3 (R= Pr, Nd, Sm, Eu) due to closing of charge-transfer gap.* Physical Review B, 1992. **45**(14): p. 8209.
3. Coey, J.M., *Magnetism and magnetic materials*. 2010: Cambridge university press.
4. Taheri, M., et al., *Magnetic structure, magnetoelastic coupling, and thermal properties of EuCrO 3 nanopowders.* Physical Review B, 2016. **93**(10): p. 104414.
5. Jien-Wei, Y., *Recent progress in high entropy alloys.* ann. Chim. sci. Mat, 2006. **31**(6): p. 633-648.
6. Rost, C.M., et al., *Entropy-stabilized oxides.* Nature communications, 2015. **6**(1): p. 8485.
7. Jin, T., et al., *Mechanochemical-assisted synthesis of high-entropy metal nitride via a soft urea strategy.* Advanced materials, 2018. **30**(23): p. 1707512.
8. Sarker, P., et al., *High-entropy high-hardness metal carbides discovered by entropy descriptors.* Nature communications, 2018. **9**(1): p. 4980.
9. Zhivulin, V., et al., *Impact of the A-site rare-earth ions (Ln3+–Sm3+, Eu3+, Gd3+) on structure and electrical properties of the high entropy LnCr0. 2Mn0. 2Fe0. 2Co0. 2Ni0. 2O3 perovskites.* Ceramics International, 2022. **48**(7): p. 9239-9247.
10. Tanveer, R., et al., *Synthesis and properties of rare-earth high-entropy perovskite.* Applied Physics Letters, 2024. **124**(21).
11. Yin, Y., et al., *Spin-glass behavior and magnetocaloric properties of high-entropy perovskite oxides.* Applied Physics Letters, 2022. **120**(8).
12. Callister Jr, W.D. and D.G. Rethwisch, *Materials science and engineering: an introduction*. 2020: John wiley & sons.
13. Rahaman, M., *Kinetics and mechanisms of densification*, in *Sintering of advanced materials*. 2010, Elsevier. p. 33-64.
14. McCusker, L., et al., *Rietveld refinement guidelines.* Applied Crystallography, 1999. **32**(1): p. 36-50.
15. Egami, T. and S.J. Billinge, *Underneath the Bragg peaks: structural analysis of complex materials*. Vol. 16. 2003: Elsevier.
16. Petkov, V., *Pair distribution functions analysis.* Characterization of Materials, 2012. **1361**.
17. Ekin, J., *Experimental techniques for low-temperature measurements: cryostat design, material properties and superconductor critical-current testing*. 2006: Oxford university press.
18. Migliori, A., et al., *Resonant ultrasound spectroscopic techniques for measurement of the elastic moduli of solids.* Physica B: Condensed Matter, 1993. **183**(1-2): p. 1-24.
19. Sarkar, A., et al., *Rare earth and transition metal based entropy stabilised perovskite type oxides.* Journal of the European Ceramic Society, 2018. **38**(5): p. 2318-2327.
20. Zhivulin, V.E., et al., *Polysubstituted high-entropy [LaNd](Cr0. 2Mn0. 2Fe0. 2Co0. 2Ni0. 2) O3 perovskites: correlation of the electrical and magnetic properties.* Nanomaterials, 2021. **11**(4): p. 1014.
21. Taguchi, H., *Relationship between crystal structure and electrical properties of Nd (Cr1− xFex) O3.* Journal of Solid State Chemistry, 1997. **131**(1): p. 108-114.

22. Zhivulin, V., et al., *Effect of configurational entropy on phase formation, structure, and magnetic properties of deeply substituted strontium hexaferrites.* Ceramics International, 2023. **49**(1): p. 1069-1084.
23. Warshi, M.K., et al., *Structural, optical and electronic properties of RFeO3.* Ceramics International, 2018. **44**(7): p. 8344-8349.
24. Gupta, M., O.V. Rambadey, and P.R. Sagdeo, *Probing the effect of R-cation radii on structural, vibrational, optical, and dielectric properties of rare earth (R= La, Pr, Nd) aluminates.* Ceramics International, 2022. **48**(16): p. 23072-23080.
25. Kumar, S., et al., *Structural, magnetic, magnetocaloric and specific heat investigations on Mn doped PrCrO3 orthochromites.* Journal of Physics: Condensed Matter, 2017. **29**(19): p. 195802.
26. Tiwari, B., et al., *Magnetostructural and magnetocaloric properties of bulk LaCrO3 system.* Materials Research Express, 2015. **2**(2): p. 026103.
27. Guo, H., et al., *Antiferromagnetic correlations in the metallic strongly correlated transition metal oxide LaNiO3.* Nature communications, 2018. **9**(1): p. 43.
28. Azad, A., et al., *Structural and magnetic properties of LaFe0. 5Cr0. 5O3 studied by neutron diffraction, electron diffraction and magnetometry.* Materials research bulletin, 2005. **40**(10): p. 1633-1644.
29. Zhang, J., et al., *Long-range antiferromagnetic order in a rocksalt high entropy oxide.* Chemistry of Materials, 2019. **31**(10): p. 3705-3711.
30. Coey, J., *Amorphous magnetic order.* Journal of Applied Physics, 1978. **49**(3): p. 1646-1652.
31. Acharya, S., et al., *Multiferroic behavior of lanthanum orthoferrite (LaFeO3).* Materials Letters, 2010. **64**(3): p. 415-418.
32. Li, E., et al., *Spin switching in single crystal PrFeO3 and spin configuration diagram of rare earth orthoferrites.* Journal of Alloys and Compounds, 2019. **811**: p. 152043.
33. Lee, J.-H., et al., *Spin-canting-induced improper ferroelectricity and spontaneous magnetization reversal in SmFe O 3.* Physical review letters, 2011. **107**(11): p. 117201.
34. Woodfield, B.F., M.L. Wilson, and J.M. Byers, *Low-temperature specific heat of La 1− x Sr x MnO 3+ δ.* Physical review letters, 1997. **78**(16): p. 3201.
35. Sreedhar, K., et al., *Electronic properties of the metallic perovskite LaNiO 3: Correlated behavior of 3d electrons.* Physical Review B, 1992. **46**(10): p. 6382.
36. Cao, M.-H., et al., *Suppressing the chromium disproportionation reaction in O3-type layered cathode materials for high capacity sodium-ion batteries.* Journal of Materials Chemistry A, 2017. **5**(11): p. 5442-5448.
37. Jiang, B., et al., *Probing the local site disorder and distortion in pyrochlore high-entropy oxides.* Journal of the American Chemical Society, 2020. **143**(11): p. 4193-4204.
38. Gussev, I.M., et al., *Systematic study of short-and long-range correlations in RE 3 TaO 7 weberite-type compounds by neutron total scattering and X-ray diffraction.* Journal of Materials Chemistry A, 2023. **11**(16): p. 8886-8903.
39. Varignon, J., et al., *Complete phase diagram of rare-earth nickelates from first-principles.* npj Quantum Materials, 2017. **2**(1): p. 21.
40. Green, R.J., M.W. Haverkort, and G.A. Sawatzky, *Bond disproportionation and dynamical charge fluctuations in the perovskite rare-earth nickelates.* Physical Review B, 2016. **94**(19): p. 195127.

41. Johnston, S., et al., *Charge disproportionation without charge transfer in the rare-earth-element nickelates as a possible mechanism for the metal-insulator transition.* Physical review letters, 2014. **112**(10): p. 106404.
42. Subedi, A., O.E. Peil, and A. Georges, *Low-energy description of the metal-insulator transition in the rare-earth nickelates.* Physical Review B, 2015. **91**(7): p. 075128.
43. Foyevtsova, K., et al., *LiNiO 2 as a high-entropy charge-and bond-disproportionated glass.* Physical Review B, 2019. **100**(16): p. 165104.
44. Etter, M., et al., *Charge disproportionation of mixed-valent Cr triggered by Bi lone-pair effect in the A-site-ordered perovskite BiC u 3 C r 4 O 12.* Physical Review B, 2018. **97**(19): p. 195111.
45. Weber, M.C., et al., *Raman spectroscopy of rare-earth orthoferrites R FeO 3 (R= La, Sm, Eu, Gd, Tb, Dy).* Physical Review B, 2016. **94**(21): p. 214103.
46. Wiglusz, R.J., et al., *A new approach in the synthesis of La 1− x Gd x FeO 3 perovskite nanoparticles–structural and magnetic characterization.* Dalton Transactions, 2015. **44**(46): p. 20067-20074.
47. Dąbrowa, J., et al., *An innovative approach to design SOFC air electrode materials: high entropy La 1− x Sr x (Co, Cr, Fe, Mn, Ni) O 3− δ (x= 0, 0.1, 0.2, 0.3) perovskites synthesized by the sol–gel method.* Journal of Materials Chemistry A, 2020. **8**(46): p. 24455-24468.
48. Radaelli, P., et al., *Charge, orbital, and magnetic ordering in La 0.5 Ca 0.5 MnO 3 s.* Physical Review B, 1997. **55**(5): p. 3015.
49. Alonso, J., et al., *Charge disproportionation in R NiO 3 perovskites: Simultaneous metal-insulator and structural transition in YNiO 3.* Physical Review Letters, 1999. **82**(19): p. 3871.
50. Medarde, M.L., *Structural, magnetic and electronic properties of perovskites (R= rare earth).* Journal of Physics: Condensed Matter, 1997. **9**(8): p. 1679.
51. Mazza, A.R., et al., *Variance induced decoupling of spin, lattice, and charge ordering in perovskite nickelates.* Physical Review Research, 2023. **5**(1): p. 013008.
52. Salamon, M.B. and M. Jaime, *The physics of manganites: Structure and transport.* Reviews of modern physics, 2001. **73**(3): p. 583.
53. Goodenough, J.B., *Metallic oxides.* Progress in solid state chemistry, 1971. **5**: p. 145-399.
54. Weber, W.J., C.W. Griffin, and J.L. Bates, *Effects of cation substitution on electrical and thermal transport properties of YCrO3 and LaCrO3.* Journal of the American Ceramic Society, 1987. **70**(4): p. 265-270.
55. Weber, W., C. Griffin, and J. Bates, *Electrical and thermal transport properties of the Y1− x Mx CrO3 system.* Journal of Materials Research, 1986. **1**(5): p. 675-684.
56. Mott, N., *Conduction in glasses containing transition metal ions.* Journal of Non-Crystalline Solids, 1968. **1**(1): p. 1-17.
57. Billinge, S., et al., *Direct observation of lattice polaron formation in the local structure of La 1− x Ca x MnO 3.* Physical Review Letters, 1996. **77**(4): p. 715.
58. Holstein, T., *Studies of polaron motion: Part II. The "small" polaron.* Annals of physics, 1959. **8**(3): p. 343-389.
59. Franchini, C., et al., *Polarons in materials.* Nature Reviews Materials, 2021. **6**(7): p. 560-586.

60. Shamblin, J., et al., *Experimental evidence for bipolaron condensation as a mechanism for the metal-insulator transition in rare-earth nickelates.* Nature communications, 2018. **9**(1): p. 86.
61. Serrano-Sánchez, F., et al., *On the lack of monoclinic distortion in the insulating regime of EuNiO 3 and GdNiO 3 perovskites by high-angular resolution synchrotron X-ray diffraction: a comparison with YNiO 3.* Dalton Transactions, 2021. **50**(20): p. 7085-7093.
62. Liu, Q., et al., *Magnetic properties of La doped SmFeO3.* Journal of Magnetism and Magnetic Materials, 2019. **469**: p. 76-80.
63. Blasse, G., *Energy transfer between inequivalent Eu2+ ions.* Journal of Solid State Chemistry, 1986. **62**(2): p. 207-211.
64. Jang, M.-K., Y.-S. Cho, and Y.-D. Huh, *Photoluminescence properties of Eu2+ activator ions in the SrS–Ga2S3 system.* Journal of Alloys and Compounds, 2020. **828**: p. 154424.
65. Yao, S.s., et al., *Luminescence studies on Ba2ZnSi2O7: Eu2+ phosphors crystals.* Luminescence, 2010. **25**(5): p. 399-402.
66. Binnemans, K., *Interpretation of europium (III) spectra.* Coordination Chemistry Reviews, 2015. **295**: p. 1-45.
67. Wi, S., et al., *Cation substitution induced structural phase transitions and luminescence properties of Eu3+-doped A2LaNbO6 (A= Ba, Sr, and Ca) double perovskite.* Journal of Alloys and Compounds, 2024. **976**: p. 173102.
68. Blasse, G., et al., *A general introduction to luminescent materials*. 1994: Springer.
69. Nikolić, M.G., D.J. Jovanović, and M.D. Dramićanin, *Temperature dependence of emission and lifetime<? A3B2 show [pmg: line-break justify=" yes"/]?> in Eu3+-and Dy3+-doped GdVO4.* Applied optics, 2013. **52**(8): p. 1716-1724.
70. Ćirić, A., S. Stojadinović, and M.D. Dramićanin, *Time-integrated luminescence thermometry of Eu3+ and Dy3+ doped YVO4.* Sensors and Actuators A: Physical, 2019. **295**: p. 450-455.
71. Schuurmans, M. and J. Van Dijk, *On radiative and non-radiative decay times in the weak coupling limit.* Physica B+ C, 1984. **123**(2): p. 131-155.
72. Musicó, B., et al., *Tunable magnetic ordering through cation selection in entropic spinel oxides.* Physical Review Materials, 2019. **3**(10): p. 104416.
73. Almishal, S.S., et al., *Untangling individual cation roles in rock salt high-entropy oxides.* Acta Materialia, 2024. **279**: p. 120289.
74. Gilleo, M. and S. Geller, *Magnetic and crystallographic properties of substituted yttrium-iron garnet, 3 Y 2 O 3· x M 2 O 3·(5− x) Fe 2 O 3.* Physical Review, 1958. **110**(1): p. 73.
75. Naik, S. and A. Salker, *Enhancement in the magnetic moment with Cr 3+ doping and its effect on the magneto-structural properties of Ce 0.1 Y 2.9 Fe 5 O 12.* Physical Chemistry Chemical Physics, 2012. **14**(28): p. 10032-10040.
76. Dong, B., et al., *The magnetic properties of BiY 2 Fe 5 O 12 nanoparticles doped with Cr ions.* Journal of materials science, 2007. **42**: p. 3167-3171.
77. Xu, H. and H. Yang, *Effect of Chromium on Magnetic Properties of Y2. 9Ce0. 1Fe5–x Cr x O12 Nanoparticles.* Materials and Manufacturing Processes, 2007. **23**(1): p. 10-13.
78. Chen, D., et al., *Structure and magnetism of novel high-entropy rare-earth iron garnet ceramics.* Ceramics International, 2023. **49**(6): p. 9862-9867.
79. Dąbrowa, J., et al., *Structure and transport properties of the novel (Dy, Er, Gd, Ho, Y) 3Fe5O12 and (Dy, Gd, Ho, Sm, Y) 3Fe5O12 high entropy garnets.* Journal of the European Ceramic Society, 2021. **41**(6): p. 3844-3849.

80. Zhang, S., et al., *Chemical stability and leaching mechanism of YIG and HEG at different pH conditions.* Journal of the American Ceramic Society, 2024. **107**(11): p. 7352-7363.
81. Golkari, M., H. Shokrollahi, and H. Yang, *The influence of Eu cations on improving the magnetic properties and promoting the Ce solubility in the Eu, Ce-substituted garnet synthesized by the solid state route.* Ceramics International, 2020. **46**(7): p. 8553-8560.
82. Peña-Garcia, R., et al., *The synthesis of single-phase yttrium iron garnet doped zinc and some structural and magnetic properties.* Materials Research Express, 2017. **4**(1): p. 016103.
83. Siebrand, W. and M.Z. Zgierski, *Franck–Condon effects in resonance Raman spectra and excitation profiles.* The Journal of Chemical Physics, 1979. **71**(9): p. 3561-3569.
84. Chen, Y., et al., *The influence of Fe concentration on Y3Al5− xFexO12 garnets.* Microelectronic engineering, 2005. **81**(2-4): p. 329-335.
85. Aakansha and S. Ravi, *Structural, magnetic and dielectric properties of Cr substituted yttrium iron garnets.* Journal of the American Ceramic Society, 2018. **101**(11): p. 5046-5060.
86. Aksenov, S.N., et al., *Phase transition in Y3Fe5O12 at high pressures observed by raman spectroscopy.* JETP Letters, 2021. **114**(12): p. 742-750.
87. Uyanga, E., et al., *Tailoring the properties of Y3AlxFe5-xO12 garnets through aluminum doping: A comprehensive study.* Materials Today Communications, 2025. **44**: p. 111996.
88. Yoshino, T., et al., *Room-temperature spin-glass behaviors and memory effects in Al-substituted Y3Fe5O12 epitaxial film grown by pulsed laser deposition.* AIP Advances, 2025. **15**(6).
89. Shannon, R.D., *Revised effective ionic radii and systematic studies of interatomic distances in halides and chalcogenides*. Acta crystallographica section A: crystal physics, diffraction, theoretical and general crystallography, 1976. **32**(5): p. 751-767.
90. Mydosh, J.A., *Spin glasses: an experimental introduction*. 1993: CRC press.
91. Edwards, S.F. and P.W. Anderson, *Theory of spin glasses.* Journal of Physics F: Metal Physics, 1975. **5**(5): p. 965.
92. Tholence, J. and R. Tournier, *Susceptibility and remanent magnetization of a spin glass.* Le Journal de Physique Colloques, 1974. **35**(C4): p. C4-229-C4-235.
93. Cardoso, C., et al., *Spin glass behavior in RuSr 2 Gd 1.5 Ce 0.5 Cu 2 O 10− δ.* Physical Review B, 2003. **67**(2): p. 020407.
94. Kniec, K., et al., *Intentional modification of the optical spectral response and relative sensitivity of luminescent thermometers based on Fe 3+, Cr 3+, Nd 3+ co-doped garnet nanocrystals by crystal field strength optimization.* Materials Chemistry Frontiers, 2020. **4**(6): p. 1697-1705.

Vita

Rubayet Tanveer was born and raised in Bangladesh. He earned his bachelor's degree in Electronics and Communication Engineering from the Institute of Science and Technology (IST), National University of Bangladesh, in 2014. He subsequently completed an M.Phil. in Physics with a concentration in Materials Science at the Military Institute of Science and Technology (MIST) in 2019, under the guidance of Dr. Brajalal Sinha and Dr. Mohammed Abdul Basith. Building upon this foundation, he pursued a master's degree in Nanoengineering at North Carolina A&T State University, where he conducted research under the mentorship of Dr. Shyam Aravamudhan. His growing interest in bulk structural and functional materials motivated him to undertake doctoral studies at the University of Tennessee, Knoxville, where he earned the Doctor of Philosophy degree in 2025. He gratefully acknowledges the guidance and inspiration of his teachers and mentors. He also acknowledges support from his mother for always keeping him on track with sticks, his father for never giving up on him and his wife for never complaining on his extra stays in the lab.